SEQUENCE DESIGN AND RECONSTRUCTION OPTIMIZATION FOR TRANSLATION OF MAGNETIC RESONANCE IMAGING

By

JAMES N. AHAD

Submitted in partial fulfillment of the requirements for the degree of

Doctor of Philosophy

Dissertation Adviser: Dr. Nicole Seiberlich

Department of Biomedical Engineering

CASE WESTERN RESERVE UNIVERSITY

May, 2023

CASE WESTERN RESERVE UNIVERSITY

SCHOOL OF GRADUATE STUDIES

We hereby approve of the dissertation of

James N. Ahad

Candidate to the degree of Doctor of Philosophy*

Research Advisor

Nicole Seiberlich

Committee Chair

Dominique Durand

Committee Members

Vikas Gulani

Mark Griswold

Xin Yu

Lee Ponsky

Date of Defense

January 18, 2023

*We also certify that written approval has been obtained for any proprietary material contained therein

In Memoriam

Gavin Hanson

1992 – 2018

For showing me the way forward

Table of Contents

List of Tables

List of Figures

Acknowledgements

The work presented in this thesis would not have been possible without the support of a great deal of family, friends, colleagues, and mentors. Completing my graduate studies has been a challenging experience that I have grown from and will one day look back fondly on (atleast this is what I have been told).

I firstly would like to thank my research advisor, Nicole Seiberlich. Her guidance and support have helped me develop as a scientist in ways that I would not have known coming into my PhD. Nicole helped create a welcoming, supportive lab with a group of amazing individuals that I have had the pleasure of working with these past years.

Secondly, I would like to thank Vikas Gulani, who has helped me think about the clinical side of scientific research, while reminding me to be clinically precise as a future physician. I am thankful for his scientific input and encouragement.

I would also like to thank my thesis committee members: Nicole Seiberlich, Vikas Gulani, Mark Griswold, Xin Yu, Lee Ponsky, and Dominique Durand. Thank you for your helpful insights during committee meetings and your time and support during my tenure in Cleveland and Ann Arbor.

I would also like to thank my colleagues and the staff at both the Case Center for Imaging Research and the Michigan Institution of Imaging Technology and Translation for helping support me on my journey, with a special thanks to Katie Wright, Yun Jiang, and Alex Fyrdahl for being supportive in many aspects of my life during my PhD.

My graduate studies would have been impossible without my friends. I am lucky to have too many friends to list in entirety but I will list a few special friends who have been close and dear to my during time. Thank you to Michael Sun, Sherry Huang, Norman Luc, Aaron Talsma, Alicia Vagnozzi, Sarah Venus, and Peter Wang. A special thanks to Gavin Hanson, who got me into this mess and is dearly missed.

Finally I would like to thank my family. Thank you to my parents, Sonny and Ellen Ahad, for their support and unwanted, frustrating encouragement. Especially my mother, on her ceaseless questions on the status of my thesis. Thank you to my grandparents, Kyaw Aun and Tin Tin, for being the greatest grandparents someone could ask for. Thank you to Caesar Ahad for your wonderful banter and encouragement. And thank you to my sister, Bridget Ahad, for being pretty great.

Sequence Design and Reconstruction Optimization for Translation of Magnetic Resonance Imaging

James N. Ahad

Abstract

Magnetic Resonance Imaging is a clinical imaging modality that has excellent soft tissue contrast, enabling it to answer clinical questions on a range of pathologies that other imaging methods cannot. However, conventional MR techniques typically have slow acquisitions that prevent applications in imaging physiological motion. In addition, other imaging modalities such as CT produce quantitative, reproducible pixel values, whereas MRI generally produces qualitative images. To address these issues, many new MR techniques have been developed but require additional optimization or development to be adopted clinically.

Three main projects involving the translation of emerging techniques in MR to clinical application will be described in this thesis. In the first project, a fast imaging technique known as through-time radial GRAPPA is optimized to reduce total acquisition time and reconstruction overhead to enable free-breathing un-gated cardiac CINE. The second project discusses a new quantitative imaging technique in the heart, known as Cardiac Magnetic Resonance Fingerprinting (cMRF), which requires a lengthy dictionary simulation step to be performed with each reconstruction. cMRF dictionary simulation is implemented and optimized on a reconstruction platform known as Gadgetron to enable clinically integration of cMRF. In the final project, in-bore MR-guided prostate biopsy is an interventional technique that requires long T_2-weighted imaging. A simulation

approach taken to find a faster T_2-weighted imaging sequence among Cartesian and spiral TSE sequence variants.

Chapter 1 Introduction

Magnetic Resonance Imaging (MRI), nearly 50 years after Paul Lauterbur's seminal paper on the subject, has become an integral component of the modern health care system. MRI is a powerful imaging modality that provides excellent soft tissue contrast without the use of ionizing radiation. In addition, image contrast can be made sensitive to a myriad of tissue properties, including magnetic tissue properties such as T_1 and T_2[1], dynamic properties such as flow[2], structural properties such as diffusion[3,4], and even biochemical properties such as proton chemical exchange[5]. The versatility of MRI has driven the development of a multitude of applications beyond just anatomical imaging, including but not limited to functional imaging of the brain[6,7], quantification of fat in the liver[8] and muscle[9], and real-time dynamic imaging of speech[10] and the heart[11]. The advantages afforded by MRI make it an invaluable tool for answering clinical questions concerning a wide range of pathologies, making this technique vital to the modern practice of medicine.

However, as compared to other imaging techniques such as computed tomography (CT) and ultrasound, MRI has a lengthy acquisition time. Firstly, the different contrasts in MRI are generated by the dynamics of nuclear spins within a tissue, which require time to evolve and differentiate themselves from other tissues. In addition, signal produced by the evolving spin dynamics within a tissue must be localized to form an image, which requires spatially encoding the NMR signal of an imaging object, a process that requires repeated measurements of the MR signal. In concert, these two factors result in MR

images being collected on the order of minutes in modern clinical imaging, in comparison to other imaging techniques that are collected on the order of seconds. **Chapter 2 will provide a brief introduction to the fundamentals of MRI, and will cover the source of the NMR signal, basic pulse sequences for generating MR contrast such as spin echo and gradient echo imaging, spatial encoding of MR images, non-Cartesian sampling, and parallel imaging.**

The lengthy acquisition time of MRI presents challenges for imaging in the presence of motion. While external controls such as clinical instructions and breath-hold scans can mitigate artifacts due to breathing and physical motion during an MRI exam, these still do not mitigate physiological motion such as the beating of the heart, peristalsis of the bowel, or the flow of blood. While special acquisition techniques utilizing navigators[12], gating[13,14], or rapid imaging methods such as parallel imaging[15,16] or non-Cartesian sampling[17,18] can be used to overcome some of these difficulties, such techniques can be accompanied by lengthy image reconstructions, are prone to other non-motion related artifacts such as aliasing or are limited in resolution. **In chapter 3, cardiac MRI using non-Cartesian Radial GRAPPA is optimized to enable real-time imaging of cardiac motion while reducing scanning and reconstruction time**. In that chapter, we demonstrate how compression of the acquired signal reduces both the need for additional calibration scans and reconstruction complexity.

Another disadvantage of MRI is the qualitative nature of MR images. Pixels in an MR image have magnitudes that vary between MR scanners, individuals, and

environments. In contrast, pixels in CT, PET or SPECT all correspond to distinct measurements of photon counts that are consistent and repeatable across a range of conditions and imaging subjects. However, MR mapping techniques can acquire quantitative maps of various MR properties such as T_1 and T_2 relaxation times. Most of these T_1 and T_2 mapping techniques rely on acquiring multiple images and fitting the pixel-wise signal evolution to an exponential decay curve. Not only is the acquisition of multiple images time-consuming, but these techniques also map only a single tissue property at a time. Magnetic Resonance Fingerprinting[19] (MRF) is a newer technique that can acquire quantitative measurements of multiple tissue properties simultaneously, by using a designed pulse train to cause the dynamics of nuclear spins to evolve in a complex manner. The resulting signal evolutions from a variety of different tissue property permutations can be modeled using simulations, forming a dictionary of signal fingerprints for each potential combination of tissue properties. The signal evolutions of pixels in a highly undersampled image can be pattern matched to the dictionary, simultaneously producing maps of various tissue properties. MRF uses a predetermined excitation pattern, which then requires the fingerprint dictionary to be computed only once. However, cardiac MRF uses sequence timings that rely on variable ECG signal, necessitating the computationally complex generation of a new dictionary with each scan. **In Chapter 4, cardiac MRF dictionary generation is optimized to enable online implementation of image reconstruction in a clinically feasible timeframe.** Measurements of tissue properties between the optimized online implementation and previously

published technique are compared and show good agreement despite significant reductions in computation time.

While MRI can be used to acquire images with an array of different tissue contrasts, acquiring some types of contrast can be time-consuming. A typical MR examination protocol can accommodate longer image acquisitions with good planning; however, interventional clinical applications are performed more efficiently and safely with shorter procedures which require shorter acquisition times. Prostate biopsies are routine procedures that are vital for the diagnosis and clinical management of prostate cancer patients. Of these prostate biopsy techniques in-gantry MR-guided prostate biopsy is the most sensitive and specific but requires lengthy T_2-weighted images with high resolution and field-of-view requirements for interventional guidance. While faster interventional imaging techniques may not have the same image quality as current imaging, a faster technique with sufficient contrast and resolution to perform the procedure with safety and confidence would greatly improve the efficiency of in-gantry MR-guided prostate biopsy. **In chapter 5, the sequence design space for fast T_2-weighted imaging is explored via simulations using phantoms designed to mimic in-gantry prostate biopsy imaging.** Simulations enable sampling a large part of the design space, and enabled comparisons between multiple sequence parameters including echo train length, echo spacing, acceleration factor, partial Fourier acquisition, and Cartesian and non-Cartesian sampling. Based on measured image quality metrics, comparisons are made between different fast imaging sequences for MR-guided prostate biopsy.

Chapter 2 MRI Fundamentals

The goal of this chapter is the present the MRI concepts that form the foundation of the work presented in this thesis. To begin, an overview of the generation of the MR signal and signal differences due to relaxation is covered. Following that, spatial encoding is discussed to describe the localization of MR signal in space which is necessary for imaging. Then some basic imaging sequences used in this thesis are introduced along with common sources of imaging artifacts that accompany MR imaging in different body regions. Finally, parallel imaging and model-based reconstruction are discussed as methods to accelerate MR imaging.

2.1: The Source of Signal in MRI

The MR signal, in typical medical imaging, is derived from the NMR physics of atomic nuclei with non-zero quantum spin. There exist multiple candidate nuclei with non-zero spin that can be imaged, but due to the abundance of hydrogen in organic matter, hydrogen nuclei are the most common source of signal in medical MR imaging. The quantum mechanical property of spin results in a spin angular momentum. The spin angular momentum S of any nuclei can be described as:

$$S^2 = \hbar^2 s(s+1) \tag{2-1}$$

Where $\hbar$ is Planck's constant and s is the spin quantum number of the nucleus. When measured along the z-axis, the spin angular momentum S_z is:

$$S_z = \hbar m_s \tag{2-2}$$

Where m_s can assume the values:

$$m_s = s, s-1, s-2, \ldots, -s \tag{2-3}$$

The magnetic moment μ of the nucleus is related to the spin angular momentum:

$$\mu = \gamma S \tag{2-4}$$

Where γ is the gyromagnetic ratio of the nucleus. For the proton or hydrogen nuclei, the gyromagnetic ratio is equal to 42.58 MHz/T. When placing a magnetic moment in an external magnetic field B, the energy of the nucleus is:

$$E = -\mu \cdot B \tag{2-5}$$

From this, the Hamiltonian can be defined as:

$$H = -\hbar\gamma S \cdot B \tag{2-6}$$

If the external magnetic field is aligned with the z-axis, this equation simplifies to:

$$H = -\hbar\gamma S_z B_z \tag{2-7}$$

For the proton which has a spin quantum number of ½, two energy states can be assumed:

$$\begin{aligned} E\left(m_s = +\frac{1}{2}\right) &= \frac{\hbar\gamma B_z}{2} \\ E\left(m_s = -\frac{1}{2}\right) &= -\frac{\hbar\gamma B_z}{2} \end{aligned} \tag{2-8}$$

This energy separation of an otherwise degenerate energy level in the presence of an external magnetic field is known as Zeeman splitting.

Absorption or emission of a photon with frequency ω can result in a proton transitioning between the two states:

$$\Delta E = \hbar\gamma B_z = \hbar\omega \tag{2-9}$$

Which simplifies to the Larmor equation

$$\omega_0 = \gamma B_0 \tag{2-10}$$

Where ω_0 is the Larmor frequency for a nucleus placed in external magnetic field B_0.

In reality, protons do not exist in isolation so in an ensemble of nuclei (or spins), known as a spin isochromat manifests quantum properties as macroscopic properties that can be modeled classically. Due to Zeeman splitting, the small energy differential between the parallel and antiparallel states caused by an external magnetic field, the spin populations in a spin isochromat reach a Boltzmann equilibrium between the two states, with a small excess of spins aligned parallel to external field. This results in a macroscopic net magnetization aligned parallel with the field typically referred to as M_0. M_0 is directly related to the SNR in an NMR experiment and is derived by multiplying the magnetic moment μ by the relative excess of parallel spins. This yields the following relationship:

$$M_0 = \frac{\rho \gamma^2 \hbar^2 B_0}{4 k_B T} \tag{2-11}$$

Where ρ is the spin density, k_B is the Boltzmann constant, and T is the temperature.

When placed in an external magnetic field, individual nuclear spins within the ensemble will precess about the axis of the external field at their Larmor frequency $\omega_0$20–22 shown in equation 2-10. However, it should be noted that the net magnetization M_0 is stationary and aligned with the z-axis, and thus does not precess. In this state, the net magnetization is not detectable and requires excitation by a separate external magnetic field B_1. Under the influence of a

polarized B_1 field rotating in resonance with the Larmor frequency of our isochromat, the net magnetization M_0 experiences a torque that rotates it towards the transverse plane. This polarized B_1 field is referred to as a radiofrequency (RF) pulse, and the angle that the net magnetization is tipped is known as the flip angle Φ. The process of excitation is shown in Figure 2-1. The flip angle Φ is related to the B_1 as follows:

$$\Phi(t) = \gamma \int_0^t B_1(\tau) d\tau \tag{2-12}$$

where γ is the gyromagnetic ratio.

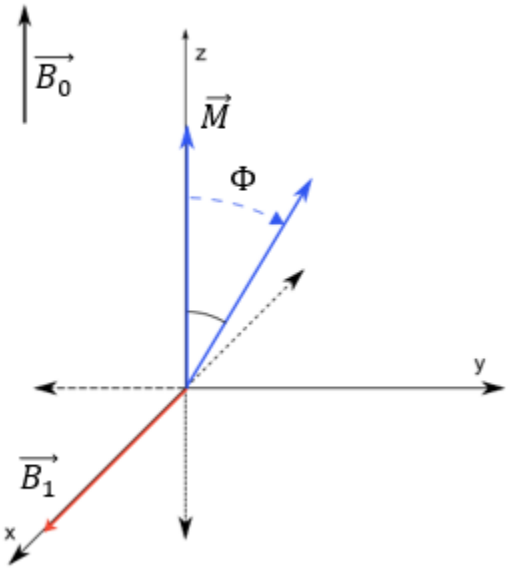

Figure 2-1: Depiction of excitation of magnetization vector $\vec{M}$ due to the action of the $\vec{B_1}$ field. The flip angle Φ is related to the magnitude of the RF pulse with the relationship shown in equation 2-2.

Given $\Phi = 90^0$, the magnetization of our isochromat now exists entirely within the transverse plane with no longitudinal magnetization. This magnetization will now experience another torque caused by the main magnetic field B_0 resulting in a precession of the magnetization about the longitudinal axis at the Larmor

frequency. The precessing magnetization produces a magnetic flux that can be detected using a loop of wire, or coil, through Faraday's law, generating the NMR signal.

Following excitation of the longitudinal magnetization by an arbitrary flip angle Φ, the net magnetization will then begin to relax away from the transverse plane back to the longitudinal axis, taking the form:

$$M_z(t) = M_z(0)\, e^{-t/T_1} + M_0\left(1 - e^{-t/T_1}\right)$$
$$M_\perp(t) = M_\perp(0)\, e^{-t/T_2} \tag{2-13}$$

where:

$$M_z(0) = \mathrm{M}_0 cos(\Phi)$$
$$M_\perp(0) = \mathrm{M}_0 sin(\Phi) \tag{2-14}$$

and where T_1 and T_2 are time constants characterizing recovery of longitudinal magnetization M_z and decay of transverse magnetization $M_\perp$, respectively. T_1 and T_2 relaxation are phenomena typically characterized by different processes, but it should be noted that they are not fully independent, as mechanisms causing T_1 relaxation also cause T_2 relaxation. As indicated in equation 2-13, T_1 relaxation describes the regeneration of longitudinal relaxation and is often called spin-lattice relaxation. During this process, spins exchange energy with their environment to return to a Boltzmann equilibrium between the parallel and antiparallel spin states. However, due to the small energy differential between the two states, spontaneous emission of a photon to transition states is rare. Instead, a local oscillating magnetic field is required to effectively behave as an RF pulse, exchanging energy between the spin and environment, to allow the state transition to happen. Such local fields can arise due to molecular motion

and optimally allow energy transfer when they oscillate at the Larmor frequency. Thus, T_1 tends to be long in both highly mobile and immobile environments, where the frequency of molecular tumbling is at a mismatch with the Larmor frequency. Most tissues containing protein and fat have molecular tumbling rates that favorably oscillate near the Larmor frequency and have relatively shorter T_1. Interestingly, increasing the strength of the main external magnetic field B_0 results in an increase in Larmor frequency and increase the mismatch between tumbling frequency and the Larmor frequency, thus prolonging the T_1 time.

In contrast, T_2 relaxation is due to a loss of phase coherence of excited spins within a spin ensemble. The resulting effect, described in equation 2-13, is a loss of net transverse magnetization. It should be noted, the same mechanism that results in T_1 relaxation also adds random phase, and thus also causing decoherence and contributing to T_2 effects. In addition to spin-lattice relaxation, loss of phase coherence can also be due to spin-spin interactions as well as microscopic field inhomogeneities. Spin-spin interactions are a type of dipolar interaction, where two local spins simultaneously exchange their longitudinal spin state, switching from parallel to anti-parallel and vice versa. The resulting interaction does not cause T_1 relaxation, but the exchange of energy still results in quantum decoherence and T_2 relaxation. In addition, microscopic field inhomogeneities due to additive contributions from local nuclei can cause dephasing by slightly changing the precession frequencies of local spins. These field inhomogeneities require low molecular motion to persist, and thus T_2 is directly proportional to the molecular tumbling rate.

In addition to T_2 relaxation, another phenomenon known as T_2* relaxation can also cause loss of phase coherence. T_2* relaxation is often due to macroscopic inhomogeneities of the main external magnetic field B_0, and classically causes loss of phase coherence at a much faster rate than T_2 mechanisms. However, due to the static nature of external field inhomogeneities, methods of recovering lost magnetization due to T_2* relaxation do exist and are visited later in this chapter. However, the remainder of this discussion will assume negligible T_2* effects.

While the magnetization dynamics in MR are complex, they can be succinctly described by the Bloch equations which can be considered the equations of motion for NMR applications. The Bloch equations as presented in block-matrix form are:

$$\frac{d}{dt}\begin{pmatrix} M_x \\ M_y \\ M_z \end{pmatrix} = \begin{pmatrix} -\frac{1}{T_2} & \gamma B_z & -\gamma B_y \\ -\gamma B_z & -\frac{1}{T_2} & \gamma B_x \\ \gamma B_y & -\gamma B_x & -\frac{1}{T_1} \end{pmatrix}\begin{pmatrix} M_x \\ M_y \\ M_z \end{pmatrix} + \begin{pmatrix} 0 \\ 0 \\ \frac{M_0}{T_1} \end{pmatrix} \qquad (2\text{-}15)$$

The relaxation effects of T_1 and T_2 form much of the contrast between tissues seen in MR, but there exist other effects such as diffusion or flow that can be modeled using the Bloch equations. Chapter 5 will discuss using Bloch equations to simulation the effects of MR acquisitions and artifacts and will go into Bloch equation simulations in further detail.

2.2: MR Imaging by Spatially Encoding the NMR signal

In an MR imaging experiment, the object to be imaged is composed of many populations of spins with different relaxation properties distributed in space.

Thus, to distinguish spin isochromats in different spatial locations, magnetic field gradients are utilized to spatially encode the NMR signal. Recall from equation 2-10, that the Larmor frequency of a spin is directly proportional to the external magnetic field that it experiences. For a set of spins distributed along the x-axis, the application of a magnetic field gradient G_x would cause the following distribution of Larmor frequencies:

$$\omega_0(x) = \gamma(B_0 + x \cdot G_x) \tag{2-16}$$

Thus, the signal detected from a coil near an object experiencing an x-axis magnetic field gradient would be the superposition of sinusoids, with each frequency corresponding to a location in space. Assuming no relaxation occurs, the resulting signal contribution from one infinitesimal block along the x-axis is:

$$dS(x,t) = \rho(x) \cdot e^{i2\pi\varphi(t)}dx \tag{2-17}$$

Where $\rho(x)$ is a detectable spin density that is proportional to the transverse magnetization and $\varphi(t)$ is a time-varying phase term due to the spatial encoding gradient. This term has the form:

$$\varphi(t) = \frac{\gamma}{2\pi}\int_0^t x \cdot G_x(\tau)d\tau \tag{2-18}$$

If we define a parameter k:

$$k(t) = \frac{\gamma}{2\pi}\int_0^t G_x(\tau)d\tau \tag{2-19}$$

And integrate the signal over the x-domain, the total signal S is:

$$S(t) = \int \rho(x) \cdot e^{i2\pi xk}dx \tag{2-20}$$

Note that this signal is the Fourier transform of the spin density distribution in space, and that the time-dependence of the signal is implicitly encoded in spatial frequency k. Thus the relationship between the spatially encoded time-domain signal and the physical spin density is:

$$S(t) \overset{\mathcal{F}}{\Leftrightarrow} \rho(x) \tag{2-21}$$

Where $\mathcal{F}$ is an operator representing the continuous Fourier transform. In practice, data cannot be acquired continuously over infinite time, and thus the finite sampled signal s(t) is said to collected in k-space and related to the reconstructed spin density $\hat{\rho}(x)$ via the discrete Fourier transform.

The spatial encoding process using gradients can be extended to two and three dimensions by using additional gradients along the y and z axes. The sampling in k-space due to these additional equations is an extension of equation 2-19, with additional equations describing the sampling trajectory through k_y and k_z:

$$\begin{aligned} k_x(t) &= \frac{\gamma}{2\pi}\int_0^t G_x(\tau)\, d\tau \\ k_y(t) &= \frac{\gamma}{2\pi}\int_0^t G_y(\tau)\, d\tau \\ k_z(t) &= \frac{\gamma}{2\pi}\int_0^t G_z(\tau)\, d\tau \end{aligned} \tag{2-22}$$

Any combination of gradient waveforms can be used to sample k-space, however, a Cartesian sampling scheme with equidistant samples is often used to enable compatibility with the Fast Fourier Transform (FFT). In the Cartesian sampling scheme, an axis is selected as the so-called frequency encoding direction, and the other axes become so-called phase encoding directions. The

frequency encoding gradient is turned on simultaneously with the ADC for signal acquisition and thus are also called the readout gradients. During the signal acquisition process, due to the frequency encoding gradient, spins along the frequency encoding direction precess at different frequencies, resulting in a signal that is a superposition of all contributing frequencies as described in equation 2-20. Phase encoding gradients are not used during signal acquisition, but rather prior to the readout gradient where they add a linear phase shift over the direction along which they are applied, which is encoded in the acquired time-domain signal. Thus the signal is acquired in a rasterized fashion, repeatedly acquiring a line of frequency encoded data for all the phase encoding steps.

The model for discrete sampling is to multiply the continuous signal by a Dirac comb, otherwise known as an impulse train of Dirac delta functions separated by some sampling time period T_s. The sampled function s is then related to the continuous signal as:

$$s(t) = S(t) \cdot \text{Ш}_{T_s}(t) \tag{2-23}$$

Where

$$\text{Ш}_{T_s}(t) = \sum_{\ell = -\infty}^{\infty} \delta(t - \ell T_s) \tag{2-24}$$

The resulting Fourier representation of the discrete signal is:

$$\mathcal{F}\{s(t)\} = \rho(x) \cdot \text{Ш}_{1/T_s}(x) \tag{2-25}$$

The resulting reconstructed image is therefore composed of periodic representations of the image every $1/T_s$ intervals. Recall from equation 2-19, the

spatial frequency k is inherently time dependent, so for a constant strength readout gradient with magnitude G_{RO}, each sample is spaced Δk apart:

$$\Delta k_{\mathrm{RO}} = \frac{\gamma}{2\pi} G_{\mathrm{RO}} \cdot T_s \tag{2-26}$$

The phase encoding gradients also traverse k-space, doing so by linearly stepping the magnitude of the gradient:

$$\Delta k_{\mathrm{PE}} = \frac{\gamma}{2\pi} \Delta G_{\mathrm{PE}} \cdot T_{PE} \tag{2-27}$$

Where ΔG_{PE} is the linear step in gradient magnitude on the phase encoding axis, and T_{PE} is the duration the gradient is turned on. Thus from equations 2-26 and 2-27, the resulting sampled data falls on a regular Cartesian grid in k-space, such that the acquired data can be directly transformed to the image domain via the Fast Fourier Transform (FFT). The simplicity of this image reconstruction is part of the reason that Cartesian sampling schemes form the backbone of modern clinical MR imaging.

The Fourier relationship between the time-domain signal and the object does enforce constraints in real-world imaging applications for which sampling occurs for a finite period and at discrete sampling intervals. The k-space spacing Δk defines the locations of aliases of our imaging object, which then occur every $\frac{1}{\Delta k}$ mm. This quantity is referred to as the field-of-view (FOV) and is related to the selected acquisition parameters in both the readout and phase encoding axes:

$$FOV = \frac{1}{\Delta k} = \frac{2\pi}{\gamma G_{\mathrm{RO}} \mathrm{T_s}} = \frac{2\pi}{\gamma \Delta G_{\mathrm{PE}} T_{PE}} \tag{2-28}$$

To satisfy the Nyquist criterion, the FOV must be set sufficiently large to prevent aliasing in the MR image.

In addition to sampling frequency, real-world imaging experiments also sample for finite duration which also has consequences for the resulting MR imaging due to Fourier properties. From the Nyquist criterion, the spatial frequency bandwidth limits the spatial resolution Δw. Typically the boundaries of k-space are defined as $-k_{max}$ to $+k_{max}$, so the resolution is related to the maximum sampled spatial frequency as:

$$\Delta w = \frac{1}{2k_{max}} = \frac{2\pi}{\gamma G_{\mathrm{RO}} \mathrm{T}_{\mathrm{ADC}}} = \frac{\pi}{\gamma G_{\mathrm{PE,Max}} T_{PE}} \tag{2-29}$$

In summary, the Fourier relationship between the MR signal and the object designates the requirements for imaging large objects requiring large field-of-views and for imaging at high resolution to resolve small anatomical features. These requirements can be met by setting six degrees of freedom from which the FOV and resolution can be designed: G_{RO}, $\mathrm{T_s}$, $\mathrm{T_{ADC}}$, G_{PE}, $G_{\mathrm{PE,Max}}$, and T_{PE}. There are many considerations for choosing specific values for these parameters, such as reducing artifacts, improving SNR, or improving acquisition speed. The relationships between FOV, resolution, and k-space are shown in Figure 2-2. Due to the rasterized acquisition method of Cartesian MRI, the total acquisition time is typically bound by the number of phase encoding steps:

$$T_{acq} = T_R \cdot N_{PE1} \cdot N_{PE2} \tag{2-30}$$

Where T_R is the repetition time between phase encoding steps. Methods do exist to reconstruct undersampled images, which will be discussed later in this chapter.

From this discussion, it can be observed that spatial encoding of the object relies on spins to be stationary. Spins in motion would not experience a constant

field strength due to the frequency encoding gradient and would accumulate phase that would prevent the correct spatial localization of said spin and cause image “ghost” artifacts. In fact, any process that causes unintended accumulations of phase can cause such imaging artifacts to appear during reconstruction. For many of these processes, there are imaging techniques to either mitigate or leverage their effects utilizing gradients or other MR sequence elements for the purposes of altering image contrast. Such imaging techniques are not the topic of this thesis, but it should be noted that these techniques, such as diffusion-weighted imaging, MR elastography, and others, also provide significant value to modern clinical practice.

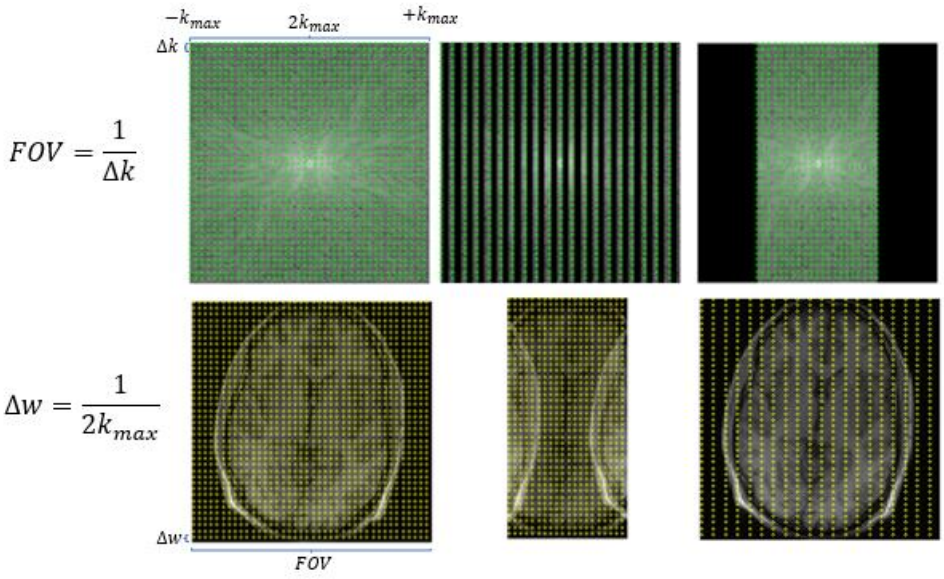

Figure 2-2: (Left) Relationship between resolution (Δw), FOV, Δk and k_{max} are shown for fully sampled k-space. Sampled k-space points are shown in green. Pixels in image space are shown in yellow. Cartesian k-space and the image domain are related via the Fast Fourier Transform. (Center) Uniform undersampling in a single direction leads to aliasing of the image along the x-axis. (Right)Acquiring a reduced k-space while retaining k-space spacing also reduces the number of collected lines, but results in loss of resolution instead. Blurring can be seen in the image domain along the x-axis.

2.3: Basic MR Sequences

The previous section on spatial encoding neither accounted for spin relaxation nor considered how sampling is repeated over several phase encoding steps to acquire sufficient k-space data to reconstruct an image. A MRI pulse sequence is a set of timings for various elements, such as gradients, RF pulses, and ADC sampling periods, that are played out and repeated to acquire k-space data. From equation 2-11 and 2-13, tissues can be distinguished by a vast array of different properties including relaxation parameters such as T_1, T_2, and T_2*, spin density, and temperature among other things. By controlling the timing intervals between sequence events, a pulse sequence can generate contrast between spins with different properties. This section will cover two basic pulse sequences: spin echo (SE) and gradient echo (GRE) imaging, but it should be noted that a myriad of pulse sequences exist to generate tissue contrast in different ways that may dependent on a variety of tissue properties besides T_1 and T_2 relaxation. In addition to these basic pulse sequences, a brief overview of multi-echo sequence is also included, due to their importance in fast spin echo sequences and steady state sequences which are utilized in this work.

As described earlier, isochromats excited by a RF pulse typically undergo T_1 and T_2 relaxation. Measurement of the signal directly after RF excitation, also known as the free-induction decay (FID) signal[23], could theoretically provide sufficient contrast information to distinguish different isochromats. However, T_2* relaxation often causes rapid loss of signal, causing low SNR and poor image quality. The prototypical MR sequence, the spin-echo sequence[24], is designed to recover magnetization lost due to T_2* relaxation and acquire signal during the

"spin-echo" where signal is maximally recovered. The spin-echo pulse sequence is shown schematically in Figure 2-3.

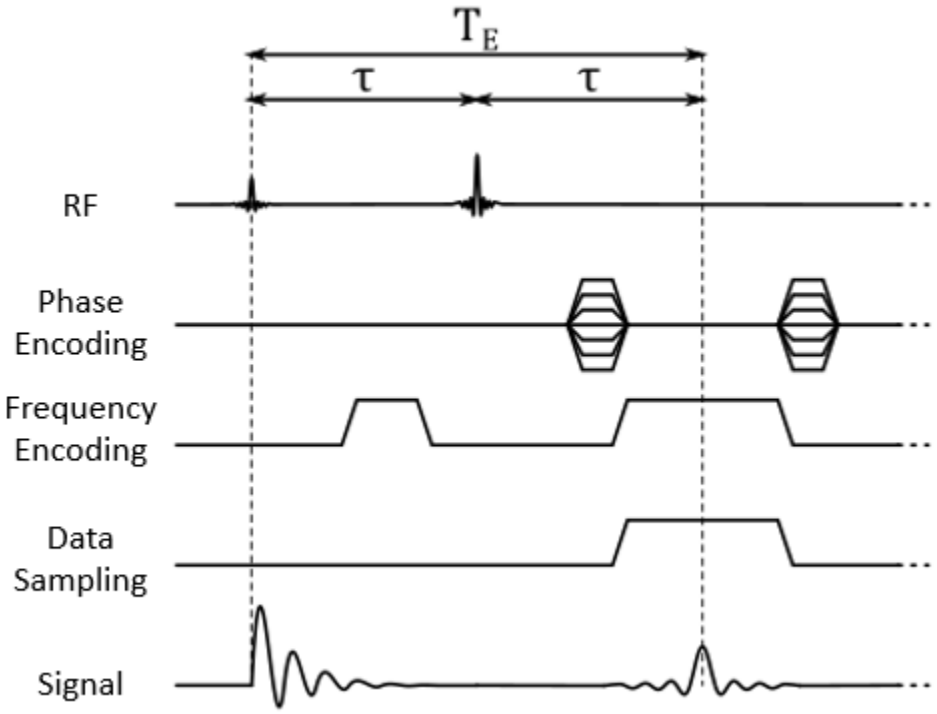

Figure 2-3: The spin-echo pulse sequence utilizes two RF pulses, an excitation pulse at $t = 0$ and a refocusing pulse at $t = \tau$. The excitation pulse produces an FID signal that decays due to T_2 relaxation. The refocusing pulse inverts the phase of the magnetization resulting in refocusing at the echo time $t = 2\tau$, at which time the echo forms. Spatial encoding and data acquisition occur during the spin echo to maximize signal. A prephaser is played on the frequency encode axis prior to the refocusing pulse to minimize time spent on dephasing gradients during acquisition. Note that the spin echo has lower peak signal compared to the FID which is due to T_2 decay.*

Following an excitation pulse, spins in an inhomogeneous field experience a Larmor frequency shift:

$$\omega = \gamma(B_0 + \Delta B_0) = \omega_0 + \Delta\omega \tag{2-31}$$

Where ΔB_0 is the magnitude of the field inhomogeneity in the spin's local environment and $\Delta\omega$ is the relative change in the Larmor frequency. Thus, over time the phase accumulation of this spin following excitation relative to the reference frame rotating at $\Delta\omega$ is:

$$\varphi(t) = \Delta\omega \cdot t \tag{2-32}$$

Resulting in loss of phase coherence, reduction in the net magnetization, and loss of signal. To recover phase coherence, the spin echo pulse sequence plays out a 180° refocusing pulse at some time τ following the excitation pulse. The RF phase of the refocusing pulse is shifted 90° from the excitation pulse, thus if the excitation pulse tips the magnetization onto the x-axis, the refocusing pulse rotates the magnetization about the x-axis. Spins that have maintained phase coherence are unaffected by the refocusing pulse, but spins that have dephased have their phase inverted. Thus the phase behavior of spins around the refocusing pulse, played at time τ is:

$$\varphi(t) = \begin{cases} \Delta\omega \cdot t & t < \tau \\ \Delta\omega(t-\tau) - \Delta\omega \cdot \tau & t > \tau \end{cases} \quad (2\text{-}33)$$

At time 2τ, also known as the echo time or T_E, all spins regardless of their local magnetic field environment are in phase coherence. This phenomenon is known as a spin echo and results in recovery of signal lost due to T_2* relaxation but not due to T_2 relaxation which is unrecoverable. The magnetization of isochromats at different precession frequencies during a spin echo sequence is shown in Figure 2-4.

Following data acquisition around the spin echo, the pulse sequence has a waiting period up until some time T_R known as the repetition time. This waiting period allows the longitudinal magnetization to recover due to T_1 relaxation. At the repetition time, the pulse sequence is repeated for a new phase encoding step. The overall signal for a spin echo sequence, due to refocusing at the spin echo, is then dominated by T_1 and T_2 effects and can be described by the following signal equation:

$$S \sim \rho \cdot exp\left(-\frac{T_E}{T_2}\right)\left[1 - exp\left(\frac{T_R}{T_1}\right)\right] \quad (2\text{-}34)$$

Where ρ is the proton spin density. Based on this signal equation, the spin echo sequence can be performed with different timing choices for T_E and T_R to yield T_1-weighted, T_2-weighted, and proton density weighted images, where weighting refers to the predominant source of contrast in the image. Typically T_1-weighted images have short T_E and short T_R, T_2-weighted images have long T_E and long T_R, and proton density-weighted images have short T_E and long T_R.

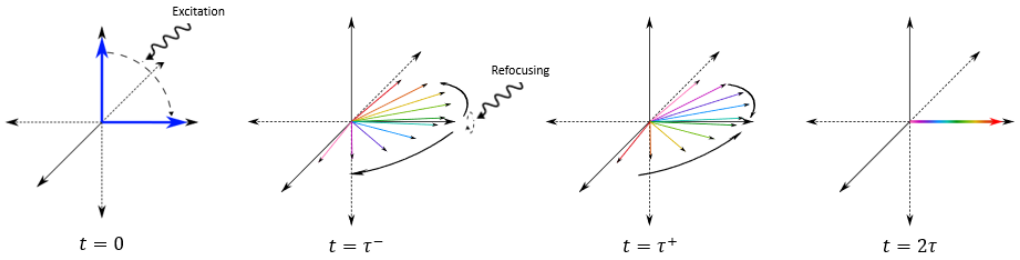

Figure 2-4: Illustration depicting the evolution of the magnetizations of various off-resonant isochromats during a spin-echo sequence. At $t = 0$, an excitation pulse tips the magnetization into the transverse plane. After some time τ, isochromats at different precession frequencies have dephased resulting in loss of transverse signal. A 180° refocusing pulse rotates the magnetizations of off-resonant isochromats, inverting their phase. Following the refocusing pulse, the magnetization begins to rephase culminating in a coherent transverse magnetization at $t = 2\tau$.

In contrast to the spin echo pulse sequence, the gradient echo pulse[25–27] sequences do not use a refocusing pulse to restore phase coherence. Thus all flavors of GRE are in part affected by T_2* relaxation. Fundamentally, GRE uses imaging gradients to produce a so-called gradient echo shown in Figure 2-5. A gradient echo is formed with the application of two gradients. First a dephasing gradient is used to disperse the FID signal. Because this dephasing process is done with a gradient, it disperses the signal in a predictable fashion described by equation 2-18. Then, at any point in time later in the sequence, a rephasing gradient is used to refocus the phase dispersion caused by the dephasing

gradient producing a gradient echo. Typically, the readout gradient also serves as the refocusing gradient and the dephasing gradient has half the area of the readout so that the gradient echo and maximum signal is collected at the center of k-space. Because GRE sequences do not play out a refocusing pulse, data can be collected with much shorter T_E limited only by maximum gradient strength. In addition, excitation flip angles for GRE sequences are typically less than 90° which reduces the need for longer T_R to recover longitudinal magnetization. Thus, GRE sequences often have faster acquisition times compared to spin echo sequences. However, because GRE sequences do not refocus phase dispersing effects other than the frequency encoding gradient, they are particularly prone to imaging artifacts caused by off-resonance, B_0 field inhomogeneity, and motion. There exist many ways of compensating for these effects in reconstruction, but the overall performance of GRE at mitigating these effects is much less than spin echo.

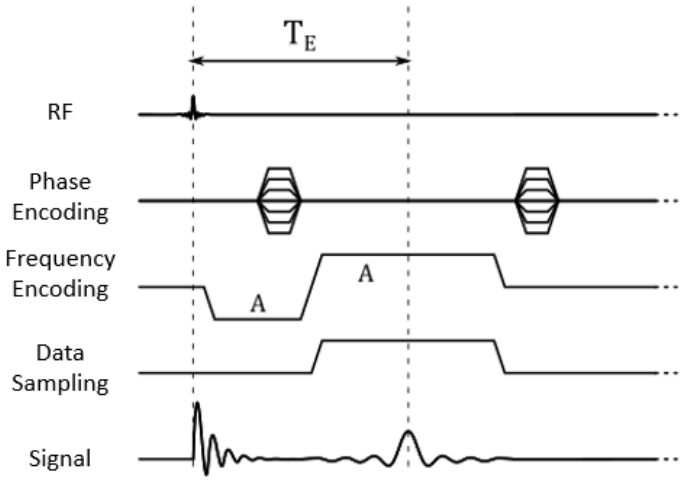

Figure 2-5: A gradient echo pulse sequence is shown here. Following an RF excitation pulse, the signal is dephased due to the action of the dephasing gradient with reverse polarity to the frequency encoding gradient. The action of the dephasing gradient is reversed due to the frequency encoding gradient resulting an echo at the echo time and maximum signal during the acquisition of the center of k-space. Note that the area of the dephasing gradient (A)

matches the area of the first half of the frequency encoding gradient. The remainder of the frequency encoding gradient completes spatial encoding, and can be lengthened for various other functions such as spoiling the transverse magnetization to enable lower T_R.

Relative to the spin echo sequence, GRE sequences have short T_R with many RF pulses occurring in rapid succession. Such a train of RF pulses leads to the production of additional echoes through additional signal pathways in addition to the FID signal produced following each pulse. As shown in Figure 2-6, a pulse train of only three RF pulses can result in additional signal pathways that contribute to the signal at different times. In the case of GRE sequences, due to the equal spacing of RF pulses, primary, secondary, and stimulated echoes all begin to refocus directly prior to each RF pulse. As a result, FID signals following pulses will have additional echo components added to them. Thus, at steady state, GRE sequences are said to have an FID-like signal post-excitation and an echo-like signal pre-excitation known as the S+ and S- signals respectively. Flavors of GRE can be divided into incoherent and coherent GRE sequences, the prior making use of gradient and RF spoiling to eliminate the unwanted transverse magnetization and echo signal pathways prior to each excitation and the latter using a T_R on the order of tissue T_2 to maintain transverse coherence of the signal pathways. Careful timing of gradients can enable collection of the S+ signal, the S- signal, or both together. This has implications for image weighting, as the FID-like S+ signal is generally T_2^* weighted, and the echo-like S- signal is more T_2 weighted.

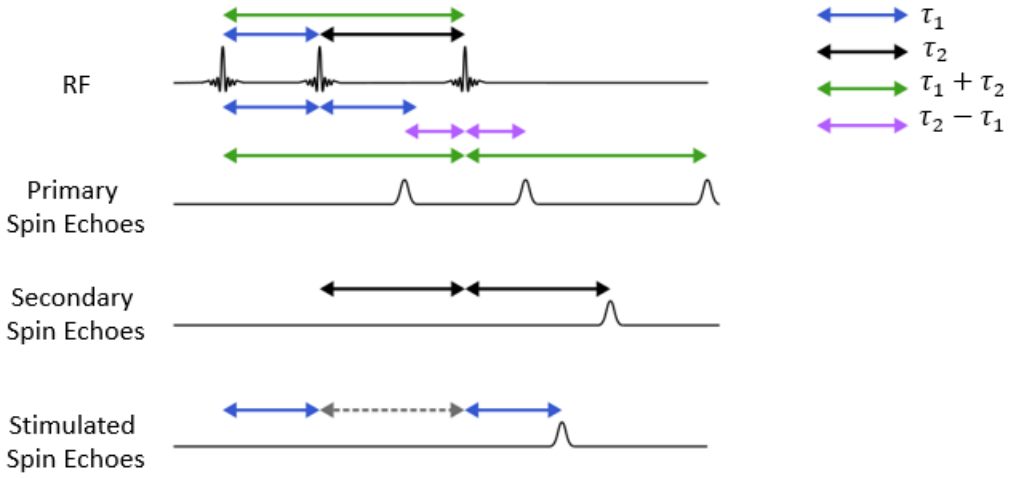

Figure 2-6 : Signal pathways resulting from a train of RF pulses of arbitrary flip angle and phase. Primary spin echoes are generated from refocusing the transverse magnetization from the first RF pulse. The locations of these echoes depend on the timing between the RF pulses and primary spin echoes themselves. Secondary spin echoes are generated from refocusing the transverse magnetization produced by RF pulses other than the first pulse. Stimulated echoes occur due to the ability of an RF pulse to store transverse magnetization as longitudinal magnetization. During the period indicated by the grey dotted arrow ($duration = \tau_2$) the transverse magnetization has been stored as longitudinal magnetization and thus does not accumulate additional phase. Once this magnetization is excited back into the transverse plane, rephasing occurs in a delayed fashion following the third RF pulse equal to the phase accumulated between the first and second pulses. FID signals (not shown) are also generated following each RF pulse, which contributes to the FID-like S+ signal in steady state sequences.

One spin-echo sequence variant, known as Rapid imaging with Refocused Echoes (RARE), Turbo Spin Echo (TSE) or Fast Spin Echo (FSE), also uses an RF echo train, but prevents signal pathways from producing secondary spin echoes by using crusher gradients around each refocusing pulse. However, stimulated echoes cannot be spoiled from the signal. Because stimulated echoes experience T_1 relaxation while the magnetization is stored along the longitudinal axis, the contribution of stimulated echoes to the TSE signal results in a mix of both T_2 and T_1 weighting. The TSE sequence is the subject of optimization in Chapter 5.

2.4: Non-Cartesian Sampling

The previous discussions primarily covered Cartesian sampling on an equispaced grid in k-space; however, equation 2-22 states that spatial encoding can be performed with any gradient input, barring scanner and safety limitations, to sample k-space with any arbitrary trajectory. Conventional Cartesian sampling has many benefits such as being directly compatible with the FFT algorithm, being highly efficient in terms of k-space coverage per unit of ADC time, and having well studied image and image artifact characteristics. However, the convenience of Cartesian sampling comes at a cost. As mentioned previously, spatial encoding in the presence of motion causes an additional accumulation of phase which prevents accurate localization of spin isochromats. While the degree of motion during frequency encoding is typically not significant, motion between phase encoding steps separated by T_R are often significant and can cause ghosting artifacts in the phase encode direction. While these ghosts can be mitigated, these techniques either require clinical controls which may have poor patient adherence or require complex reconstructions or acquisition schemes to circumvent.

Non-Cartesian acquisition schemes often sample k-space with non-uniform density and thus have aliasing patterns that appear more noise-like rather that the coherent aliasing artifacts in Cartesian sampling. As a result, non-Cartesian trajectories can generally tolerate higher undersampling factors with parallel imaging. In addition, undersampling with non-Cartesian trajectories occurs in multiple directions, making better use of coil geometries.

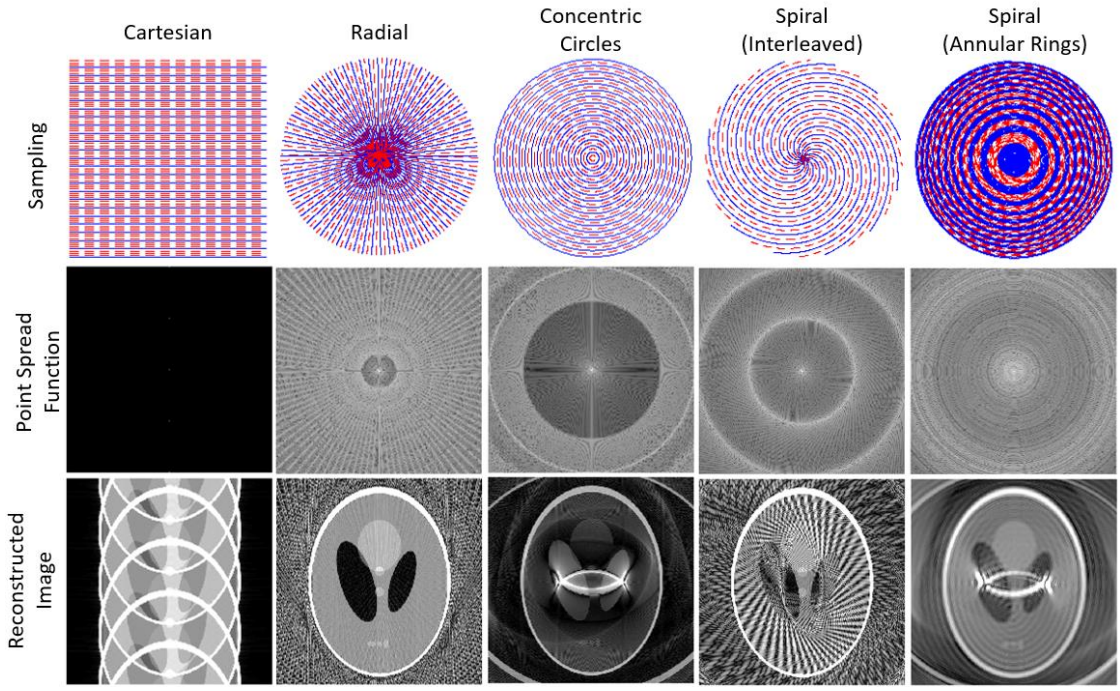

Figure 2-7: Undersampled (R=4) k-space trajectories for Cartesian, radial, concentric rings, spiral interleaved, and spiral annular rings are shown here (top row). Collected data are shown as solid blue lines and uncollected data are shown as dashed red lines. Point spread function (PSF) of each undersampled trajectory are also shown in log scale (middle row). Zero-filled phantom reconstruction using undersampled k-space trajectories are shown as well (bottom row). Note that aliasing patterns for non-Cartesian trajectories do not result in coherent replicas of the images, as in the Cartesian case. However, aliasing artifacts do obscure parts of the image depending on the sampling trajectory.

The work in this thesis focuses primarily on projection sampling (also known as radial sampling) and spiral sampling. As shown in Figure 2-7, the radial trajectory involves sampling k-space via spokes that pass through k_0[18,28]. Radial sampling results in a non-uniform sampling density over k-space resulting in oversampling of the center of k-space and undersampling at the periphery. Due to it's relatively lower sampling density at the periphery of k-space, radial imaging typically requires more acquisition shots to achieve the same resolution and field of view of a Cartesian image. However, radial sampling does not have a specific phase encoding direction, thus artifacts from motion or undersampling appear more diffuse over the image domain and form streaking artifacts rather than coherent ghosts or aliases. Radial sampling's reduced sensitivity to motion and

tolerance of undersampling make it suitable for imaging physiological motion, with residual motion and aliasing artifacts following motion correction or parallel imaging being particularly diffuse and unobtrusive[28,29]. Radial sampling also redundantly acquires the center of k-space which can be useful for self-gating[30] or self-navigation[31]. Sufficiently high acceleration factors can even acquire images with sufficient temporal resolution to resolve motion without motion correction, enabling free-breathing ungated acquisition[32].

Spiral trajectories can take a variety of potential shapes[17,33,34] that can be designed for a variety of different applications such as motion insensitivity[35], improved SNR[36], self-navigation[37], flow compensation among many other functions. Like radial sampling, spiral sampling also does not have a distinct phase encoding direction, and has similarly diffuse aliasing and motion artifacts (Figure 2-7). One distinct benefit of spiral sampling is the ability to design the sampling density, shape, and number of interleaves of the trajectory, enabling considerable flexibility in trajectory function. However, spiral readouts are typically longer due to gradient maximums and slew rate limitation than either Cartesian or radial readouts, making them more prone to off-resonance blurring. Thus trade-offs must be made between acquisition time, resolution, and off-resonance tolerance when designing a spiral trajectory.

The aliasing patterns seen in all undersampled images are dependent on the direction in k-space that is undersampled. In Cartesian sampling, as shown in Figure 2-7, undersampling occurs in the k_y direction, which results in replicas in regular intervals in the y-direction of the image domain. Because the

undersampling is uniform through k-space, the resulting aliasing artifacts are coherent. Accelerated radial data are undersampled in the k_θ direction but fully sampled in k_r. The sampling density near the center of k-space, k_0, meets the Nyquist criterion but the sampling density at the edge of k-space is low. Thus, high frequencies at specific angles are lost from the image resulting in aliased streaks at those unsampled projection angles which can be seen in the point spread function. These radial streaks often appear as a more benign aliasing pattern than Cartesian undersampling which only mildly obscures image details. In comparison to radial sampling, concentric ring sampling instead is undersampled in k_r and fully sampled in k_θ. The resulting aliasing artifacts are then radially symmetric, as shown in the point spread function, and fold over from the opposite side of the object. This can be seen in the image, as the top, bottom, and sides of the phantom fold over radially and appear as an artifact in the center of the field of view. Similarly, the phantom edges fold over and form a symmetric circular ring at the edge of the image. Spiral sampling patterns can be seen as a range of intermediate trajectories between radial and concentric circles. The interleaved spiral pattern requires multiple rotated shots akin to radial spokes. However, because of rotation in the trajectory, spirals also resemble concentric rings. Undersampled interleaved spiral trajectories are thus undersampled in both k_θ and k_r and have aliasing characteristics of both the radial and concentric circles trajectories, which can be observed in both the point spread function and the zero-filled reconstruction. The design of the spiral trajectory can control the radial-like or circle-like undersampling pattern, with a

spiral trajectory designed with a large number of interleaves having aliasing patterns akin to radial and long single-shot spirals having aliasing patterns akin to concentric circles. The spiral annular rings sampling pattern is one such extreme, using a single shot spiral trajectory that is broken up into multiple shots that sample ring-like portions of k-space. The resulting undersampling pattern resembles variable density undersampling using concentric circles, and as a result, the undersampled image has prominent radial fold-over as shown by the circular shape of the point spread function, and the aliasing artifact in the center of the field of view.

Both radial and spiral sampling have reconstruction challenges not required of Cartesian sampling. Non-Cartesian sampling schemes require a non-uniform fast Fourier transform (NUFFT) for image reconstruction, which is often performed via a process called gridding[38–40]. Gridding uses the collected non-Cartesian points to interpolate the values of the underlying Cartesian grid. The resulting interpolated Cartesian k-space is reconstructed with a FFT to produce an image. The computational complexity of a NUFFT is $O\left(N \cdot log\, N\, +\, N\, \cdot\, log\left(\frac{1}{\varepsilon}\right)\right)$ in comparison to the complexity of the FFT which is $O(N \cdot log\, N\,)$, thus leading to longer reconstructions for non-Cartesian data.

2.5: Parallel Imaging

Parallel imaging[15,16,41,42] is an approach used to reconstruct unaliased MR images from undersampled data by exploiting the additional spatial information inherent to data acquisition from multiple “parallel” receiver coils. Because the acquisition time of an MR image scales with the number of phase encoding steps

required for a fully sampled image, undersampling along the phase encoding axis can greatly decrease the acquisition time. This section will discuss two parallel imaging methods, SENSE and GRAPPA, that reconstruct undersampled data in the image domain and in k-space respectively.

SENSitivity Encoding or SENSE is a method to reconstruct undersampled data in the image domain by using coil sensitivity maps to unfold aliased images[43]. Each pixel in an aliased reduced FOV image has signal superimposed from multiple locations in the full FOV image. This aliasing occurs identically in each detector coil; however, the signal from the superimposed points are weighted by the coil sensitivity when aliased. Thus, for each coil i, the signal at the aliased point P_i for coil i is:

$$P_i = \sum_{k=1}^{N_p} S_{i,k} I_k \tag{2-35}$$

Where N_p is the number of superimposed points, $S_{i,k}$ is the coil sensitivity at each superimposed point k for coil i and I_k is the signal in the unaliased full FOV image at superimposed point k. The location of each superimposed point I_k is known due to the regularity of aliasing with a uniformly undersampled Cartesian trajectory, with aliases separated by $\frac{FOV}{R}$ where R is the undersampling factor. Because P_i and $S_{i,k}$ are also known, for each aliased point P, a system of N_c equations can be solved for all superimposed points I_k. This system is overdetermined if $N_c > N_p$, thus the least squares optimization finds the optimal solution to the matrix equation:

$$v = Ua \tag{2-36}$$

Where v is the vector of length $\mathrm{N_p}$ containing the separated signals from all the superimposed points, a is a vector of size $\mathrm{N_c}$ containing the aliased signals P_i for each coil I, and U is the least squares optimal unfolding matrix that takes the form:

$$U = (S^H \Psi^{-1} S)^{-1} S^H \Psi^{-1} \tag{2-37}$$

Where S is the sensitivity matrix containing the coil sensitivities at each superimposed point and Ψ is the noise covariance matrix between all the detector coils. The SENSE algorithm is outlined in Figure 2-8.

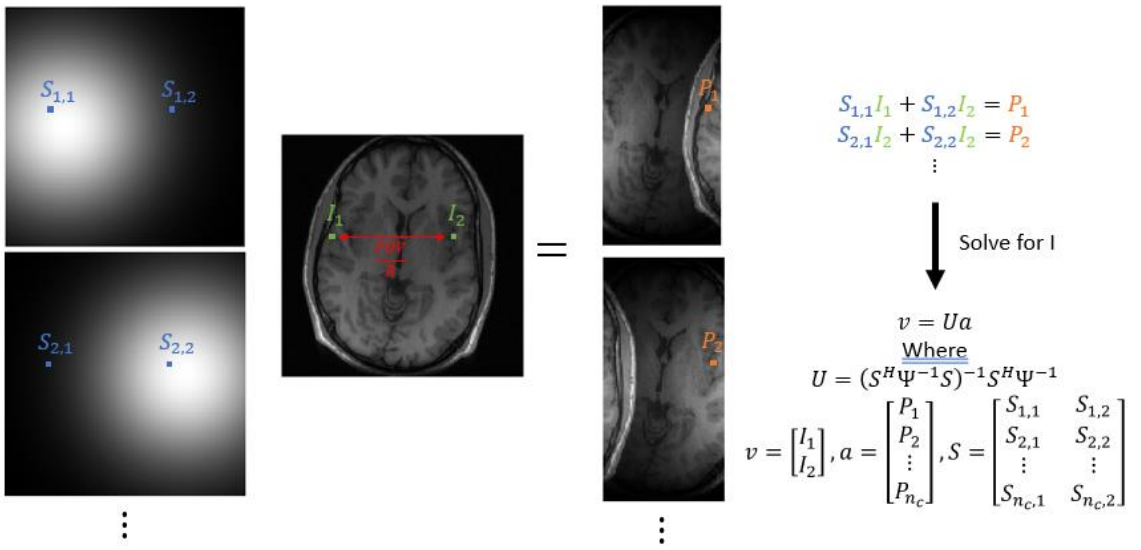

Figure 2-8: The SENSE algorithm is shown for an acceleration factor of 2 with phase encoding in the left-right direction. Aliased pixels in the undersampled coil images (P_1,P_2) have signal folded over from two locations in the unaliased image. These aliased points are separated by a distance equal to the FOV over the acceleration factor R (in this case R=2). These locations have corresponding coil sensitivity values. Using a system of linear equations shown on the right, a matrix inverse operation can be used to solved for a composite unaliased image.

To perform a SENSE reconstruction, prior knowledge of the coil sensitivities is required, and accurate coil sensitivities are necessary for a high-quality reconstruction. Non-Cartesian trajectories have irregular aliasing patterns and require iterative conjugate gradient minimization to unfold the aliased images[44].

Another parallel imaging technique known as GeneRalized Autocalibrating Partial Parallel Acquisition or GRAPPA instead reconstructs data in the k-space domain[45]. GRAPPA builds on Simultaneous Acquisition of Spatial Harmonics (SMASH) which demonstrated that sinusoidal coil sensitivities can be leveraged to perform k-space shifts that mimic phase encoding[46]. This is done with a set of weights that form a linear combination of coil sensitivities which allow the lines of k-space to be shifted to uncollected phase encoding locations. The original SMASH algorithm required prior knowledge of the coil sensitivities and demanded specific coil configurations to generate the requisite composite sinusoidal coil sensitivities. AUTO-SMASH[47] and VD-AUTO-SMASH[48] eliminated these restrictions, instead requiring a portion of k-space to be fully sampled to serve as an auto-calibration signal (ACS) to solve for reconstruction weights within k-space. GRAPPA generalizes the process of VD-AUTO-SMASH, solving for weights that reconstruct missing phase encoding lines for each individual coil rather than a composite coil signal. The resulting reconstructed coil images are combined to obtain a final image in contrast to SENSE and older SMASH methods which generate combined images. A schematic representation of GRAPPA is shown in figure

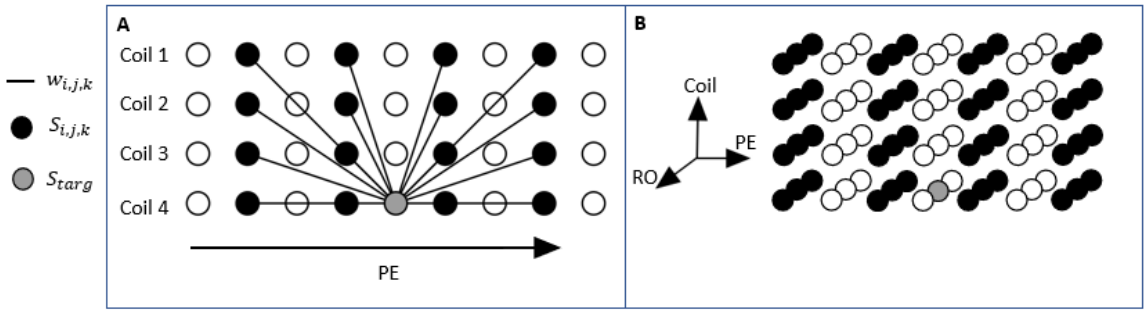

$$S_{targ} = \sum_{i}^{Coil} \sum_{j}^{PE} \sum_{k}^{RO} w_{i,j,k} S_{i,j,k}$$

Figure 2-9: A schematic representation of the GRAPPA algorithm. (A) Data from multiple coils is multiplied by a weight kernel to generate a single target point within a single coil. (B) Shown is the three dimensional representation of the GRAPPA source point locations, illustrated without GRAPPA weights. The value of the target point is generated by multiplying source points by the GRAPPA weights. Within a single coil image, the GRAPPA kernel is shifted to reconstruct all the missing lines. A separate kernel is required for each coil image.

The GRAPPA algorithm reconstructs uncollected k-space locations in the undersampled data by utilizing GRAPPA weights which can be represented in matrix form as:

$$\tilde{S}_{targ} = S_{src} \cdot w \tag{2-38}$$

Where S_{src} corresponds to the collected points in the undersampled data, $\tilde{S}_{targ}$ refers to the target points that are not acquired but are to be estimated with GRAPPA, and w are the GRAPPA weights. From the ACS data, the weights are calculated with a least squares approximation using the Moore-Penrose pseudo-inverse as follows:

$$w = S_{ACS-targ} \cdot pinv(S_{ACS-src}) \tag{2-39}$$

where $S_{ACS-src}$ are the source points and $S_{ACS-targ}$ are the target points found in the ACS data corresponding to collected and uncollected lines of k-space in the under sampled data. The number of equations in this linear system is equal to the number of GRAPPA kernel repetitions in the ACS data, and the number of

unknown variables is equal to the number of points in the GRAPPA kernel (i.e. the kernel size x the number of receiver channels). To produce a unique solution, the number of known equations must be equal to or greater than the number of unknown variables. A new equation can be generated by shifting the GRAPPA kernel within the ACS data to obtain a new kernel repetition, as the GRAPPA weights are invariant to k-space location if the kernel geometry does not change. The minimum number of kernel repetitions required to calculate the GRAPPA weights is

$$Repetitions > N_{kr}N_{kp}N_c \tag{2-40}$$

Where N_{kr} and N_{kp} are the GRAPPA kernel dimensions in the readout and phase encoding directions and N_c is the number of coils. An overdetermined system will reduce any bias in the weight computation by preventing overfitting of correlated noise or coil imperfections thus in practice more ACS data is collected to have a larger number of kernel repetitions. In Cartesian GRAPPA, the acquisition of a few additional central lines of k-space provides hundreds of kernel repetitions with high SNR enabling a robust reconstruction with fewer artifacts.

Chapter 3 Optimization of Through-time Radial GRAPPA with Coil Compression and Weight Sharing

The results presented in this chapter have been published in an original research article in Magnetic Resonance in Medicine.

In this chapter, a non-Cartesian parallel imaging technique, through-time radial GRAPPA, is optimized to reduce ACS acquisition time and GRAPPA weight calibration time to enable online reconstruction at the scanner in a clinically feasible timeframe. Utilizing radial GRAPPA as opposed to Cartesian GRAPPA allows for free-breathing ungated scans, but variable GRAPPA kernel geometry demands calibration of unique GRAPPA weights for each kernel location in k-space, which requires additional calibration data and computational demand. Coil compression is a data compression technique that both reduces the need calibration data and improves reconstruction performance. In addition, weight sharing reduces the number of unique GRAPPA weights to compute, further improving the reconstruction performance. Optimized parameters for coil compression and weight sharing applied to reconstructions enables images to be collected with a temporal resolution of 66ms/frame and spatial resolution of 2.34mm x 2.34mm while reducing calibration acquisition time from 34s to 6.7s, weight calculation time from 200s to 3s, and weight application time 18s to 5s.

3.1: Developments in Cardiac Cine MR Imaging

Cardiac cine MRI is a well-established dynamic imaging technique with high spatial and temporal resolution to assess both cardiac structure and physiological motion[49]. In clinical practice, cardiac cine is a precise and reproducible method

for assessment of function and mass of both ventricles though the cardiac cycle. In comparison to other approaches to functional assessment of the heart, cardiac MR is non-invasive, does not use ionizing radiation, and provides superior soft tissue contrast with more possible imaging planes. For these reasons, cardiac cine is considered to be the gold standard for clinical assessment of cardiac function[50].

Despite the success of cardiac cine, patient pathologies can reduce the quality of acquired images. To eliminate motion artifacts, a long acquisition through multiple cardiac cycles is performed with retrospective ECG gating to obtain enough data to resolve motion during each cardiac phase. Due to the long acquisition time, multiple breath-holds are required to eliminate respiratory motion. However, cardiac dysrhythmia can reduce the accuracy of cardiac gating and introduce motion artifacts into acquired images and non-cooperative patients such as children or patients with dyspnea are unable to perform the long breath-holds required for high-quality cardiac cine. Thus, imaging failure due to motion artifacts is a challenge with cardiac cine.

Real-time cardiac imaging techniques have been proposed that do not require breath holds or ECG gating by using rapid data sampling and image reconstruction methods, such as parallel imaging and compressed sensing.[51–55] Non-Cartesian parallel imaging techniques have enabled free-breathing and ungated cardiac imaging with comparable image quality to conventional Cartesian cine[32,56]. Radial and spiral sampling trajectories oversample the signal-rich central region of k-space reducing their sensitivity to motion-related artifacts.

In addition, undersampled non-Cartesian trajectories often produce less obtrusive aliasing artifacts than their Cartesian counterparts, enabling higher acceleration factors and, thus, improved temporal resolution to resolve motion. One such non-Cartesian parallel imaging-based approach for rapid cardiac imaging is through-time radial GRAPPA which has been previously deployed for real-time imaging[57–61] due to its low reconstruction latency (<1s).

However, through-time radial GRAPPA requires several fully sampled datasets to calibrate GRAPPA weights, resulting in lower acquisition efficiency. Reported implementations of through-time radial GRAPPA have typically required between 25s[57] to up to 150s[61] per slice for the collection of this calibration data, though calibration times have been reduced to 2.6s[32] by using large reconstruction segment sizes that may introduce blurring and artifacts that can degrade image quality. Longer GRAPPA calibration acquisition may be acceptable in interventional applications[57] where a single calibration scan can be used to reconstruct multiple accelerated acquisitions. In contrast, cardiac cine not only is acquired in a single acquisition, but also requires several slices for ventricular coverage, each slice requiring a new calibration scan. Thus, while capable of generating high-quality cardiac images, through-time radial GRAPPA is inefficient for cardiac cine imaging; reduction of the acquisition time for calibration data without loss of image quality could facilitate the deployment of through-time radial GRAPPA for functional cardiac imaging in the clinic[62].

In addition, growing multichannel receiver arrays and an increasing demand for higher resolution[63–66] place additional computational burden on through-time

radial GRAPPA reconstructions. Previously reported real-time applications[57] have demonstrated reconstruction latencies of <1s only during application of the GRAPPA weights, as the calculation of GRAPPA weights are performed only once and do not contribute significantly to the overall reconstruction efficiency. However, compared to GRAPPA weight application, GRAPPA weight calculation is far more computationally intensive and is a major contributor to reconstruction latency for cardiac functional imaging.

Thus, the purpose of this work is to minimize calibration acquisition and GRAPPA weight computation time for through-time radial GRAPPA without impacting image quality. PCA coil compression and weight sharing are the two approaches explored in this work to meet this goal. As both calibration acquisition time and reconstruction latency scale with receiver array size, PCA coil compression can potentially reduce both calibration acquisition time and reconstruction latency while retaining the SNR and encoding benefits of a large array. In addition, reusing GRAPPA weights across small regions of k-space reduces the number of GRAPPA weights required and can thus reduce the time spent on calculating the GRAPPA weights. Calibration acquisition time and GRAPPA weight calculation time is compared between previously reported through-time radial GRAPPA reconstructions and optimized reconstructions with coil compression and weight sharing. In addition, image RMSE of reconstructions with different settings are compared to determine if coil compression or weight sharing can be performed without loss of image quality.

3.2: Through-time Radial GRAPPA

Theory

In radial GRAPPA, and many other non-Cartesian GRAPPA implementations, the relationship between the source and target points is different in different areas of k-space, and thus the GRAPPA kernel, and associated weights, also differs across k-space. As a result, a unique set of weights must be computed for each kernel geometry.

In through-time radial GRAPPA, multiple fully sampled datasets are collected and used as calibration data. However, acquiring a sufficient number of kernel repetitions solely from repeated fully-sampled data results in a long acquisition time for the calibration data. The original work on through-time radial GRAPPA proposes a hybrid method which takes calibration data over a small (often 8x1) k-space segment to reduce the number of fully-sampled calibration frames which must be collected[59,61]. The lower bound of calibration frames needed to estimate the GRAPPA weights can be written as:

$$CalibrationFrames > \frac{N_{kr}N_{kp}N_c}{N_{rseg}N_{pseg}} \quad (3\text{-}1)$$

Where N_{rseg} and N_{pseg} are the k-space segment sizes used for calibration in the readout and phase encoding directions respectively.

PCA coil compression is a dimensionality reduction technique along the coil dimension that has been used to improve image SNR and reduce reconstruction time[63–66]. When applied to through-time GRAPPA, PCA coil compression also reduces the lower bound of calibration frames required to estimate the GRAPPA weights as shown in equation 3-1. We hypothesize PCA coil compression will significantly reduce the number of calibration frames

needed for through-time radial GRAPPA, thereby reducing the acquisition time, which is a limiting factor in efficient implementation of radial GRAPPA in clinical practice.

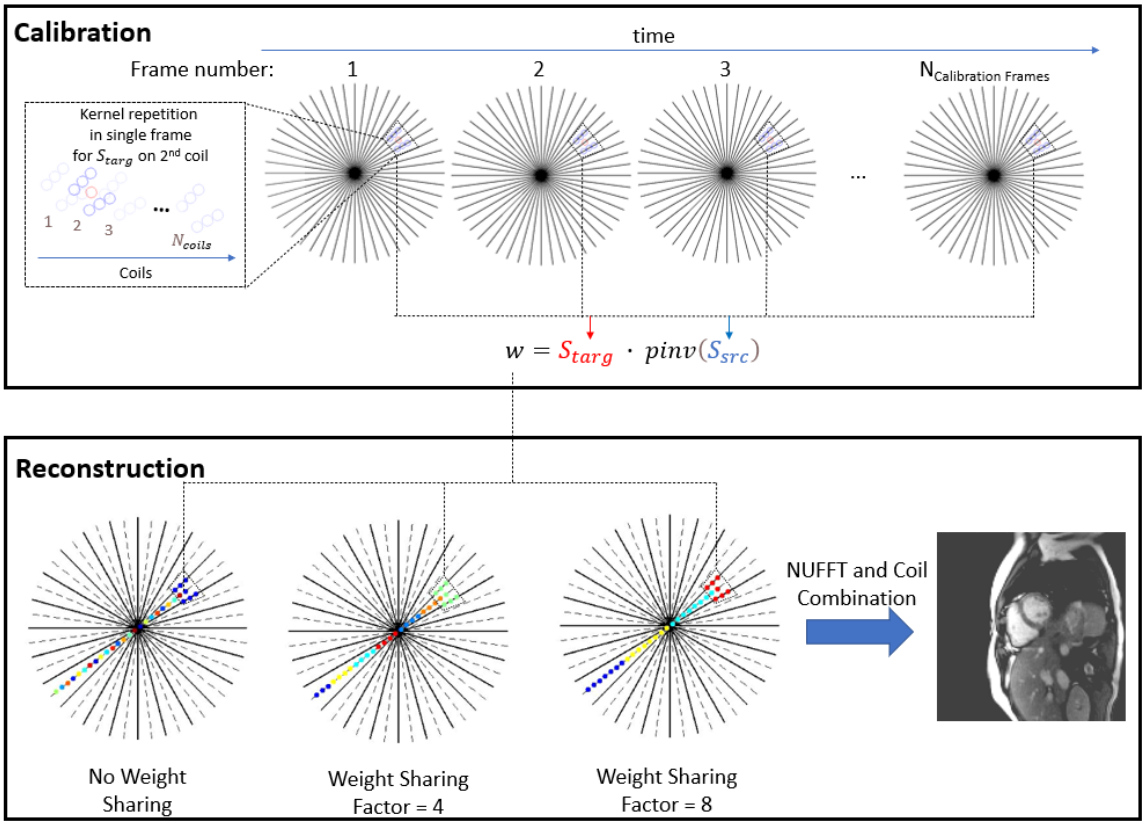

Figure 3-1: Schematic of through-time radial GRAPPA, divided into calibration and reconstruction steps. In the calibration step, GRAPPA weights are generated using ordinary least squares using source points (shown in blue) and target points (shown in red). In this calibration schematic, a single unique weight set is generated from the highlighted source and target points. In the reconstruction step, the weight set generated in the calibration step is applied to three separate reconstructions schema, which are shown to illustrate the differences between reconstructions with and without weight sharing. On the left, a conventional through-time radial GRAPPA reconstruction is performed, with each target point reconstructed with a unique weight set (represented as target points of different colors). In the middle, GRAPPA weights are shared between four locally adjacent target points in the readout direction, corresponding to a weight sharing factor of four. The target points reconstructed with the same weight set are shown as a single color. On the right, an example of a weight sharing factor of eight is shown, with eight target points reconstructed with a single weight set. Regardless of the reconstruction method used, the resulting reconstructed k-space resembles fully sampled data and is reconstructed using NUFFT and coil combination.

In radial GRAPPA, the relationship between each target point and source point kernel in k-space is unique. However, computing a set of GRAPPA weights for each missing point in an undersampled radial dataset is a computationally intensive reconstruction step due to the need for repeated pseudoinverse

operations. A diagram detailing this algorithm can be found in Figure 3-1. While every GRAPPA kernel in radial k-space is unique, kernels that are locally adjacent are geometrically similar, and the GRAPPA weights can be assumed to be approximately the same. Thus, one weight set could be applied to reconstruct several adjacent target points, and the number of unique GRAPPA weights required for a complete reconstruction could be reduced, in turn reducing the GRAPPA weight computation time. The “weight sharing factor” is the is the number of target points reconstructed with a single GRAPPA weight set. Note that weight sharing is distinct from the use of k-space segments for calibration, where several kernel repetitions are collected over a region of k-space to estimate the GRAPPA weights.

3.3: Data Acquisition and Analysis

In vivo cardiac data were collected from 15 healthy volunteers in an IRB approved study on a 1.5T Sola Siemens MRI scanner using a 30-channel body receiver array. A total of 400 frames of calibration data were collected during free-breathing with no ECG-gating in the short axis orientation using a radial bSSFP readout with the following imaging parameters: 128x128 matrix, 144 radial projections, 256 readout points per projection, TR/TE=2.94/1.48ms, 37^{o} flip angle, 8mm slice thickness, $300mm^2$ FOV. Following the collection of calibration data, ten seconds of accelerated data were collected with a similar imaging protocol using acceleration factors of 4, 6, 9 and 12 (36, 24, 16, and 12 projections, respectively), resulting in temporal resolutions of 100ms/frame, 67ms/frame, 44ms/frame, and 36ms/frame respectively.

Gold Standard Reconstruction

A gold standard image for each acceleration factor was generated via through-time radial GRAPPA reconstruction of collected undersampled data using 400 calibration frames, no k-space segmentation for calibration (1x1 segment), and a 3x2 GRAPPA kernel (in read and projection directions respectively)[61]. Following through-time radial GRAPPA reconstruction, a non-uniform Fast Fourier Transform (NUFFT) from the MIRT toolbox[67] was performed and coils were combined using adaptive combination[68].

Impact of Coil Compression on Required Calibration Data

The radial k-space data, with 30 independent receiver channels, were projected onto a virtual coil subspace at each k-space location using a linear PCA coil compression algorithm[64,69,70]. The through-time radial GRAPPA reconstruction was performed using truncated subsets of the virtual coil space, from 30 virtual coils to 8 virtual coils, with 30 virtual coils accounting for 100% of the signal from the original data. Signal content of the compressed data is defined as the sum of the singular values of the virtual coil subset over the total sum of all singular values. Reconstructions were also performed at specific compression levels (95%, 90%, 80%), defined as the smallest number of virtual coils to needed exceed a signal content threshold. For our system, these compression levels corresponded to 16, 12, and 8 virtual coils.

Through-time radial GRAPPA reconstructions were performed with a 8 x 1 (read x projection) k-space segment size and 3x2 kernel size, as suggested in Seiberlich, et al.[61]. For each virtual coil subset, the number of calibration frames

employed to generate GRAPPA weights was monotonically decreased from 80 to the lower bound described by equation 3-1. Any fewer frames would result in the GRAPPA calibration being underdetermined, where a unique solution for the weights cannot be calculated. In addition, reconstructions where the number of coils were insufficient to perform parallel imaging at a given acceleration factor were not considered.

Image quality of accelerated acquisitions was quantified by calculating the root mean squared error (RMSE) between grayscale normalized gold standard and reconstructed images in an ROI drawn around the heart.

Impact of GRAPPA Weight Sharing on Reconstruction Time and Quality

The through-time radial GRAPPA reconstruction algorithm was modified such that a single GRAPPA weight set was used to estimate multiple target points along the same radial projection. The extent of weight sharing was varied from no weight sharing (weight sharing factor of one, where each target point was associated with a unique weight set) to weight sharing over 32 points (weight sharing factor of 32) for all acceleration factors. Reconstructions with weight sharing were performed with no coil compression and 80 calibration repetitions to assess image quality changes due to weight sharing independently of coil compression. Image quality was assessed by computing the RMSE between images reconstructed with weight sharing and previously described gold standard images.

Reconstruction with Coil Compression and Weight Sharing

A set of reconstruction parameters were chosen based on coil compression and weight sharing results that demonstrated improved calibration acquisition and reconstruction time performance with minimal image quality degradation. The parameters selected were 12 virtual coils, 16 calibration frames, and a weight sharing factor of 8. Reconstructions with the selected optimized parameters were performed at acquired acceleration factors and were compared to the gold standard reconstruction via RMSE.

Reconstruction Performance

All reconstructions were performed on a dual 12-core Intel Xeon Silver 4214 platform with 128GB of RAM. Reconstruction times for through-time radial GRAPPA with coil compression and weight sharing were normalized to the most computationally intensive reconstruction (no coil compression, no weight sharing, 80 calibration frames). Reconstruction times were subdivided into the three most computationally intensive tasks: Non-uniform fast Fourier transform (NUFFT), GRAPPA weight calculation, and GRAPPA weight application.

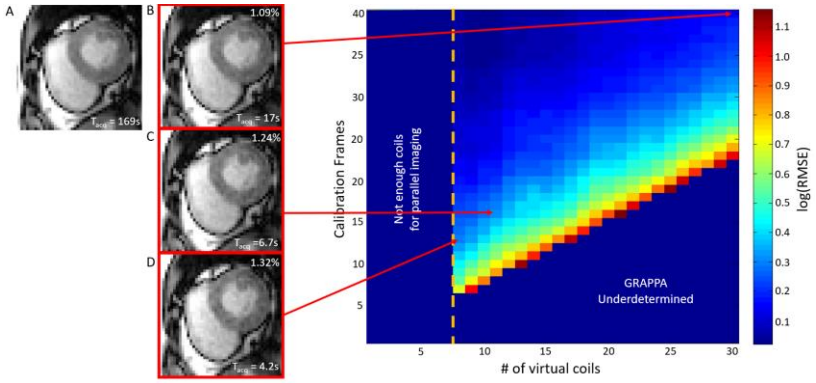

Figure 3-2: Right: A representative heatmap indicating the log(RMSE) between the gold standard and reconstructions performed with a specific number of virtual coils and calibration frames for R=8. Left: The gold standard image for this heat map is shown as image A. Images B, C and D correspond to reconstructions from specific regions of the heatmap with similar RMSE and are reconstructed with coil compression to signal content of 100%, 90%, and 80% respectively. The acquisition time of the calibration data (T_{acq}) is shown in the bottom right of each image. The RMSE between the gold standard and each reconstruction is shown on the top right of each image.

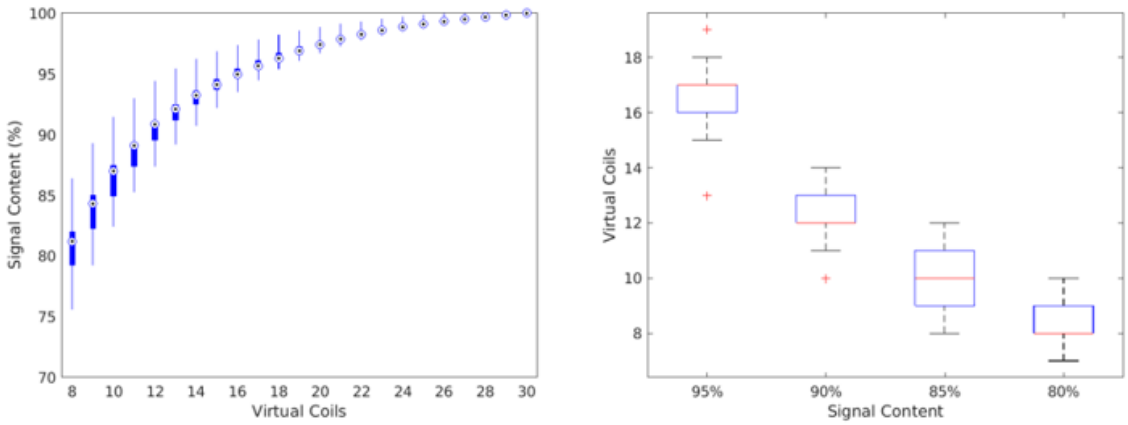

Figure 3-3: Left: A series of boxplots indicating the signal content remaining after coil compression to a specific virtual coil count. Each boxplot represents information from N=15 healthy subjects. The median is shown as a white circle with a central blue dot, the interquartile range is shown as a thick blue box, and the minimum and maximum values are shown as whiskers extending from the interquartile range. Right: A series of boxplots indicating the number of virtual coils required to yield a specific signal content threshold. The median is shown as a red line, the interquartile range is shown as a blue box, and the minimum and maximum are shown as whiskers extending from the interquartile range. Outliers beyond 1.5x the interquartile range are shown as red pluses.

3.4: Results

Figure 3-2 shows a heatmap of the RMSE values for reconstructions performed across the range of coil compression factors and calibration frames for a single subject at acceleration factor of 8. Figure 3-3 shows boxplots demonstrating that signal content at specific compression levels is consistent across the 15 volunteers. Going from right to left, decreasing the number of virtual coils (e.g. decreasing the signal content threshold) improves the RMSE for a given number of calibration frames. Going from top to bottom, decreasing the number of calibration frames worsens the image quality, with a sharp increase in RMSE as the GRAPPA weight equation approaches being exactly determined (as described in equation 13-). Representative images from the heatmap, together with the gold standard reconstruction (Figure 3-2a, 1x1 segment, 30 coils, 400 calibration frames), are also shown. Figure 3-2b shows a reconstruction with no coil compression (8x1 segment, 30 coils, 40 calibration

frames). Figure 3-2c shows a reconstruction with coil compression to a 90% signal content threshold (8x1 segment, 12 coils, 16 calibration frames). Figure 3-2d shows a reconstruction with coil compression to an 80% signal content threshold (8x1 segment, 8 coils, 12 calibration frames). Compared to the gold standard, the reconstructed images have comparable image quality, with RMSE of 1.09% for the reconstruction with no coil compression, 1.24% for the reconstruction with coil compression toa 90% signal content threshold, and 1.32% for the reconstruction with coil compression to an 80% signal content threshold. In addition, the total acquisition time of the calibration data required to perform the reconstruction with coil compression is reduced from 17s to 4.2s per slice.

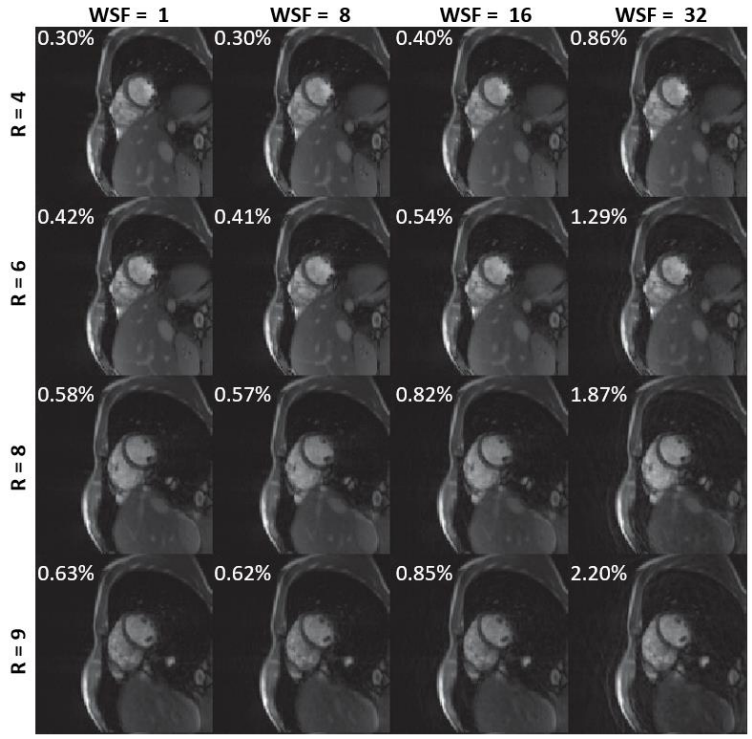

Figure 3-4 Reconstructed images over a range of weight sharing factors and acceleration factors. Images were reconstructed with no coil compression and 80 calibration frames. The leftmost column of images was reconstructed with no weight sharing, equivalent to a weight sharing factor of one. The RMSE between the gold standard and reconstructed image is shown on the top left of each image.

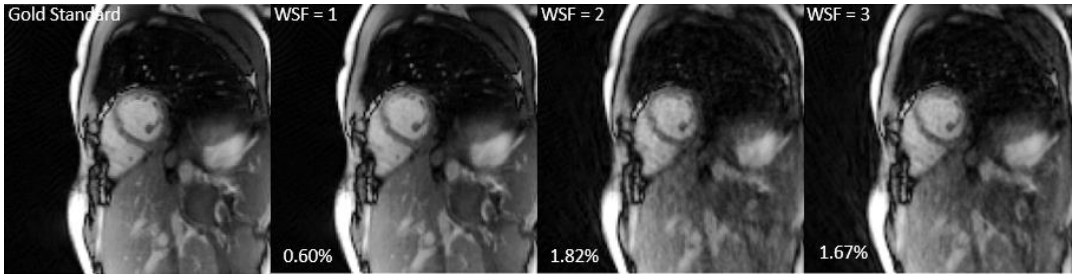

Figure 3-5 Reconstructions performed with weight sharing in the projection direction for acceleration factor of 8. Relevant images have RMSE compared with the gold standard in the bottom left corner. Left: Gold standard reconstruction. Middle Left: Reconstruction with 30 virtual coils, 40 calibration frames, and no weight sharing. Middle Right: Reconstruction with 30 virtual coils, 40 calibration frames, and WSF=2 in the projection direction. Right: Reconstruction with 30 virtual coils, 40 calibration frames, and WSF=3 in the projection direction.

Diastolic images from a matrix of reconstructions at acceleration factors of 4,6,8 and 9 with weight sharing factors of 1, 8,16, and 32 along the readout direction are shown in Figure 3-4. In addition, diastolic images at acceleration factor of 8 with weight sharing factors of 1,2, and 3 in the projection direction are shown in Figure 3-5 for comparison. All reconstructions are performed with no coil compression and 80 calibration frames. Reference images with no weight sharing are shown on the left and labeled with a weight sharing factor of 1. The RMSE of the reconstruction increases along with both acceleration factor and the weight sharing factor. All reconstructions with a weight sharing factor of 8 in the readout direction have similar RMSE to the reference. A weight sharing factor of 32 leads to artifacts and loss of image quality across all acceleration factors. In the projection direction, weight sharing factor of 2 leads to artifacts and global loss of image quality and is comparable to image quality loss at a weight sharing factor of 32 in the readout direction.

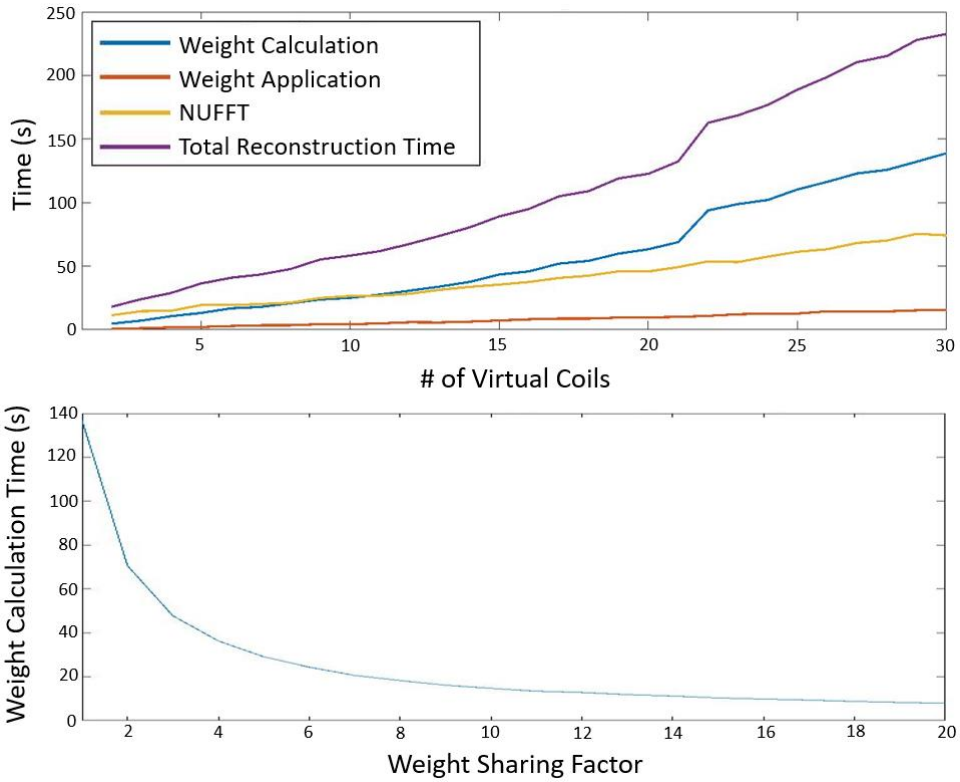

Figure 3-6 (Top) A representative plot showing the total reconstruction time (purple) for reconstructions with varying numbers of virtual coils at an acceleration factor of 9. All reconstructions were performed with 80 calibration frames. The calculation time of the GRAPPA weights is shown in blue and the reconstruction time, where the weights are applied to reconstruct undersampled data, is shown in red. Time taken to perform radial gridding is shown in yellow. Other computational tasks, such as data transfer or IO overhead, are negligible compared to GRAPPA and NUFFT time. (Bottom) A representative plot showing the reduction in weight calculation time due to weight sharing at an acceleration factor of 9. Weight sharing does not impact NUFFT or weight application time.

Figure 3-6 shows the radial GRAPPA reconstruction performance improvements associated with coil compression and weight sharing. With no coil compression, the reconstruction time was 237s. At a 95% coil compression level (16 coils), the reconstruction time is reduced to 104s. At a 90% coil compression level (12 coils), the reconstruction time is reduced to 68s. The primary contributor to these performance improvements is the reduction of weight calculation time. While weight sharing does not impact NUFFT or weight application performance, it does affect the weight calculation time, as shown in the bottom plot of Figure 3-6. A weight sharing factor of 8 reduces the time required to calculate the

GRAPPA weights from 134s to 18s, an 86.6% reduction in weight computation time, independent of coil compression.

In Figure 3-7 and Figure 3-8, systolic and diastolic images are shown in three representative healthy subjects at acceleration factors of six and nine respectively (frame rates of 15 frames/s and 27.5 frames/s) and compared between optimized reconstructions with coil compression and weight sharing, and reconstructions without. The associated calibration data acquisition of optimized reconstructions was obtained retrospectively from the gold standard dataset and could be collected in 6.77s/slice compared to reconstructions with 80 calibration frames, where calibration data are acquired in 34s/slice. In addition, weight computation time for the optimized reconstructions was reduced from 201s to 3.1s per slice for an acceleration factor of 6, and 144s to 2.0s per slice for an acceleration factor of 9.

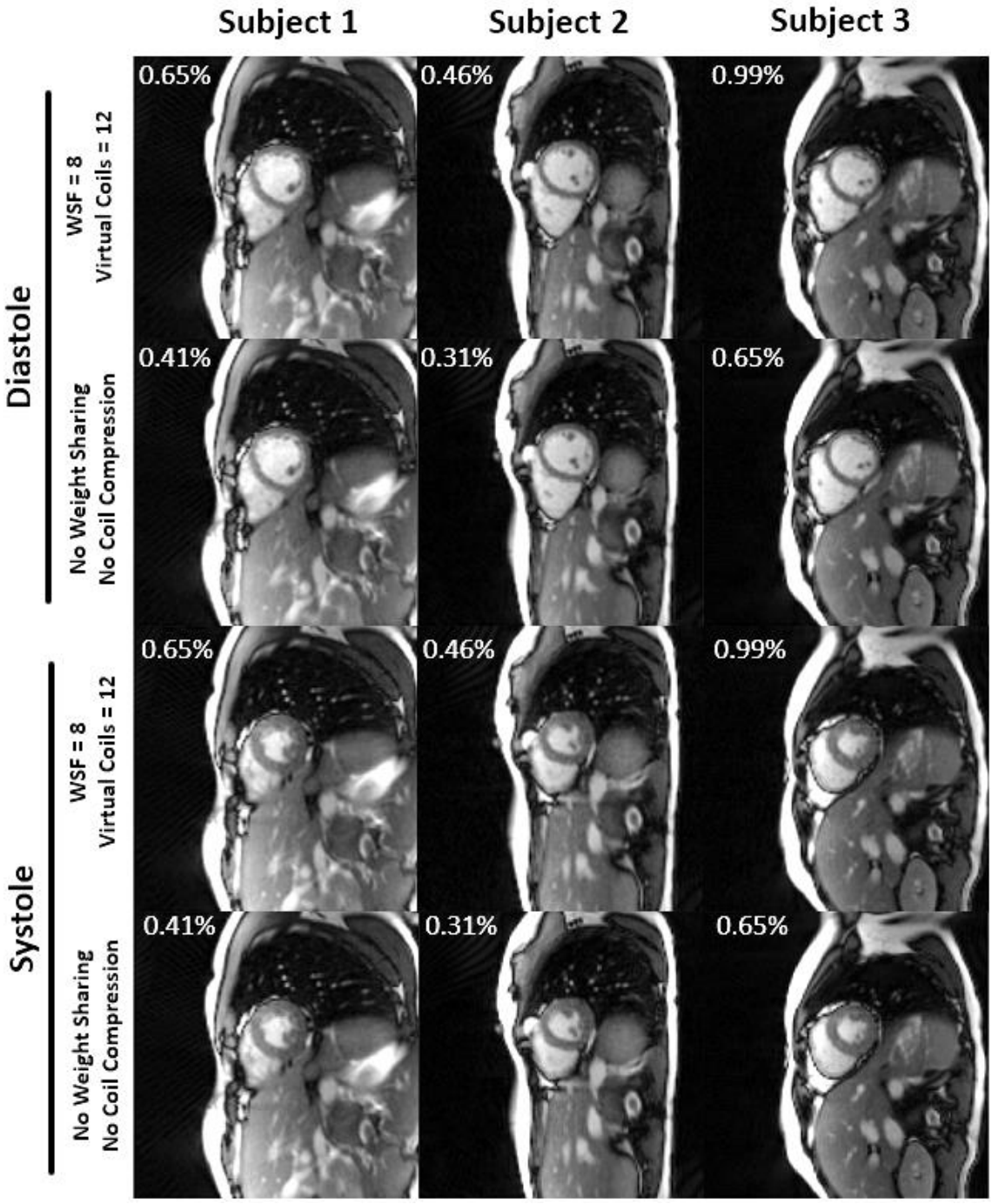

Figure 3-7 Reconstructed images from diastole and systole from three healthy subjects at an acceleration factor of 6. Image RMSE are shown in the top left of each image. Optimized reconstructions performed with 12 virtual coils, 16 calibration frames, and a weight sharing factor of 8 are compared to reconstructions performed with no coil compression, 80 calibration frames, and no weight sharing. In plane resolution is 2.34x2.34mm^2 and temporal resolution is 67ms/frame resulting in a 15 frame/s acquisition. The acquisition time for the calibration data used in the optimized reconstruction was 6.77s, average weight computation time was 3.13s and average weight application time was 4.1s. In contrast, reconstructions with no coil compression or weight sharing have a calibration acquisition time of 34s, average weight computation time of 201s, and average weight application time of 15.1s.

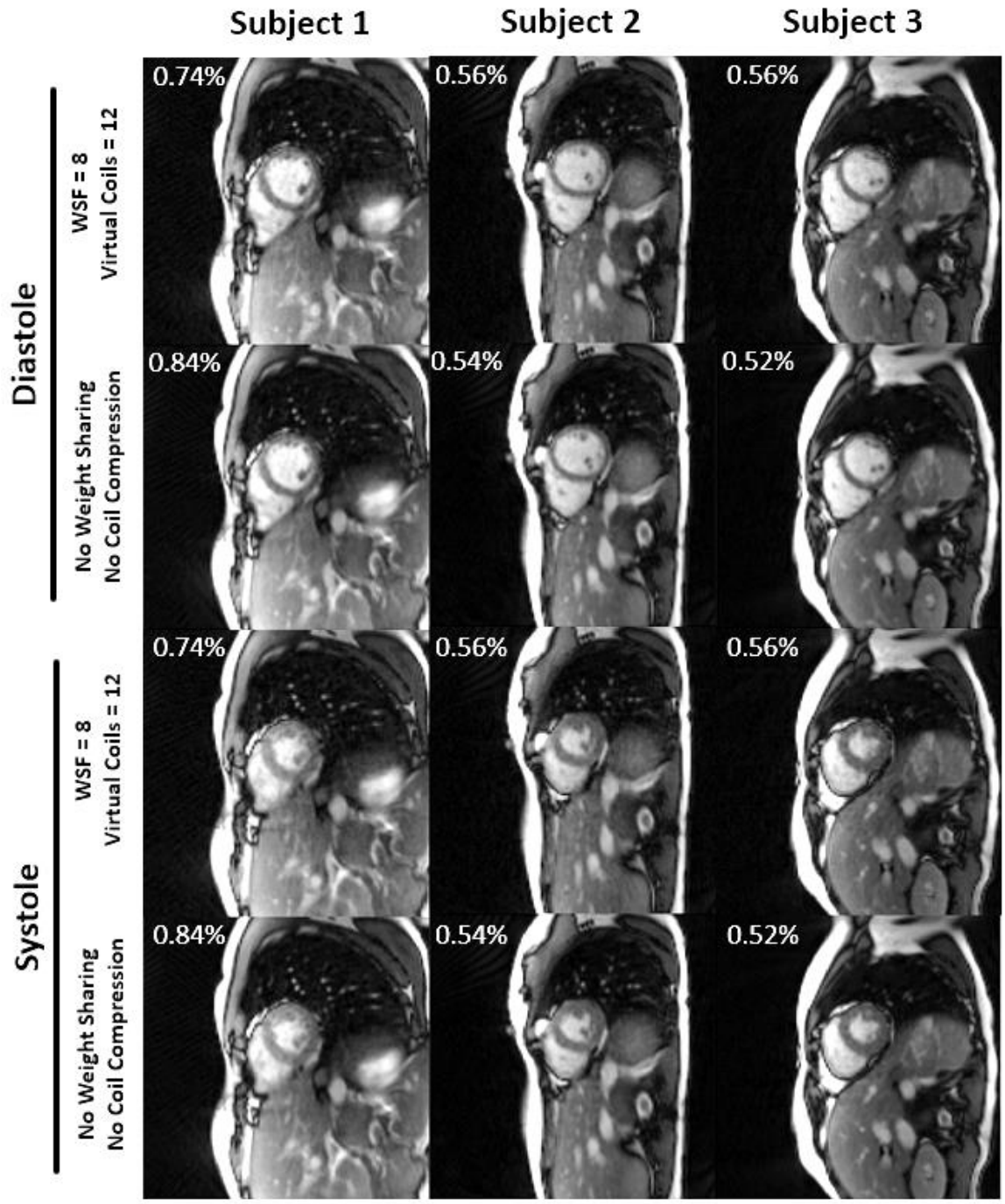

Figure 3-8 Reconstructed images from diastole and systole from three healthy subjects at an acceleration factor of 9. Image RMSE are shown in the top left of each image. Optimized reconstructions performed with 12 virtual coils, 16 calibration frames, and a weight sharing factor of 8 are compared to reconstructions performed with no coil compression, 80 calibration frames, and no weight sharing. In plane resolution is 2.34x2.34mm^2 and temporal resolution is 44ms/frame resulting in a 27.5 frame/s acquisition. The acquisition time for the calibration data used in the optimized reconstruction was 6.77s, average weight computation time was 2.0s and average weight application time was 4.9s. In contrast, reconstructions with no coil compression or weight sharing have a calibration acquisition time of 34s, average weight computation time of 144s, and average weight application time of 18.5s.

3.5: Discussion

In this work, through-time radial GRAPPA, a real-time free-breathing ungated acquisition technique for functional cardiac MRI, is optimized for clinical application by reducing the calibration acquisition time and GRAPPA weight computation time. While prior work has optimized the radial GRAPPA weight application step to enable real-time imaging in an interventional setting[57], such optimizations do not address the calibration acquisition time and GRAPPA weight computation time. However, in functional cardiac MRI, the calibration acquisition and GRAPPA weight computation time are the primary sources of inefficiency: calibration requirements can increase scan time by a factor of 2 or more, and GRAPPA weight computation accounts for nearly 60% of the total reconstruction time. Indeed, the long acquisition time for calibration data has been a limiting factor when implementing through-time radial GRAPPA in a clinical setting. As proposed in Seiberlich et al[61], a through-time radial GRAPPA acquisition for a cardiac imaging application with 75 calibration frames would take 31.5s per slice solely for calibration, and would be inefficient in a clinical setting where 10-15 slices are required for whole heart coverage. In addition to long calibration acquisition times, long GRAPPA weight computation times are impractical for on-line implementation, as more than 20 minutes would be required to calculate the GRAPPA weights for a typical short-axis stack, adversely affecting clinical workflow. To address these issues, an optimized acquisition and reconstruction (12 virtual coils, 16 calibration frames, and weight sharing factor of 8) is suggested, in which images can be generated with image quality comparable to

the gold standard despite requiring only 6.7s of calibration data per slice. Weight sharing in the projection direction could potentially further improve reconstruction performance, but is poorly tolerated and introduces artifacts and blur as shown in Figure 3-5. From these optimizations, GRAPPA weight calculation times were reduced from 201s to 3.1s per slice for an acceleration factor of 6, and 144s to 2.0s per slice for an acceleration factor of 9. With the suggested optimization, the combined calibration acquisition and weight calculation steps may have a reduced impact on clinical workflow, especially as all data collection steps can be performed without ECG gating during free-breathing.

In this work, calibration frames were retrospectively reduced during reconstruction, but in practice, the number of calibration frames must be selected at the time of acquisition. This problem can be addressed by an a priori selection of the number of virtual coils to use in reconstruction at acquisition time. This selection creates a lower bound on the number of calibration frames required to perform GRAPPA, as shown in equation 3-1. For the experimental arrangement at our institution, coil compression to 12 virtual coils results in 90% of the information to be retained with little variability between subjects (see Figure 3-3). Correspondingly, the image reconstructed with weights generated using only 16 calibration frames and 12 virtual coils had an RMSE (1.24%) comparable to an uncompressed reconstruction with 80 calibration frames (1.09%).

It should be noted that coil compression reduces the total signal content used in reconstruction, but despite reduced signal, reconstruction with coil compression either has similar or better RMSE to a reconstruction with no

compression but similar number of calibration frames. The effect of improved image quality with coil compression has been described in other work with Cartesian SENSE[70] and Cartesian GRAPPA[66] and is due to truncation of virtual coils with the lowest signal content which can be dominated by noise. Removal of these virtual coils prevents fitting to noise during GRAPPA weight estimation. The noise reduction performance due to coil compression is expected to depend on a variety of factors including the SNR of the imaging application, the size of the real multichannel array, and the geometry of the array. In addition, truncating too many virtual coils can result in pruning real signal instead of noise. For functional cardiac imaging, the RMSE of through-time radial GRAPPA reconstructions with coil compression was reduced at all compression levels compared to an uncompressed reconstruction for a fixed number of calibration frames, as shown in Figure 3-2, suggesting that the signal from a smaller number of virtual coils contains sufficient structural and contrast information for robust image reconstruction.

In comparison to many other techniques for rapid functional cardiac MRI, such as machine learning based parallel imaging approaches[71,72] or compressed sensing[73], non-Cartesian GRAPPA methods acquire images with sufficient temporal resolution to not require ECG-gating or breath holds. While compressed sensing approaches have the advantage of greatly reducing acquisition time, the non-linear reconstruction is not conducive to parallelization, impeding optimization of reconstruction performance[54,73,74]. Machine learning based approaches have excellent reconstruction speed but have not yet been shown to

be generalizable. Thus, many newer cardiac MR approaches still require breath-holds or ECG-gating which are points of imaging failure in patients with dyspnea or arrhythmia. Non-Cartesian GRAPPA techniques are clinically robust to many pathologies[32] and the presented optimized strategy for through-time radial GRAPPA resolves long-standing issues with clinical implementation without compromising image quality. In addition, coil compression and weight sharing should be applicable to other though-time non-Cartesian GRAPPA implementations.

3.6: Conclusions

Through-time radial GRAPPA enables free-breathing ungated functional cardiac imaging with high temporal resolution. However, the initial formulation of through-time radial GRAPPA requires a time-consuming calibration acquisition and long weight computation times. In this work, these disadvantages are mitigated via coil compression and weight sharing. Coil compression to 12 virtual coils (90% compression factor) results in minimal impact on image quality across all tested acceleration factors. The associated reduction in requisite calibration data to 16 frames enables calibration acquisition time to be reduced from 31.5s to 6.7 seconds per slice and GRAPPA weight calculation time to be reduced by 63%. Weight sharing further reduces GRAPPA weight calculation time with minor impact on image RMSE at a weight sharing factor of eight. Combined application of coil compression and weight sharing does not degrade image quality while retaining calibration and reconstruction benefits of each processing step and reducing GRAPPA weight calculation to <3s across all acceleration factors. This

work demonstrates that coil compression and weight sharing can be used to reduce calibration acquisition time and reconstruction latency of through-time radial GRAPPA for functional cardiac imaging without compromising image quality.

Chapter 4 Integrating Cardiac MRF into the Clinical Workflow using the Gadgetron Framework

In this chapter, a new quantitative imaging technique used in the heart, cardiac Magnetic Resonance Fingerprinting or cMRF, is integrated into a standard clinical interface to enable accessibility to a new imaging technique. Cardiac MRF (cMRF) is an MRF technique that allows the simultaneous acquisition of T1, T2, and M0 maps in the heart. cMRF is unique in that a new MRF dictionary must be simulated after every scan to incorporate subject- and scan-specific variations in heart rate. These simulations are incompatible with current clinical reconstruction software and, thus, must be performed off-site. As a solution, dictionary simulation tools and cMRF reconstruction were implemented in Gadgetron, an open-source modular reconstruction platform that allows complex reconstruction algorithms to interface directly with MRI scanners. The Gadgetron cMRF implementation was found to have no significant bias in relaxation parameter measurements with the prior technique and improved reconstruction performance by 61%. In addition, the Gadgetron cMRF implementation no longer required human intervention for cumbersome data transfer steps between the MR scanner, an off-site reconstruction computer, and the clinical electronic medical record, enabling seamless integration into standard clinical and research workflow. The availability of such a vendor-independent cardiac MRF reconstruction system will allow rapid scientific and clinical evaluation of cMRF at other clinical sites.

4.1: Introduction to Magnetic Resonance Fingerprinting

Magnetic resonance fingerprinting (MRF) is a quantitative imaging method that produces multiple tissue property maps simultaneously. Conventional quantitative imaging measures only one parameter at a time and required a collection of images with different acquisition times to fit a signal model to estimate the parameter of interest, resulting in a relatively time-consuming procedure. In contrast, MRF utilizes a pseudo-random imaging sequence in a highly accelerated imaging framework and matching pixel-wise signal evolutions to pre-computed dictionaries of signal evolutions. Within the dictionary, each set of imaging parameters has a unique "fingerprint" signal evolution in response to the imaging sequence[19]. By modularly adding sequence blocks with different RF pulses and gradients, MRF imaging sequences can be made more sensitive to mapping different tissue properties such as T_1 and T_2 relaxation[19,75,76], volume fraction[77], or saturation transfer[77,78]. In addition, sources of artifact in the imaging system can be compensated by adding artifact sources, such as B0 and B1 inhomogeneity[79–81] and off-resonance[19], into the signal evolution model. As a result, MRF-acquired tissue property maps have been shown to be robust to artifact and reproducible across scanners, healthy volunteers, and patients[80,82–86]. The rapid and accurate acquisition of tissue property maps generated by MRF have garnered significant clinical interest in MRF imaging techniques and applications.

As most MR vendors do not have a commercially available MRF sequence, clinical validation of MRF is done in partnership with MR researchers, and

requires time-consuming transfer of both raw and reconstructed MR data between clinical systems and laboratory workstations. Gadgetron, an open source image reconstruction platform that can interface directly with the MR scanner, has previously been successful at eliminating data transfer steps and delays between imaging and clinical reading for commercially unavailable imaging techniques[87]. Gadgetron reconstructed images are seamlessly returned to the MRI scanner display, enabling non-intrusive integration into the diagnostic workflow (Figure 1). In addition, Gadgetron has in-built algorithms for graphics processing unit (GPU) accelerated image reconstructions which can improve reconstruction performance of computationally intenstive reconstructions to clinically appropriate timescales. GPU accelerated image reconstructions for other imaging techniques such as parallel imaging[88], phase velocity mapping[89], and perfusion imaging[90,91]. Gadgetron MRF has been developed for clinical prostate tissue property mapping, by integrating dictionary matching into Gadgetron with a pre-computed prostate MRF dictionary[92]. In addition, Gadgetron applications are deployable as encapsulated virtual images using Docker, enabling rapid clinical collaboration. As a result, Gadgetron is an excellent platform to deploy future MRF technologies.

4.2: Cardiac Relaxometry and MRF

Quantitative cardiac tissue property mapping has been shown to provide clinically actionable information in acute situations[93] such as early detection of acute myocardial infarction[94,95], reperfusion hemorrhage[96] and monitoring of vasodilator function in acute coronary syndrome and acute myocardial

infarction[97]. Fluid integration of cardiac MRF (cMRF) into clinical workflow can greatly improve acquisition time for these applications. However, cMRF differ from other implementations of MRF in that the image sequence timings depend on heart rate and vary from scan to scan. These timings must be modeled when generating the dictionary to ensure accurate quantification of relaxation parameters. Thus, each cMRF acquisition requires a unique signal dictionary which cannot be precomputed[75]. Dictionary simulation is the most computationally expensive portion of MRF reconstruction workflow, and while MEX-c compilation of existing MATLAB code can improve performance of dictionary simulations to clinically feasible timescales, this method requires additional software and licenses that are not provided with MR scanner installations and are rarely found in clinical practice.

Clinical interest in cMRF provides the impetus for implementation and optimization of dictionary simulation within Gadgetron to deploy cMRF images on clinically appropriate timescales.

4.3: Gadgetron Reconstruction Framework for Online Imaging

A flowchart of the Gadgetron-based cMRF reconstruction pipeline is shown in Figure 1. Each step is described in detail in the following sections.

cMRF Pulse Sequence and Data Acquisition

Data were collected with a previously described 15-heartbeat 2D cMRF sequence comprised of three 5-heartbeat blocks[75]. An inversion preparation pulse is applied every five heartbeats and adiabatic T_2-preparation pulses are applied every third, fourth and fifth heartbeats with echo times of 30ms, 50ms

and 80ms, respectively. Flip angles are varied from 4° to 25° and the TR/TE are held constant at 5.1/1.4ms. Data are sampled along a variable density spiral trajectory that rotates by the golden angle every TR. Fifty TRs are acquired every heartbeat during a diastolic scan window of 255ms, and a total of 750 TRs are collected over the entire scan.

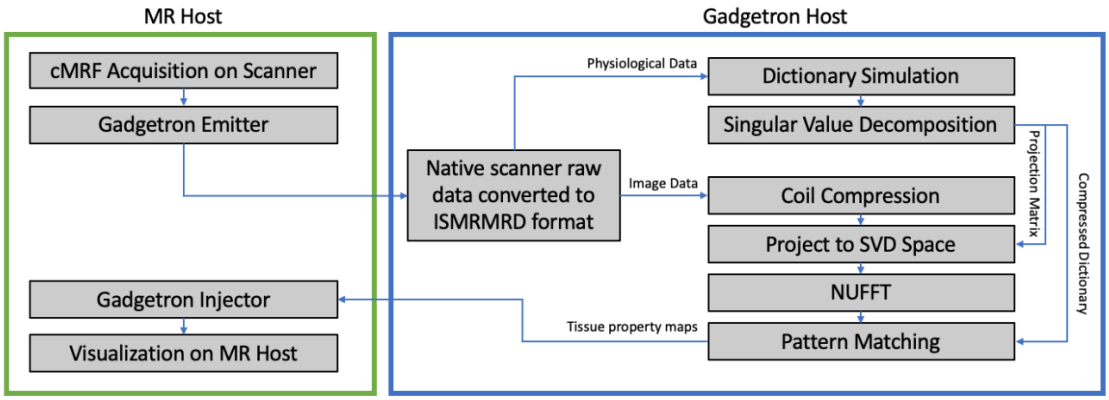

Figure 4-1: Flowchart of Gadgetron cMRF workflow. Prior to implementation of Gadgetron cMRF, tasks shown to be performed on Gadgetron host were previously performed by a research associate who would manually transfer data and run reconstruction in MATLAB environment at off-site laboratory workstation.

As shown in Figure 4-1, the raw cMRF data are transferred from the scanner in native scanner format to the Gadgetron computer, where it is converted into the ISMRM raw data format[98]. Raw data is then parsed and passed on to dictionary simulation and pattern matching modules within Gadgetron for reconstruction.

Dictionary Simulation

cMRF dictionary generation is performed via Bloch simulation with an isochromat of 50 spins. Variable heart rate timings for each individual cMRF scan are integrated into the dictionary simulation using recorded ECG timestamps. cMRF dictionary has an exponential step size in T_1 and T_2 of 5%, with minimum values of 2ms scaling to a maximum T_1 of 6000ms and a maximum T_2 of

1000ms. Dictionary entries where T_2 is greater than T_1 are truncated from the dictionary, resulting in 6473 pairs of T_1 and T_2 values to be simulated. Off-resonance is not simulated in the dictionary because the FISP sequence is relatively insensitive to this parameter. Bloch equation simulations generate a final dictionary of signal evolutions specific for a particular scan made up of 6473 entries with 750 timepoints.

The MATLAB cMRF pipeline was mirrored and optimized in Gadgetron by writing new gadgets to implement tools for optimized Bloch equation simulations and MRF reconstruction processes. Heart rate independent simulation components, such as rotation matrices for the flip angle excitation train, preparation pulses, and spoiler phase dispersion, were pre-computed upon initiating image acquisition to reduce apparent reconstruction overhead.

SVD Compression

As shown in Figure 1, the resulting dictionary is compressed along the time dimension using singular value decomposition (SVD) from 750 timepoints to 47 singular values to reduce memory requirements and accelerate pattern matching. Singular values past 47 collectively contain less than 0.5% of signal required for pattern matching. The right singular matrix from the SVD is stored to project accelerated MRF images onto the same SVD space as the compressed dictionary prior to pattern matching. The low-rank approximation of the dictionary reduces memory requirements and accelerates pattern matching performance[99]. SVD implementation in Gadgetron was performed using the SVD algorithm in the Intel Matrix Kernel Library (MKL).

Image Reconstruction and Pattern Matching

Acquired undersampled image data (30 coils, 750 images) undergoes SVD coil compression along the coil dimension to compress the data to 12 virtual coils. For the same reason as dictionary SVD, 12 coils are selected as singular values past 12 contained less than 0.5% of acquired signal.

Undersampled cMRF images were gridded every TR using the Gadgetron-native GPU-accelerated non-uniform Fast Fourier Transform (NUFFT). The time series of undersampled images are projected onto the SVD space of the compressed dictionary to yield 47 singular images.

Coil sensitivity maps were estimated from the first singular image using the Inati algorithm[100] and the reconstructed images are coil combined via Gadgetron-native adaptive coil combination. As a result, prior to pattern matching, the image space contains 47 singular images. The reconstructed images are then pattern matched to the dictionary using vector dot-product matching.

Projection of acquired data onto dictionary SVD space and vector dot-product matching both require multiplication of large matrices. Gadgetron implementation of these steps were implemented on the GPU using CuBLAS library algorithms to leverage GPU-based parallel processing algorithms.

Offline MATLAB reconstruction

The Gadgetron-based cMRF reconstruction was compared to an offline MATLAB reconstruction, which has been described previously[75]. The MATLAB dictionary simulation and cMRF reconstruction uses CPU-parallelized, compiled Mex code. Gridding is performed using the NUFFT implementation in the

Michigan Image Reconstruction Toolbox (MIRT). Finally, coil sensitivity maps are estimated using adaptive coil combination method. The only differences between Gadgetron and MATLAB-Mex C reconstruction are algorithmic; All dictionary simulation and image reconstruction parameters are unchanged between the two reconstruction.

Bloch equation simulation, data reconstruction and pattern matching for both platforms were performed on the same machine to insure performance comparability (Ubuntu 16.04, 16-core Intel Core i7-7820X, Nvidia GTX1080, 32GB RAM). Performance was assessed by reconstruction time spent in dictionary simulation, SVD compression, NUFFT, pattern matching and overall time.

Phantom Validation

Phantom data are collected on a 1.5T Siemens Aera scanner using the T_2 array of the ISMRM/NIST MRI system phantom[29,82]. EKG signal is simulated at the scanner using vender-provided tools to emulate physiological input into cMRF dictionary simulation. Simulated EKG recapitulated a defined heart rate of 80 beats per minute with no arrhythmia or irregular beats.

4.4: Data Acquisition and Analysis

In Vivo Patient Scans

In vivo data were also acquired on a 1.5T Siemens Aera scanner from 66 patients undergoing MR cardiomyopathy assessment. Patients were chosen as the test group as the variable heart rates observed in pathology would have the greatest impact on tissue property measurement error. Homogenization of B_0

was achieved over phantom vials and heart regions by pre-scan shimming. Mid-cavity pre- and post- contrast MRF datasets were collected in 66 and 64 patients, respectively, in an IRB-approved study.

Analysis of T_1 and T_2 Maps

The accuracy of cMRF T_1 and T_2 maps generated using the Gadgetron pipeline was compared to those generated using MATLAB in the ISMRM/NIST MRI system phantom using average T_1 and T_2 values from circular regions of interest with a 25-pixel diameter (ROIs) drawn in tubes with known relaxometry values. For in vivo assessment, ROIs were drawn by trained radiologists on maps of the mid-chamber short axis view. These ROIs drawn corresponded to AHA heart segments 7-12[101] and were approximately 6 pixels per region, over which relaxometry values were averaged to obtain mean T_1 and T_2 per scan. In vivo measurement differences between Gadgetron and MATLAB reconstructions were assessed by Bland Altman[102,103] analysis between average T_1 and T_2 values over the whole image slice. Scans were partitioned into pre and post contrast comparison groups and measurement biases were determined separately in each group.

4.5: Results

Figure 2 depicts the T_1 and T_2 maps generated from NIST phantom data and demonstrates good visual agreement between Gadgetron and MATLAB-Mex C reconstruction methods. No artifacts are observed in the NIST system phantom images in either the Gadgetron or MATLAB-Mex C reconstruction. In addition, both Gadgetron and MATLAB-Mex C measured T_1 and T_2 values have high

correlation with the reference T_1 and T_2 values in the ISMRM/NIST phantom. Over T_1, Gadgetron and MATLAB both had a R^2 values of 0.998 and over T_2, Gadgetron had an R^2 value of 0.996 and MATLAB had an R^2 value of 0.997. Bland-Altman analysis indicated that the maps generated with Gadgetron had no statistically significant bias in T_1 or T_2 measurement in comparison to the maps generated in MATLAB. The maximum differences between measurements from Gadgetron and MATLAB were 0.19% in T_1 and 0.7% in T_2.

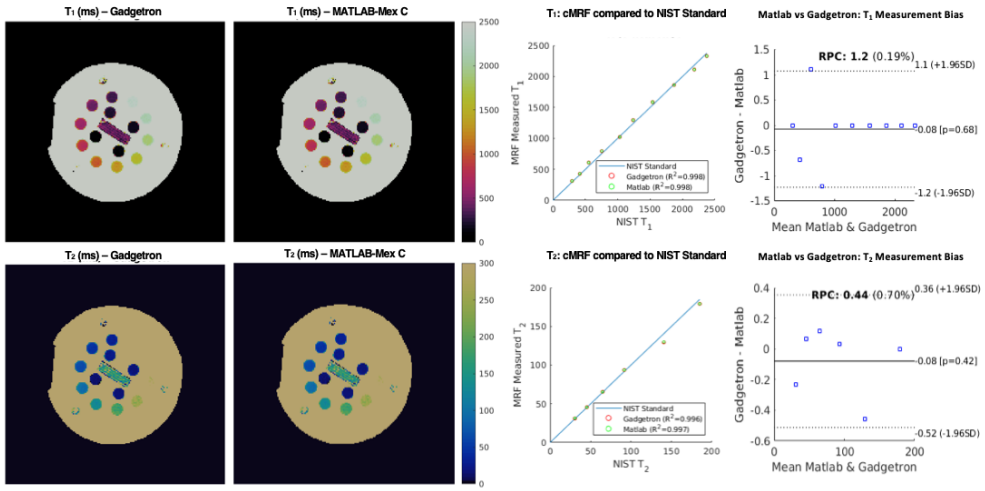

Figure 4-2: T_1 and T_2 maps of ISMRM/NIST phantom calculated using Gadgetron (left) and MATLAB-Mex C reconstruction pipelines. The maps show good visual agreement. ROIs were drawn in each vial and average T_1 and T_2 values were computed. Scatter plots between cMRF measurements made with Gadgetron and MATLAB-Mex C and T_1 and T_2 values provided by NIST show strong correlation with Gadgetron T_1 R^2=0.998, Matlab T_1 R^2=0.998, Gadgetron T_2 R^2=0.996 and Matlab T_2 R^2=0.997. Bland Altman plots demonstrate strong agreement with statistically insignificant bias in T_1 and T_2 with a narrow reproducibility coefficient (RPC), namely ±1.2ms in T_1 and ±0.44ms in T_2. Maximum error in T_1 is 0.19% and maximum error in T_2 is 0.7% which are well within the 5% dictionary step size.

Representative T_1 and T_2 maps are shown in Figure 4-3 and Figure 4-4 and demonstrate good overall visual agreement in T_1 and T_2 values in non-lung tissue regions; however, large deviations up to 18% between the calculated values occur in the lung region, where there is significantly reduced SNR.

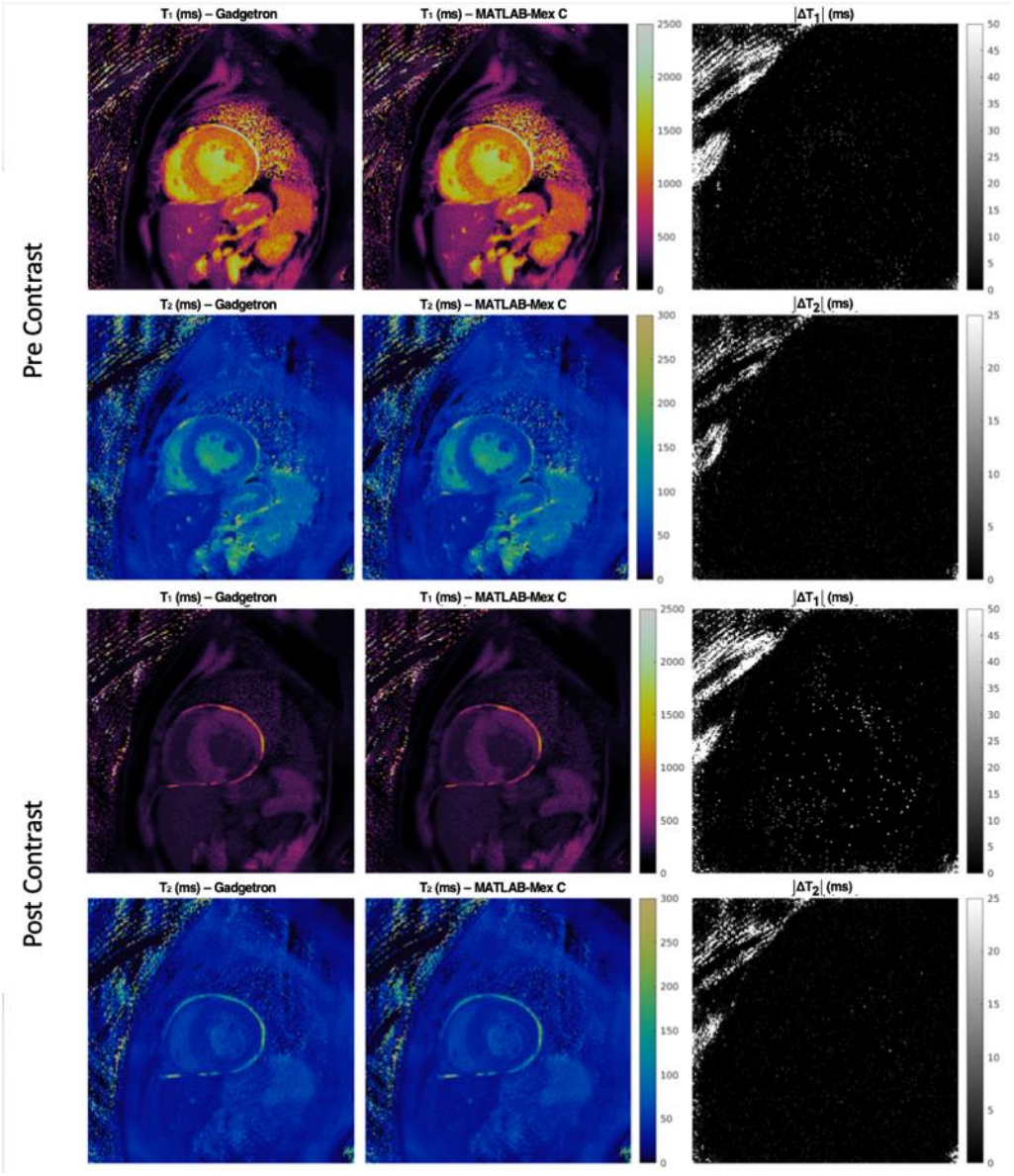

Figure 4-3: Representative pre- and post-contrast T_1 and T_2 maps collected from a representative patient with prior myocardial infarction. Absolute difference maps are shown on the right most column. A transmural scar of the inferolateral wall due to prior infarction is shown with hypertensive changes in wall thickness. Maps show excellent agreement in myocardial and abdominal regions. Differences arise in areas of low signal, specifically the lung and outside the body. These differences are visibly indiscernible and occur in regions outside of clinical interest.

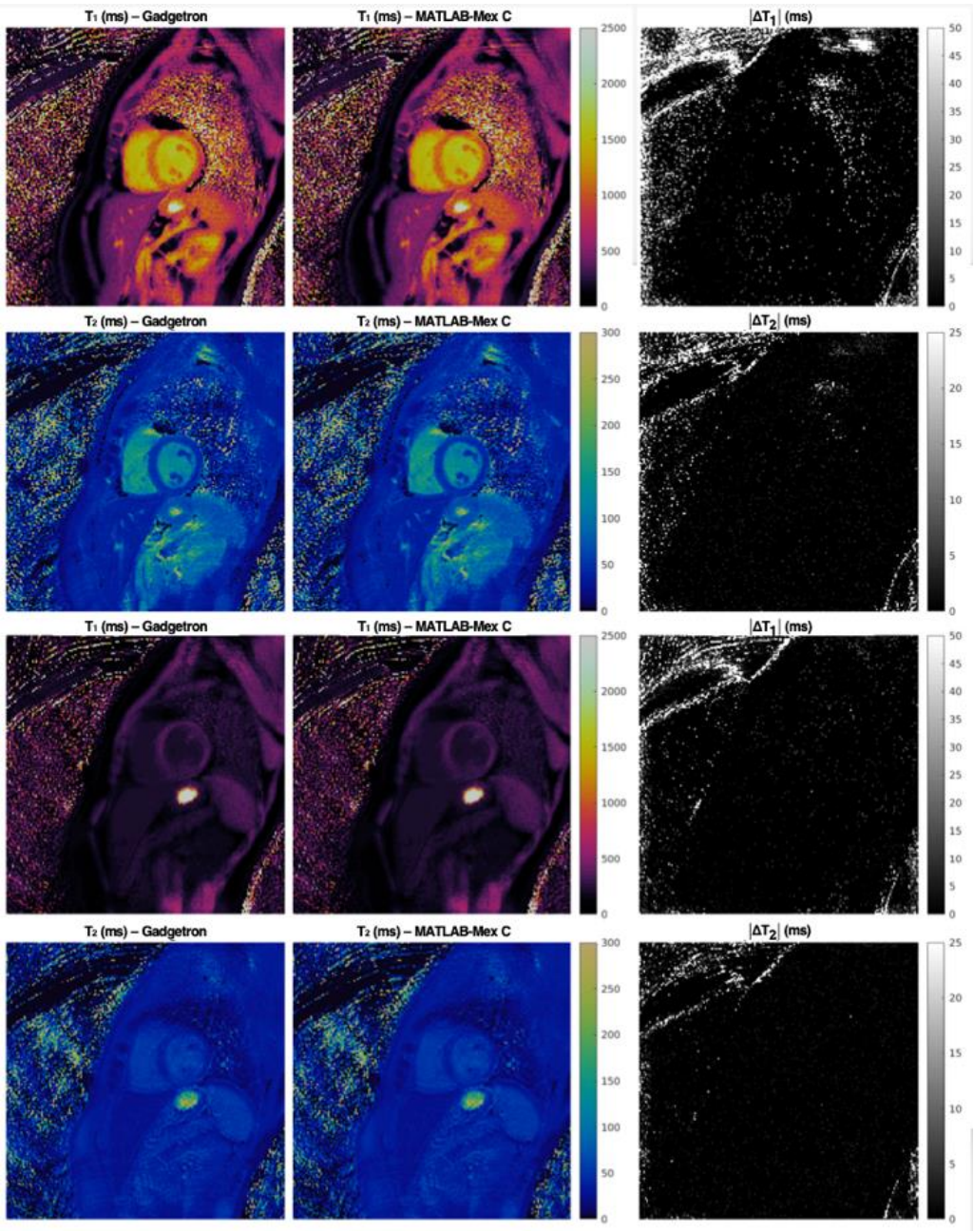

Figure 4-4: Representative diastolic pre- and post-contrast T_1 and T_2 maps collected from a representative patient dilated cardiomyopathy. Absolute difference maps are shown on the right most column. Maps show excellent agreement in myocardial and abdominal regions. Differences arise in areas of low signal, specifically the lung and outside the body. These differences are visibly indiscernible and occur in regions outside of clinical interest.

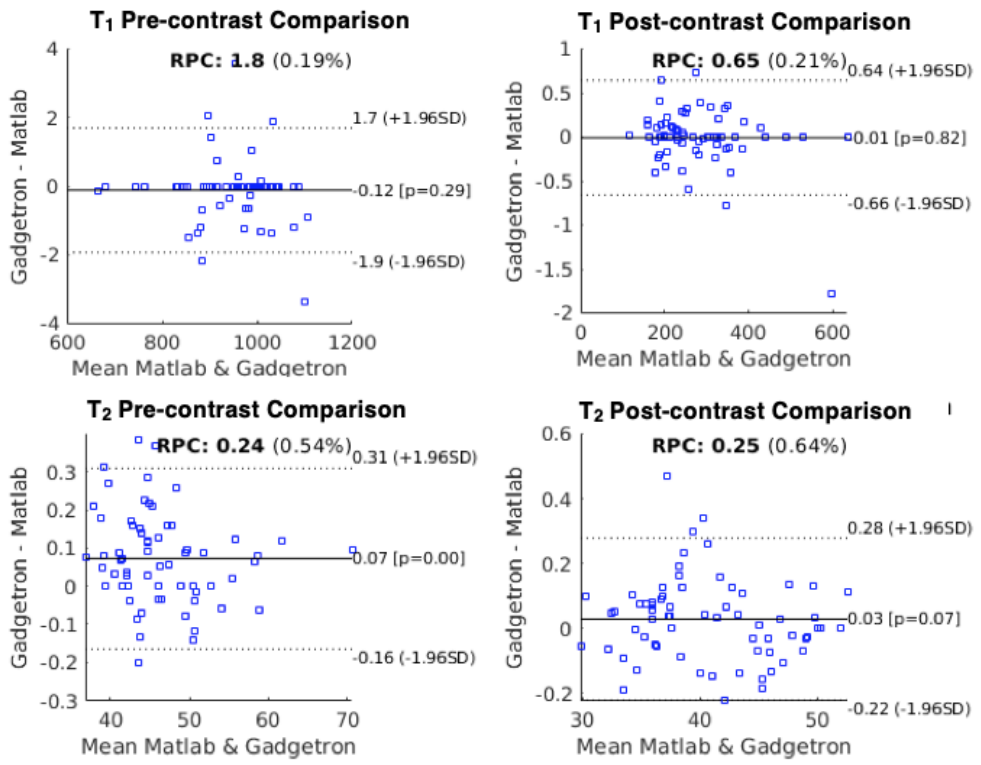

Figure 4-5: Bland Altman plots for pre- and post-contrast average T_1 and T_2 values in radiologist-drawn cardiac ROIs are shown. N=66 for pre-contrast patients and N=64 for post-contrast patients. Pre- and post-contrast T_1 and post-contrast T_2 times show no statistically significant bias and narrow limits of agreement as demonstrated by low RPC. Pre-contrast T_2 measurements show a statistically significant but clinically insignificant different of 0.07ms. The maximum error in pre-contrast T_1 is 0.19% and post-contrast T_1 is 0.21%. The maximum error in pre-contrast T_2 is 0.54% and post-contrast T_2 is 0.64%. All maximum error values are smaller than the 5% step size dictionary resolution.

Figure 4-5 illustrates that Bland-Altman analysis of measured relaxometry values in radiologist-drawn cardiac segment ROIs shows no statistically significant bias between Gadgetron or Matlab-Mex C implementations in both pre- and post-contrast T_1 maps and post-contrast T_2 and a statistically significant in pre-contrast T_2 of 0.07ms ($p < 0.05$) representing a maximum bias of 0.18%. Reproducibility coefficients (RPC) are all less than 1.8s for T_1 measurements and less than 0.25s for T_2 measurements indicating narrow limits of agreements. Maximum measured error is 1.4% and falls well within the predetermined dictionary resolution (<5%).

Benchmark MATLAB-Mex C reconstruction was performed on the same computer configuration as the Gadgetron reconstructions (Ubuntu 16.04, 16-core Intel Core i7-7820X, Nvidia GTX1080, 32GB RAM) and took 62.46s to perform on a stand-alone PC, with dictionary simulation and NUFFT as the largest reconstruction bottlenecks. As shown in Table 1, Gadgetron optimizations achieved 64% overall reconstruction performance improvement over MATLAB. Optimizations in dictionary simulation and the GPU-accelerated NUFFT algorithm improved bottleneck performance and were the major contributors to reducing reconstruction time with 61% improvement in dictionary simulation time and 88% improvement in NUFFT time. SVD compression and pattern matching had minor contributions to reconstruction performance, and GPU optimization of these reconstruction steps slightly reduced the overall reconstruction performance. Gadgetron provided additional performance gains by eliminating the data transfer requirements between scanner and computation system which were not quantified but are significant and cumbersome.

Reconstruction Step	MATLAB Performance	Gadgetron Performance
Dictionary Simulation (s)	41.1	15.9
SVD (s)	0.3	2.2
NUFFT (s)	19.3	2.2
Pattern Matching (s)	1.8	2.2
Total Time (s)	62.5	22.5

Table 4-1: Dictionary simulation and reconstruction performance in MATLAB-MEX C and Gadgetron. Gadgetron shows a 64% overall reconstruction improvement with most improvement gains in the computationally intensive dictionary simulation and NUFFT steps. GPU acceleration of SVD compression and pattern matching had considerable memory overhead which eliminated gains in processing speed, but did not contribute significantly to reconstruction time.

4.6: Discussion

This study demonstrated that despite algorithmic differences between cMRF tissue property generation implementations in Gadgetron and MATLAB, no statistically significant differences in myocardial relaxometry values are found. Both reconstruction pipelines recapitulated literature T_1 and T_2 values as supported by the NIST phantom maps with no significant measurement differences between the two reconstruction platforms. In addition, both platforms have good agreement with previously measured NIST phantom T_1 and T_2 in the physiological range.

In vivo data, encapsulated in Figure 4, demonstrates that Gadgetron and MATLAB cMRF reconstructions had narrow limits of agreement in clinically significant regions of interest in the heart. The largest measured reproducibility coefficient was 1.8ms for T_1 measurement and 0.25ms for T_2 measurement. Because the finest resolution in the dictionary are 2ms for T_1 and T_2 respectively, these differences are comparable to noise-induced variance and are not large enough to affect clinical decision making. Differences in myocardial relaxometry values are either not statistically significant (pre-contrast T_1 and T_2, post-contrast T_2) or quantitatively negligible (post-contrast T_1, bias of 0.07ms) compared to the dictionary resolution.

There are specific steps in the cMRF reconstruction pipeline that differ algorithmically between the Gadgetron and MATLAB-Mex C implementation: low-rank approximation from SVD, NUFFT, and coil combination. Debugging of individual pipeline outputs found that the SVD algorithms used on the two

platforms did have mathematical differences of up to .12% in the calculation of singular values but did not lead to any significant differences in the final reconstructed maps when compared in isolation. Differences in the NUFFT algorithms between Gadgetron and MATLAB cause a different distribution of aliasing artifacts in the underlying undersampled cMRF data, however, these differences also did not propagate further down the reconstruction pipeline and did not result in significant differences in the reconstructed maps. Differences in adaptive coil map estimation and combination algorithms did result in significant differences in relaxometry values in the lungs as well as the appearance of non-Cartesian aliasing artifacts outside the imaging region but did not lead to differences in myocardial values. Pattern matching in the lung region, which has low SNR, is significantly impacted by noise, and coil combination algorithms propagate this noise error in different ways. However, the lung region is not of clinical interest in myocardial mapping and is not considered to be a drawback to the improved afforded by the Gadgetron implementation. However, these algorithmic differences should be shown careful consideration when porting MRF reconstruction pipelines for other body regions, where different coil geometries may considerably enhance the differences due to coil combination algorithms. A potential solution is to utilize a sum-of-squares coil combination step, though this solution may not be suitable for applications that require the preservation of image phase.

The in vivo dataset utilized contained patients with a wide variety of pathological conditions. Patients with dilated cardiomyopathy who have thinner

myocardium, and thus fewer pixels per ROI, have considerably higher variance in measured relaxometry values. The increased variance in average T_1 and T_2 measurements may have contributed to the small bias seen in the post-contrast T_1 maps. However, as stated before, these differences amount to a quantitatively negligible bias of .07ms compared to the dictionary spacing of the physiological T_1 range. In the physiological T_1 range, a 5% dictionary resolution translates to between 40ms to 60ms dictionary spacing. Despite all sources of variability and algorithmic differences, the T_1 and T_2 values calculated using the Gadgetron and MATLAB implementations largely agree and all limits of agreement in both pre and post contrast T_1 and T_2 fall well within the dictionary resolution (<5%).

In terms of computational performance, single-slice cMRF reconstructions as performed in this report, had poor scaling in GPU-accelerated SVD compression and pattern matching due to data transfer overhead that contributed to worse reconstruction performance. SVD performance would be improved with larger dictionary sizes to take advantage of parallel processing available on the GPU. In addition, GPU acceleration of pattern matching is unlikely to lead to any performance improvement in the context of SVD compression, as matrix sizes are too small to enable parallel processing power to compensate for additional data transfer overhead. However, the GPU acceleration pattern matching has potential utility for future applications that may not want to utilize a low-rank dictionary approximation or use particularly large dictionaries such as MRF with proton exchange[77,78]. All GPU accelerated reconstruction steps will scale considerably better with acquisitions that will lead to increase data throughput

such as simultaneous multi-slice or 3D imaging sets which are future directions for cMRF development. These larger datasets will enable better utilization of GPU accelerated reconstruction components, as data transfer overhead will be overshadowed by performance gains at large matrix sizes. In addition, MRF applications that require larger dictionaries, such as when modeling off resonance or B_1 inhomogeneity, will also benefit from the GPU-accelerated tools developed in this work. These advantages can be leveraged to enable cMRF to run on older scanner hardware which may require additional modeling to account for scanner imperfections. Overall, performance improvements in Gadgetron over MATLAB are considerable but modest in the context of one-hour clinical scanning sessions.

The significant value provided by Gadgetron implementation come from scanner integration, which enables online cMRF reconstruction that eliminates the need for data transfer from scanner hardware to research computation systems. After integration, Gadgetron reconstructed T_1 and T_2 maps are easily uploaded by radiology technicians with all other cardiac imaging done during a clinical imaging procedure to hospital imaging databases to be read by radiologists, allowing cMRF to fit within the existing clinical workflow. By enabling faster access to clinically actionable tissue property maps, the utility of cMRF can be expanded to more acute situations[93]. As an open source software, a Gadgetron cMRF dictionary simulation and reconstruction package is now available upon request as a portable Docker[104] virtual machine image.

4.7: Conclusion

The exploration of cMRF for clinical applications has been impeded by the need for scan-specific cMRF dictionaries and reconstruction tools that are not available on commercial scanner software. Gadgetron implementation of the cMRF reconstruction pipeline not only recapitulates the accuracy observed with the currently employed MATLAB-Mex C reconstruction tools, but also improves reconstruction performance and eliminates time intensive and error-prone data transfers. The work presented herein will allow rapid implementation of cMRF in the clinical setting and enable further research in cMRF applications.

Chapter 5 Balancing Acquisition Time and Image Quality for Fast T_2-weighted Imaging

This chapter will discuss the acceleration of T_2-weighted imaging, which is essential for many clinical applications. Clinically, T_2-weighted imaging is performed with slow Cartesian TSE sequences. While it is possible to accelerate TSE sequences by altering sequence parameters, such as echo train length, partial Fourier acquisition, or sampling trajectory, these changes may affect image contrast and introduce artifacts leading to a difficult-to-predict reduction of image quality. Using digital phantoms that replicate specific imaging conditions, namely prostate biopsy, simulations were performed to explore the balance between acquisition time and image quality for accelerated TSE-based T_2-weighted imaging.

5.1: Introduction

T_2-weighted imaging is essential in clinical practice for several applications and is commonly performed using Cartesian TSE sequences. These sequences are comprised of an excitation pulse followed by a train of 180° pulses to refocus the signal that is dephased due to field inhomogeneities (T_2*). To avoid weighting due to T_1 relaxation, long repetition times (T_R), typically between 4000-6000ms, are used to recover longitudinal magnetization between acquisition shots. These constraints result in long acquisition times for many applications, specifically, those that require a large field-of-view (FOV = 400mm2) and high resolution (1mm x 1mm x 3mm), such as prostate imaging. Parallel imaging with GRAPPA has enabled acquisition time reduction, but acceleration factors are limited to

R=3, resulting in acquisition times of 40-60s. For interventional applications, including in-gantry prostate biopsy, which relies heavily on T_2-weighted images, such long acquisition times result in a considerable latency in visual feedback. Such long acquisition times can make performing these procedures cumbersome and technically challenging. Thus, faster T_2-weighted imaging would benefit more efficient diagnostic imaging and improved MR-guided procedures.

There are several approaches to reducing the acquisition time of T_2-weighted TSE images. The T_R can be shortened to reduce the acquisition time directly. However, this results in increased T_1-weighting, altering image contrast, and a reduction in the recovery of longitudinal magnetization and, thus, SNR. Increasing the echo train length (the number of phase encoding lines collected for each T_R) reduces the number of repetitions required for the acquisition; single-shot TSE sequences such as HASTE are extreme examples of this approach. However, a longer echo train can result in a loss of resolution due to blurring from shorter T_2 species which can obscure small anatomical structures and lesions. Another regularly used approach is to reduce the number of acquired lines using undersampling and a dedicated image reconstruction strategy such as parallel imaging. However, acceleration factors greater than 3 are prone to reduced SNR and residual aliasing artifacts, limiting its efficacy. Another method is to alter the sampling trajectory to increase the k-space that can be covered during the same echo train duration. Non-Cartesian spiral sampling trajectories can potentially increase k-space sampling efficiency in TSE but have been shown to have different image artifacts and contrast

characteristics[105,106] resulting from T_2-decay induced signal modulation due to repeated sampling of the k-space center. In addition, spiral trajectories typically have longer readouts that are prone to off-resonance artifacts[107] that manifest differently from Cartesian TSE. Thus, the impact of TSE imaging parameters and the sources of image quality degradation with faster imaging is expected to differ significantly for spiral and Cartesian TSE. However, non-Cartesian trajectories in conjunction with advanced reconstruction techniques such as parallel imaging or compressed sensing are helpful for rapid imaging in cardiac imaging[57,108,109], abdominal imaging[110,111], magnetic resonance angiography[112], and arterial spin labeling[113,114] and can potentially be applied to other applications. A solution to faster T_2-weighted TSE is likely a combination of these strategies; given the large number of parameters that can be adjusted and the differing needs of different applications, the optimal sequence may depend on the goal of imaging as well as the hardware available.

In-bore MR-guided prostate biopsy is one application that relies on T_2-weighted guidance imaging for accurate lesion targeting. Due to complex and variable pelvic anatomy and the high variability of lesion contrast, size, and location, in-bore MR-guided prostate biopsy is a technically challenging procedure that requires considerable operator expertise[115,116]. Long Cartesian TSE acquisitions are commonly used as image guidance, though gradient echo sequences[117,118] and single-shot HASTE[119] have also been used to reduce visual feedback latency. However, GRE sequences have poor image contrast and are sensitive to the variety of off-resonance sources in the pelvis, leading to signal

dropout and distortion. Single-shot HASTE has T_2-weighted contrast but can also suffer from blurring, preventing accurate visualization of small or low-contrast lesions which could lead to inaccurate targeting. To provide adequate image quality for image guidance during a prostate biopsy, a fast T_2-weighted sequence must retain the sufficient resolution and contrast to visualize and target lesions while adding minimal additional artifacts. Thus, there is a need to identify a method for rapidly acquiring T_2-weighted images for specific applications, such as in-bore prostate biopsies, and to characterize the trade-off between faster acquisition time and image quality.

In this work, a simulation approach is taken to explore the parameter space of fast T_2-weighted TSE sequences to characterize trade-offs between image quality and acquisition time for use in prostate biopsy. Digital phantoms were designed to replicate specific imaging conditions during a prostate biopsy: variable lesion size, lesion T_2, and off-resonance sources. Fast T_2-weighted sequences with a range of echo train lengths, echo spacings, acceleration factors, and acquisition trajectories were simulated. Image quality metrics of contrast, image sharpness, and artifact power were measured from these phantom images and the results compared to determine if the acquisition time for the T_2-weighted images used in prostate biopsy could be shortened without significantly impacting image quality.

5.2: Methods

Simulation

The images produced by various TSE sequences were simulated using a discrete-event model, as described in Kwan et al[120] and Petersson et al[121]. For the specific application of prostate biopsy, the effects of T1, T2, T2*, and off-resonance were simulated; other tissue characteristics were neglected. The spin density of the image object $\rho(x,y)$ is partitioned to N groups of spin densities $\rho_n(x,y)$, where the nth spin density matrix corresponds to all voxels with the nth unique set of tissue properties $<T_1,T_2,\Delta B_0,\ldots>_n$. The Fourier representation of each such spin density partition is represented in k-space as $P_n\big(k_x(t),k_y(t)\big)$ where the position in k-space is temporally dependent on spatial encoding events. For each spin density partition, tissue properties of each non-zero voxel in $\rho_n(x,y)$ and the resulting spin evolutions of any voxel in that group are identical. Thus, the acquired time-domain signal of the nth partition, S_n, can be described as

$$S_n\big(k_x(t),k_y(t),t\big) = M_{\perp,\mathrm{n}}(t)\cdot P_n\left(k_x(t),k_y(t)\right) \tag{5-1}$$

where $M_{\perp,\mathrm{n}}(t)$ represents the complex transverse magnetization at time t. This expression can be written as:

$$S_n(t) = M_{\perp,n}(t)\cdot P_n(t) \tag{5-2}$$

The time domain signal S(t), acquired from the whole object, is then the sum of the signals from each spin group.

$$\mathrm{S(t)} = \sum_{\mathrm{i=0}}^{\mathrm{N}} \mathrm{M}_{\perp,i}(\mathrm{t})\cdot \mathrm{P_i(t)} \tag{5-3}$$

The simulated image is obtained by applying a gridding operator $\mathcal{G}$ to the simulated signal and applying the inverse Fourier transform as follows:

$$\mathrm{Im}(\mathrm{x},\mathrm{y}) = \mathcal{F}^{-1}\{\,\mathcal{G}\{\mathrm{S}(\mathrm{t})\}\,\} \tag{5-4}$$

For this simulation, the spin dynamics of relaxation and off-resonance during the TSE sequences are modeled using a Bloch matrix formalism[122,123]. $\mathrm{M}_{\perp,i}(\mathrm{t})$ is generated from a Bloch simulation of a voxel with relaxation properties $<T_1,T_2,\Delta B_0,\ldots>_i$ corresponding to the i^{th} partitioned spin density. To accurately model spin rephasing in forming the spin-echo, T_2* is modeled using an ensemble of spin isochromats with a Lorentzian frequency spectrum to model intravoxel field inhomogeneities and reproduce T_2^* effects. The frequency spectrum is parameterized as follows[24,120]:

$$M_0(\omega) = \frac{2T_2'}{1 + [2\pi T_2'\omega]^2} \tag{5-5}$$

where

$$\frac{1}{T_2^*} = \frac{1}{T_2} + \frac{1}{T_2'} \tag{5-6}$$

Off-resonance is modeled in the Bloch equation simulator by multiplying the simulated transverse magnetization by a complex phasor:

$$M_{\perp,\mathrm{n}}(t) = M_{\perp,\mathrm{n}}(t) \cdot e^{i2\pi\Delta\omega(t-kt_{ESP})} \tag{5-7}$$

where k is the current echo in the echo train. A diagrammatic representation of the simulation is shown in Figure 5-1.

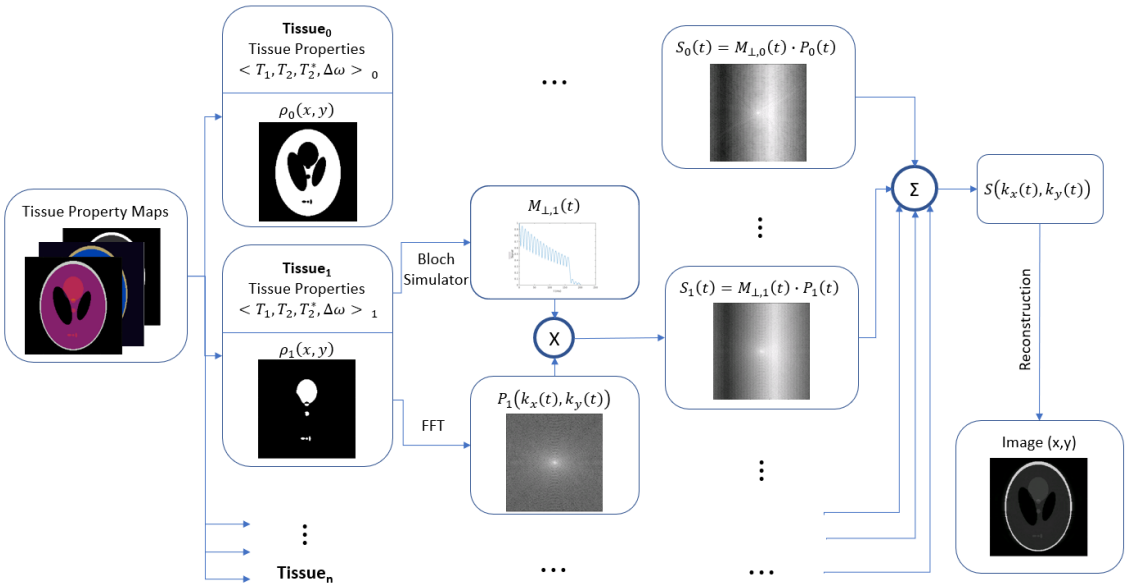

Figure 5-1: Functional block diagram describing the simulation process, where the tissue property maps are input to yield an image. A Cartesian sampling scheme is shown here, but the simulation process for a spiral sampling scheme is identical with a NUFFT instead of an FFT, and with a different reconstruction process to for the double encoded data.

Digital Phantoms

A set of digital phantoms was designed to mimic conditions of in-bore MR guided prostate biopsy that include T1, T2, T2*, and off-resonance effects, as shown in Figure 5-2. Bloch equation simulations as described above were used to generate images from these digital phantoms.

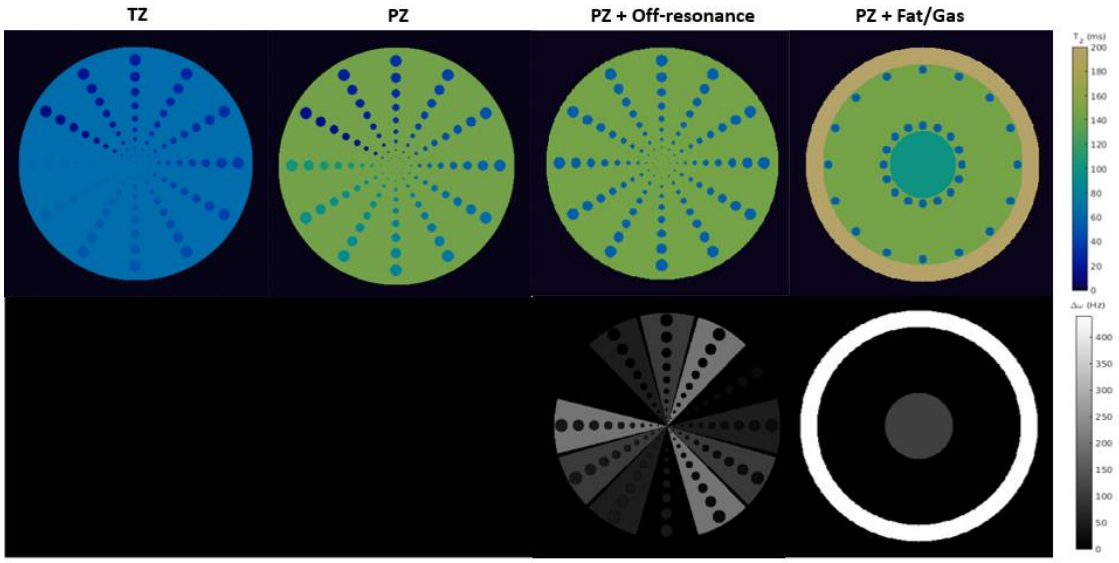

Figure 5-2: Set of phantoms used in simulation, with the top row showing T2 relaxation maps and the bottom row showing off-resonance maps. (Left and Middle Left) In the "TZ" and "PZ" phantoms, the T_2 of lesions are varied in each radial projection. The T_2 values span the range of average T_2 values for either transition zone or peripheral zone to $\pm 3\sigma$. Background has relaxation properties that mimic healthy tissue. (Middle Right) An off-resonance phantom was designed with constant relaxation properties in each area corresponding to the average relaxation properties of a peripheral zone lesion. The off-resonance offset of lesions in each radial projection were varied (0Hz,20Hz,40Hz) in addition to the off-resonance of the healthy tissue background (0Hz, 50Hz, 100Hz, 200Hz) (Right) A phantom designed to mimic in vivo conditions, including off-resonance from adjacent non-prostate tissue. The outer ring is set to the off-resonance frequency and apparent relaxation properties of fat at 3T (T1 = 400, T2 = 200, 440Hz) and the inner circle is set to an off-resonance frequency and relaxation properties to mimic rectal wall (T1 = 2000, T2 = 100, 110Hz). See ***Error! Reference source not found.*** *for relaxation parameters for individual lesions and the healthy background.*

The first two digital phantoms imitate lesions found in the transition zone and peripheral zone of the prostate. These phantoms are referred to as the "TZ phantom" and the "PZ phantom," respectively. Lesions are mimicked as circles embedded in a matrix with relaxation properties reflecting healthy prostatic tissue. Lesion T_2 is varied over three standard deviations of previously measured T_2 values and lesion size is varied from 1mm to 10mm in radius[124,125]. Variable T_2 values are used to compare the effects of T_2-decay induced signal modulation. The third phantom mimics imaging in the presence of mild to moderate off-resonance sources such as main field inhomogeneity. Off-resonance values are assigned to the lesions and the surrounding healthy tissue. The resonance

frequency offsets used spanned those typically found in the peripheral zone (0-200Hz) either due to main field inhomogeneity or susceptibility from rectal gas[126]. In this phantom, the lesions range in size from 1mm to 10mm and with T_1 = 1650ms and T_2 = 56ms, mimicking relaxation properties of cancerous peripheral zone lesions. This phantom is referred to as the "PZ + off-resonance phantom". The fourth phantom mimics large sources of off-resonance due to rectal gas and fat, which primarily impacts the peripheral zone and overall image quality. Lesions were placed in a matrix mimicking the peripheral zone, with a central region of rectal wall ($\Delta\omega = 110Hz$) and surrounded by an outer region of fat ($\Delta\omega = 440Hz$). This phantom is referred to as the "PZ + fat/gas phantom".

	TZ Phantom		PZ Phantom	
Sector Region	**Lesion**	**Background**	**Lesion**	**Background**
Sector 1	[1450ms, 14ms]	[1800ms, 65ms]	[1800ms, 16ms]	[2240ms, 146ms]
Sector 2	[1450ms, 18.4ms]		[1800ms, 24ms]	
Sector 3	[1450ms, 22.8ms]		[1800ms, 32ms]	
Sector 4	[1450ms, 27.2ms]		[1800ms, 40ms]	
Sector 5	[1450ms, 31.6ms]		[1800ms, 48ms]	
Sector 6	[1450ms, 36ms]'		[1800ms, 56ms]'	
Sector 7	[1450ms, 40.4ms]		[1800ms, 64ms]	
Sector 8	[1450ms, 44.8ms]		[1800ms, 72ms]	
Sector 9	[1450ms, 49.2ms]		[1800ms, 80ms]	
Sector 10	[1450ms, 53.6ms]		[1800ms, 88ms]	
Sector 11	[1450ms, 58ms]		[1800ms, 96ms]	
Sector 12	[1450ms, 62.4ms]		[1800ms, 104ms]	

Table 5-1: Relaxation properties of prostate lesions modeled in digital phantoms shown as binary pairs of [T1, T2]. The properties of sector 6, which corresponds to the 3 o'clock position on the digital phantoms, are the average relaxation properties of prostatic lesions in the transition and peripheral zones. Note, as mentioned previously, the T_2 is set to $T_2/2$.*

The values for T_1, T_2, and off resonance assigned to each of the spaces for the four digital phantoms are enumerated in

	TZ Phantom		PZ Phantom	
Sector Region	**Lesion**	**Background**	**Lesion**	**Background**
Sector 1	[1450ms, 14ms]	[1800ms, 65ms]	[1800ms, 16ms]	[2240ms, 148ms]
Sector 2	[1450ms, 18.4ms]		[1800ms, 24ms]	
Sector 3	[1450ms, 22.8ms]		[1800ms, 32ms]	
Sector 4	[1450ms, 27.2ms]		[1800ms, 40ms]	
Sector 5	[1450ms, 31.6ms]		[1800ms, 48ms]	
Sector 6	[1450ms, 36ms]¹		[1800ms, 56ms]¹	
Sector 7	[1450ms, 40.4ms]		[1800ms, 64ms]	
Sector 8	[1450ms, 44.8ms]		[1800ms, 72ms]	
Sector 9	[1450ms, 49.2ms]		[1800ms, 80ms]	
Sector 10	[1450ms, 53.6ms]		[1800ms, 88ms]	
Sector 11	[1450ms, 58ms]		[1800ms, 96ms]	
Sector 12	[1450ms, 62.4ms]		[1800ms, 104ms]	

Table 5-1. Literature describing T_2^* properties of the prostate[127–129] is sparse, so T_2^* was approximated to be equal to $\frac{T_2}{2}$ based on published values of quantitative T_2[130–135] and T_2^*[128] measurements and to enforce $T_2^* < T_2$ for all tissues.

Simulation Parameters

For both Cartesian TSE and spiral TSE, the following sequence parameters were held constant: T_R = 4000ms, FOV = 400mm, Resolution = 1.04mm x 1.04mm (matrix size 384x384). The excitation flip angle was 90 degrees, and the refocusing flip angle was 180 degrees. The T_E used for Cartesian TSE was 100ms. Spiral TSE has a variable effective T_E dependent on both echo train length (ETL) and echo spacing (ESP) and thus this parameter was not held constant. ETL was varied between 8 and 64 in steps of 8, ESP was varied from 5ms to 20ms in steps of 3ms, and the acceleration factor (R) is varied between 1, 2, and 3. In addition, for Cartesian TSE, the Partial Fourier Factor (PFF) was selected from the following: $[\frac{9}{16}, \frac{3}{4}, 1]$. In addition to this parameter space, single-shot Cartesian TSE sequences acquired in one T_R (4s) were included by

removing ETL constraints; these sequences are referred to as HASTE-type sequences. The maximum echo train length of these sequences was equal to the matrix size (384) and had a PFF = 1 and R = 1. The minimum echo train length of these HASTE sequences was 72 and had a PFF = $^{9}/_{16}$ and R = 3. Combinations of sequence parameters that were unfeasible due to hardware limitations were excluded.

Within this parameter space is the Cartesian TSE sequence that resembles clinical sequences used now in prostate biopsy (ETL = 16, ESP = 8, R = 1, PFF = 1, T_{acq} = 96s); this sequence is used as a gold-standard for comparison of other accelerated sequences. This sequence parameter space enables simulations of Cartesian sequences with total acquisition times of 4s, 8s, 16s, 24s, 32s, 48s, 64s, and 96s and spiral sequences with acquisition times of 4s, 8s, 16s, 24s, 32s, 56s, and 112s.

Spiral TSE

To simultaneously mitigate T_2-decay-induced spiral artifacts and off-resonance artifacts while minimizing reconstruction and acquisition overhead, a modified double encoding strategy, outlined in Figure 5-3, is used. Here a second acquisition with both a reversed view order as demonstrated in Li et al[106] and redundant trajectory retracing as demonstrated in Fielden and Meyer[136] is collected. This scheme simultaneously mitigates artifacts due to T_2-decay-induced signal modulation and off-resonance without additional B_0 maps, although the acquisition time is doubled compared to uncorrected spiral TSE sequences.

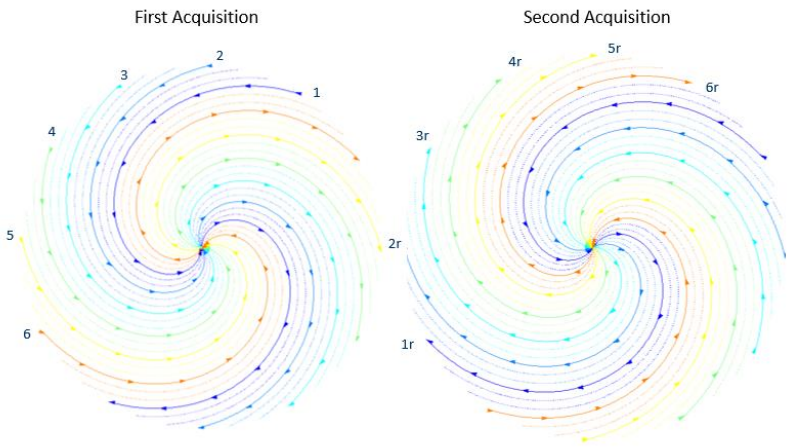

Figure 5-3: The view order and sampling directions of the first and second acquisitions of the corrected spiral TSE acquisition. (Left) In the first acquisition, each spiral arm is sampled in the numerical order indicated by both the number and color. The direction that the spiral trajectory traverses during the readout is indicated by the colored arrows. Lines that are left uncollected that will be reconstructed are dotted, in this case for R=3. (Right) During the second acquisition, each interleaf is retraced but with a reversed view order and readout direction (indicated by the arrows and r designation)

A spiral in/out trajectory was designed in consideration of the modified double encoding strategy and the requirements suggested for the redundant trajectory retracing to mitigate off-resonance artifacts. The redundant trajectory retracing causes a cosine amplitude modulation over k-space, dependent on the amount of phase accumulated over the readout due to off-resonance. Given that the total phase accumulated over the readout is less than π, the resulting cosine amplitude modulation leads to a mild attenuation of high-frequency components and corresponding image blur. Further reduction of the accumulated phase, such as by shortening the readout duration, reduces the degree of attenuation and associated blurring. However, to cover k-space with shorter duration spirals would requires a larger number of interleaves which would contribute to longer acquisition times. Given that off-resonance values in the prostate are rarely greater than 100Hz[126] a maximum readout time of 5ms was used as a constraint to design a spiral in/out trajectory with 108 interleaves and a readout duration of

3.23ms for a field of view of 400mm^2 and an in plane resolution of 1.04mm x 1.04mm.

Reconstruction

Simulated partial Fourier Cartesian TSE data were reconstructed with projection over convex sets algorithm[137] and FFT. Simulated spiral TSE data were reconstructed with algorithms described in Li et al[138] and Fielden and Meyer[136] for corrections using modified doubled encoding strategy, then transformed to an image using NUFFT. No additional off-resonance corrections were applied during reconstruction. It was assumed that undersampled acquisitions would be reconstructed without additional noise or artifacts in order to focus on the selection of sequence parameters; thus uncollected lines were filled with simulated data.

Image Quality

Quantitative image quality metrics of image sharpness, contrast, and artifact power were used to compare the performance of each set of sequence parameters. Image sharpness was measured as the 10%-90% rise time of lesion edges from healthy tissue to lesion tissue and is expressed as a percent ratio relative to the gold standard. Image sharpness was measured in eight radially symmetric line profiles through the lesion edge for each lesion and then averaged to obtain an overall image sharpness metric for the entire image. Contrast was measured as the ratio between mean lesion signal and mean healthy tissue signal. Prior to calculating the contrast metrics, each image was windowed and leveled such that the relative signal intensity of the healthy tissue

background and largest lesion with average T_2 was similar across all simulations. The measured contrast is expressed as a percent ratio relative to the gold standard and averaged over every lesion to obtain an overall contrast metric for the image. Contrast was only assessed in the TZ and PZ phantoms, as only these phantoms had variable lesion relaxation values. Artifact power was measured as the Shannon entropy[139] of the healthy tissue regions of the image. The histogram of the healthy region grayscale pixel intensities is generated from 256 bins and the Shannon entropy is calculated as:

$$Entropy = \sum p(i)\ log\ p(i)$$

where $p(i)$ is the relative frequency of the i^{th} bin. Healthy tissue regions of the four phantoms used in this study were designed to have a constant signal magnitude and thus zero entropy, and thus a non-zero entropy measurement in the healthy tissue region can be attributed to image artifacts. Due to expected contrast differences between sequences, artifact power was not quantified in lesion tissue. An overall artifact power metric is expressed as a percent ratio relative to the measured gold standard artifact power. The overall image quality score for each sequence is the average of the image sharpness, contrast, and artifact power metrics over all tested phantoms.

5.3: Results

In Figure 5-4 and Figure 5-5, images from the sequences with the lowest image quality score (indicating the best overall images) for each acquisition time are shown for each phantom variant for both Cartesian and spiral sampling trajectories. Highly accelerated Cartesian TSE images have reduced edge

sharpness around the lesions and ringing artifacts. At acquisition times of 16s and greater, Cartesian TSE images appear comparable to the gold standard images. In contrast, images simulated with accelerated spiral TSE sequences have swirl-like artifacts within lesions and streaking artifacts across the field of view. These artifacts are reduced when using an acquisition time of at least 16s, but some residual artifacts remain resulting in variable image intensity in the healthy tissue regions.

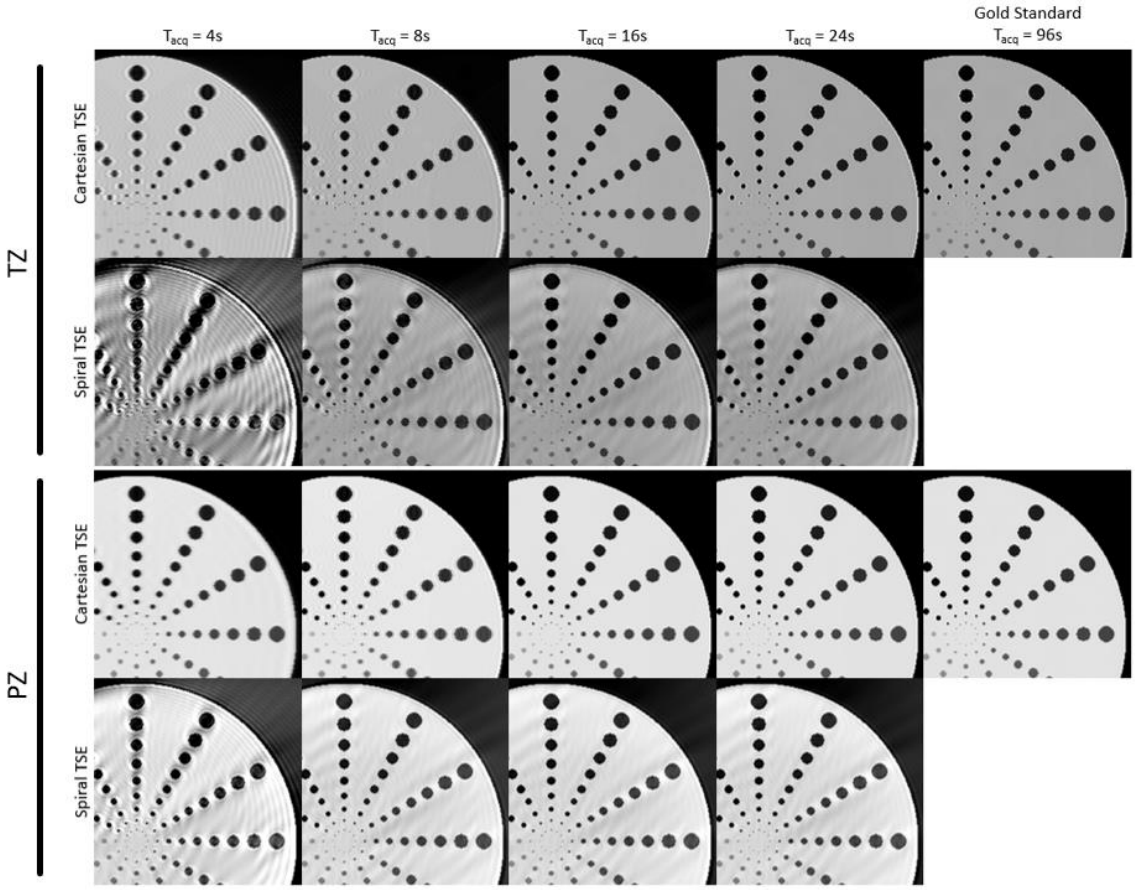

Figure 5-4: Zoomed image of simulated Cartesian and spiral TSE images of sequences with best image quality performance, determined by lowest image quality score, in both the transition zone phantom (Top) and peripheral zone phantom (Bottom). Right to left is the phase encoding direction for the Cartesian sequences. Sequence parameters can be found in Table 5-2. Cartesian sequences show blurring and ringing in the phase encoding direction due to T_2 decay over k-space with reduced acquisition time. In spiral imaging, T_2-decay induced "swirl" artifacts worsen with reduced acquisition time. These T_2-decay effects can be seen to worsen in the transition zone which has lower lesion T_2 values and in darker lesions which have lower T_2.

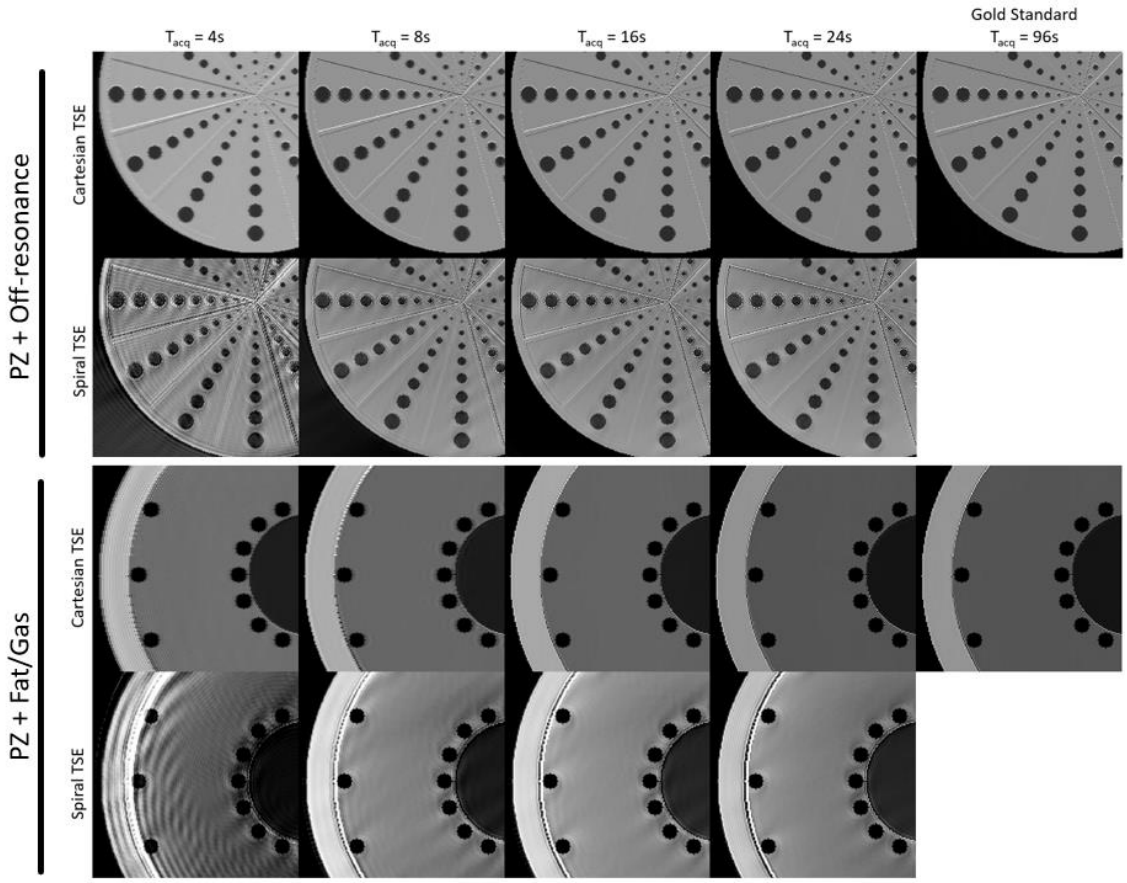

Figure 5-5: Images generated using the PZ + off-resonance and PZ + fat/gas phantoms. Right to left is the phase encoding direction for the Cartesian sequences. (Top) Zoomed portion of peripheral zone in the off-resonance phantom. In this portion of the phantom, the lesion off-resonance is set to 40Hz, and the background off resonance increases clockwise from 0Hz, 50Hz, 100Hz, 200Hz. Cartesian sequences show mild chemical shift artifacts in the read-out direction. Spiral TSE sequences show similar image quality despite further reduction of acquisition time, except at a 4s acquisition time where considerable streaking artifacts reduce lesion and lesion edge visibility. (Bottom) Zoomed portion of peripheral zone with fat/gas phantom. Larger off-resonance values in due to fat and rectal gas lead to larger chemical shift artifacts in both Cartesian and spiral acquisitions, though Cartesian image artifacts are mild relative to spiral TSE.

The image contrast between lesions and the healthy tissue background in the TZ and PZ phantoms is shown relative to the gold standard sequence in Figure 5-6. Spiral TSE has an altered contrast profile over the span of lesion T_2 values in both the TZ and PZ phantoms. When using an acquisition time of 16s, spiral TSE in the TZ and PZ phantoms shows increased contrast in lesions with T_2 values below the average lesion T_2 (TZ - 36ms, PZ – 56ms). Cartesian TSE, when using the same acquisition time of 16s, has comparable contrast to the

gold standard with less than a 1% difference in lesion contrast over the lesion T_2 range. With T_{acq} < 16s, differences between spiral TSE and the gold standard have no discernable pattern while differences in Cartesian TSE have lower contrast at low T_2 values. However, for highly accelerated sequences, spiral TSE has greater image contrast when averaged over the lesion T_2 range compared to both Cartesian TSE at equivalent acquisition time and the gold standard sequence.

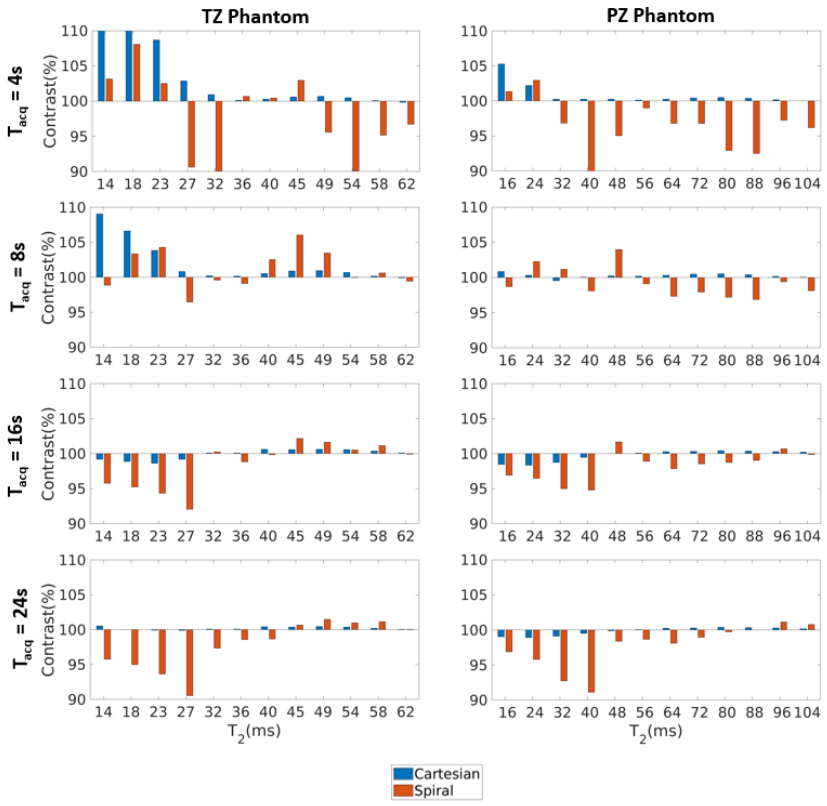

Figure 5-6: Contrast between lesion and healthy tissue background for the best image quality performance (e.g. lowest image quality score) by acquisition time relative to the gold standard sequence (% contrast = 100). A relative contrast measurement of 100% indicates that the contrast of the accelerated scan is equivalent to that of the gold-standard; values greater than 100% indicate that the contrast between that lesion and the background is lower than the gold standard. Conversely, contrast values less than 100% indicate that the contrast between the lesion and background is superior to the gold standard (Left) In transition zone phantom, images collected using spiral TSE with acquisition times of 24 and 16s have a higher contrast in low T_2 lesions compared to the gold standard sequence; Cartesian acquisitions lead to lower contrast for lower T2 value lesions for these acquisition times. At lower acquisition times, spiral TSE does not have a predictable contrast pattern due to T_2-decay spiral artifacts within the lesions. (Right) In the peripheral zone phantom, spiral TSE has consistently greater contrast over the lesion T_2 range than both Cartesian TSE sequences collected at similar acquisition time and the gold standard Cartesian sequence.

The image sharpness relative to the gold-standard image is shown in Figure 5-7 for the sequences with the best image quality performance (e.g. lowest image quality score) at each acquisition time for both Cartesian and spiral sampling trajectories; a value greater than 100% suggests that the measured rise time at lesion edges was larger than in the gold standard on average, and the image is thus less sharp than the gold standard. As the acquisition time decreases, image sharpness for both Cartesian and spiral sampling trajectories also decreases in every phantom variant. The reduced image sharpness is most significant in the TZ phantom, where the average rise time of a lesion edge of a Cartesian TSE sequence acquired in 4s was 76% longer relative to the gold standard. Cartesian TSE acquired in 24s has modest reduction in image sharpness across all phantom variants, with a 4.9% increase in average rise time at lesion edges. In the PZ and PZ + Off-resonance phantoms, not only did spiral TSE had shorter measured rise time compared to Cartesian TSE with similar acquisition times, but spiral TSE at acquisition times of 8s and greater also had shorter measured rise time relative to the gold standard. However, using an acquisition time of 16s results in images with comparable image sharpness to the gold-standard. In contrast, images generated using Cartesian TSE have longer measured lesion edge rise time at shorter acquisition times, although images acquired in 24s or more have comparable sharpness to the gold standard images. In the PZ + fat/gas phantom, while Cartesian TSE had a similar pattern of decreased image sharpness at an acquisition time of 8s to the other peripheral zone phantoms, spiral TSE had additional artifacts due to high off-resonance

sources resulting in decreased measured image sharpness, which was lower than Cartesian TSE except at an 8s acquisition time.

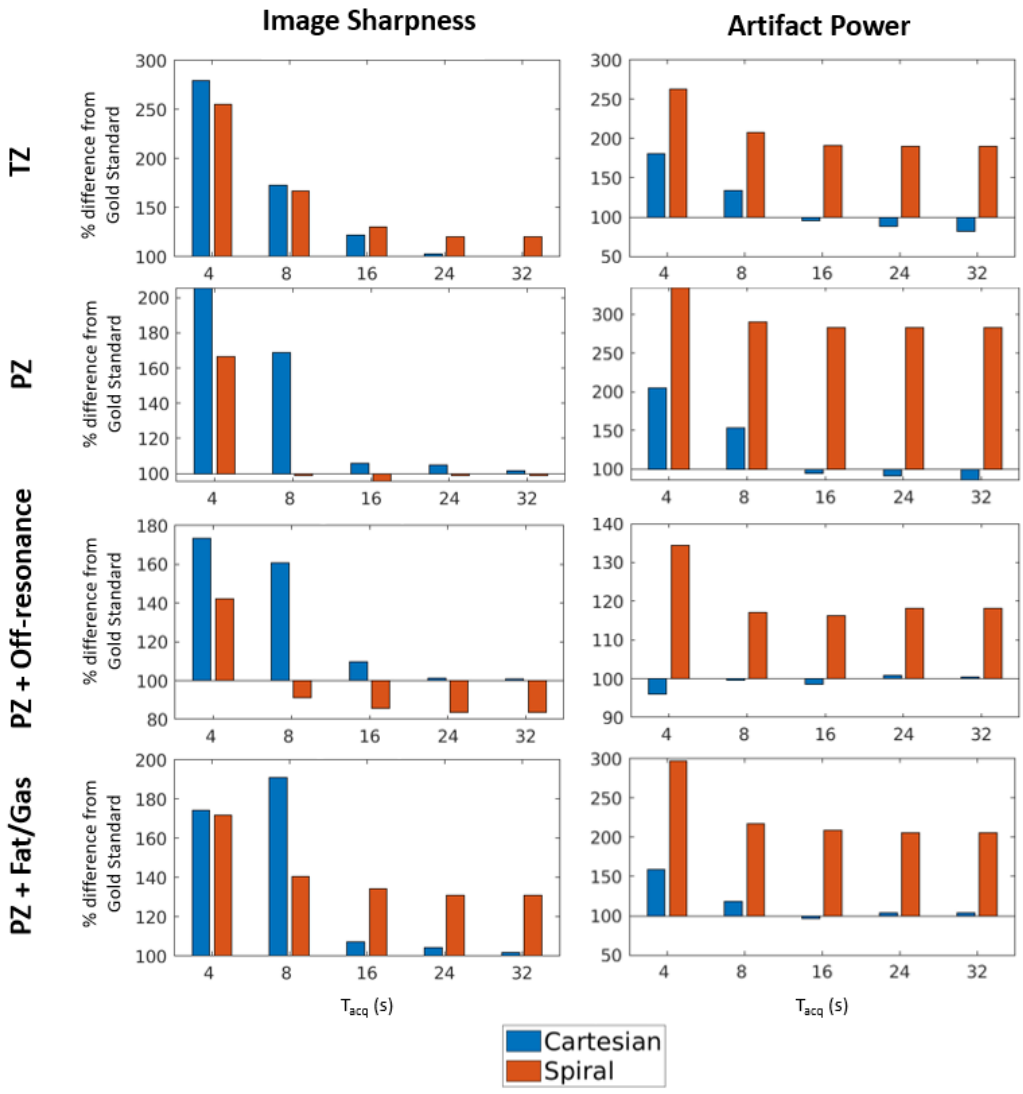

Figure 5-7: Measured image sharpness and artifact power for sequence parameters with the best image quality performance (e.g. lowest image quality score) at each acquisition time relative to the gold standard sequence (% difference = 100). Lower values indicate greater image quality for both image sharpness and artifact power. (Left) In the PZ and PZ+Off-resonance phantom, spiral TSE has superior image sharpness compared to Cartesian TSE. Image sharpness in the TZ phantom is comparable between Cartesian and spiral TSE. Lesions in the PZ + Fat/Gas phantom are close to off-resonance sources that result in chemical shift; the resulting artifact results in larger rise time measurement due to difficulty of distinguishing lesion edges with healthy tissue or artifacts. (Right) Spiral TSE has increased artifact power compared to Cartesian TSE over all acquisition times and phantom variants.

Figure 5-7 also shows changes in measured artifact power resulting from reduced acquisition times. Spiral TSE has higher artifact power for every

phantom variant at all acquisition times compared to Cartesian TSE. Both spiral and Cartesian TSE have sharp increases in artifact power relative to the gold standard sequence at an acquisition time of 8s in the TZ and PZ phantoms, and at an acquisition time of 4s in the PZ + Fat/Gas phantoms. In the PZ + Off-resonance phantom, artifact power in the Cartesian TSE sequences are not associated with acquisition time. For all phantoms, artifact power in spiral TSE is much larger than Cartesian TSE.

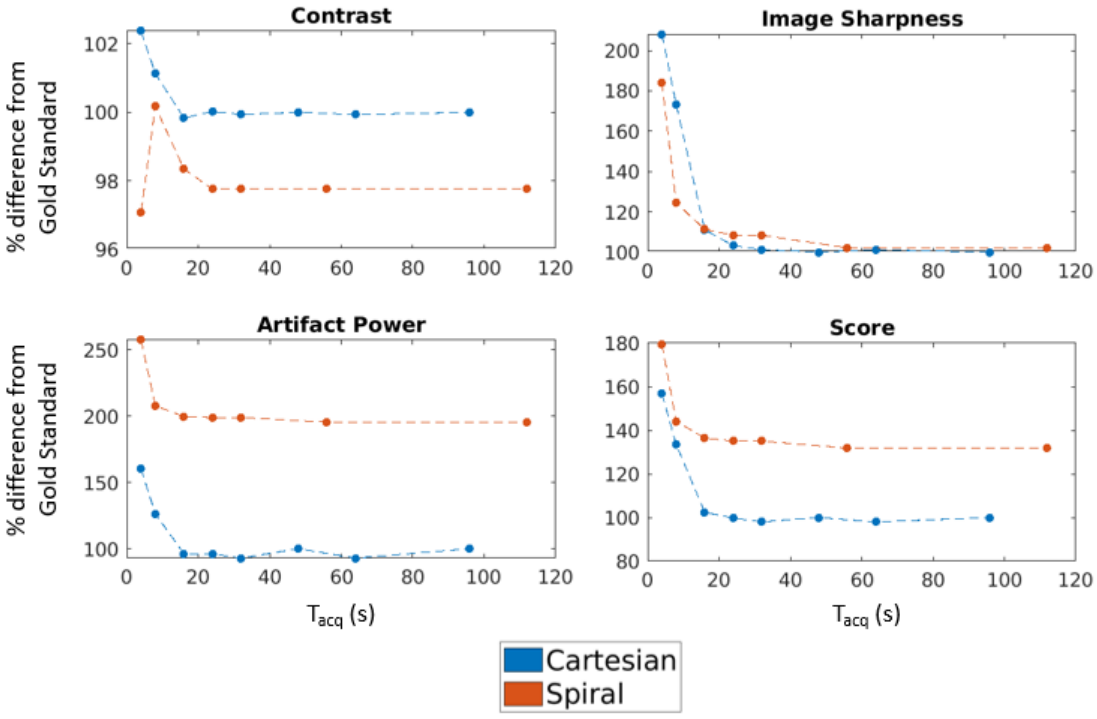

Figure 5-8: Overall image quality metrics for sequences with the best image quality performance (e.g. lowest image quality score) at each acquisition time relative to the gold standard sequence (% difference = 100). Gold standard corresponds to point on Cartesian graphs at a T_{acq} = 96s. Lower image quality metric values correspond to greater image quality. For all image quality metrics, reducing the acquisition time results in a rapid rise in image quality metrics and correspondingly lower image quality. In the 16s-24s acquisition time regime, both Cartesian and spiral TSE sequences have comparable image quality to longer counterparts. (Top Left) Spiral TSE has better contrast than Cartesian TSE, including the gold standard over the entire acquisition time range. (Top Right) Cartesian TSE and Spiral TSE have comparable image sharpness, with spiral TSE having sharper images at lower acquisition times where Cartesian TSE has considerably longer echo train lengths that contribute to blur. (Bottom Left) Spiral TSE has greater artifact power than Cartesian TSE over the entire acquisition time range. (Bottom Right) Based on the image quality score metric in this work, overall performance of Cartesian TSE is superior over the entire acquisition time range.

In Figure 5-8, the overall image quality metrics of sequences with the best image quality performance at each acquisition time are shown. The overall image quality score, which is the product of each of the averaged relative image quality metrics, indicates that the acquisition time for Cartesian TSE can be reduced to 24s while maintaining image quality comparable to the gold standard. Further reducing acquisition time to 16s leads to only a 7% increase in image quality score. Despite the higher contrast and image sharpness compared to the gold-standard, images collected with spiral TSE have an overall lower image quality compared to the gold standard at all acquisition times due to significant artifact power.

The sequence parameters of the best performing sequences at acquisition times of 4s, 8s, 16s, 24s are shown in Table 5-2, with their corresponding image quality metrics relative to the gold standard sequence. For Cartesian TSE, the best performing sequences generally had the shortest possible echo train length for each acquisition time without partial Fourier acquisition, as partial Fourier acquisitions lead to higher artifact power. For an acquisition time of 4s, using partial Fourier acquisition to reduce echo train length improved the measured image sharpness at the cost of additional artifact power that resulted in an overall reduction in image quality score. At an acquisition time of 24s, the total image quality score for the best performing Cartesian TSE sequence is 1, which is equivalent to the gold standard. For spiral TSE, reducing the ETL was also the best strategy to achieve the best image quality for a given acquisition time. Spiral

TSE sequences that have been corrected by the modified double encoding strategy had a higher level of performance compared to uncorrected spirals.

Acquisition Time (s)	Cartesian TSE								Spiral TSE						
	Sequence Parameters				Image Quality Metrics				Sequence Parameters			Image Quality Metrics			
	ETL	ESP	PFF	R	CON	IS	AP	Score	ETL	ESP	R	CON	IS	AP	Score
4	96	5	3/4	3	1.02	2.08	1.60	1.57	40'	8'	3'	.97	1.84	2.57	1.80
	128	5	1	3	1.02	2.16	1.61	1.60	48'	8'	3'	.97	1.84	2.57	1.80
	72	5	9/16	3	1.01	2.15	1.77	1.64	48'	5'	3'	.98	1.90	2.64	1.84
8	48	5	3/4	3	1.01	1.73	1.26	1.34	40	8	3	1.00	1.24	2.08	1.44
	56	5	3/4	3	1.01	1.75	1.27	1.34	40	5	3	1.02	1.32	2.13	1.49
	64	5	1	3	1.01	1.84	1.18	1.34	48	8	3	1.00	1.38	2.22	1.54
16	32	5	1	3	1.00	1.11	.96	1.03	24	8	3	.98	1.11	2.00	1.36
	40	5	1	3	1.01	1.30	1.03	1.11	24	5	3	.99	1.12	2.01	1.37
	24	5	3/4	3	1.00	1.19	1.25	1.15	24	11	3	.99	1.15	2.02	1.38
24	24	5	1	3	1.00	1.03	.96	1.00	16	8	3	.98	1.08	1.99	1.35
	32	5	1	2	1.00	1.12	.94	1.02	24	8	2	.98	1.11	2.00	1.36
	24	8	1	3	1.01	1.22	1.08	1.10	24	5	2	.99	1.12	2.01	1.37
96 (Gold Standard)	16	8	1	1	1	1	1	1	No modified double encoding strategy applied for correction						

Table 5-2: Sequence parameters for the top three performing accelerated sequences at different acquisition times. Image quality metrics for each sequence parameter set are also shown for image contrast (CON), image sharpness (IS), artifact power (AP), and overall image quality score (Score). Image quality metrics are relative to the gold standard, with measured values less than one indicating greater image quality performance than the gold standard. Best performing sequences in each acquisition time category are typically those with the shortest echo train length, though partial Fourier acquisition leads to an increase in artifact power that does not provide a sufficient benefit except at long echo train lengths at acquisition times of 4s and 8s.

5.4: Discussion

In this work, different options for rapid collection of T_2-weighted images were assessed in simulation, with examples for the specific application of in-bore prostate biopsy. Based on the results these simulations, it may be possible to accelerate T2-weighted imaging for prostate biopsy from current times of 96s to 24s without significant degradation in image quality.

Image contrast is one of the largest sources of value provided by MRI for image-guided intervention, such as prostate biopsy, and thus is a key image quality metric for fast imaging sequences. In contrast to Cartesian TSE, where view ordering can be used to control the contrast in the final image, each shot in

spiral TSE contributes to the overall image contrast. It was previously reported that this effect leads to improved contrast in the brain[106]. In the prostate, spiral TSE does have higher image contrast between lesions and background tissue compared to Cartesian TSE sequences collected at similar acquisition times, and often has greater contrast than the gold standard at many acquisition times and for many lesion T_2 values (Figure 5-6). However, the improvement in contrast is small, and is, on average, 2% higher than the gold standard. Compared to GRE sequences[140,141], which have considerably altered contrast that prevents visualization of most prostate lesions, spiral TSE provides excellent tissue contrast that is comparable to Cartesian TSE.

T_2-decay-induced signal modulation is source of artifacts in TSE sequences that has ramifications for image quality in both Cartesian and spiral TSE. The primary source of blur in Cartesian TSE is T_2-decay, which causes significant loss of image sharpness in the transition zone due to lower lesion T_2 values. In Cartesian TSE, the view order of phase encoding lines typically places later echoes in the periphery of k-space, which results in an attenuation of high-frequency signals. This leads to a non-uniform apodization effect along the phase encoding direction, resulting in blurring dependent on T_2 (Figure 5-9). Thus, sequences with minimized echo train lengths, which reduces T_2-decay over k-space, have the best performance in terms of image sharpness. Another impact of T_2-decay in Cartesian TSE images is the so-called pseudo-edge enhancement artifact. Due to a widening of the point spread function, constructive signal interference at edges between tissues with considerably different T_2 values can

form a bright edge. For prostatic lesions, this effect was observed primarily in transition zone lesions with T_2 values of less than 27ms. These lesions would be relatively rare in practice, so this artifact should not impact image quality in most cases.

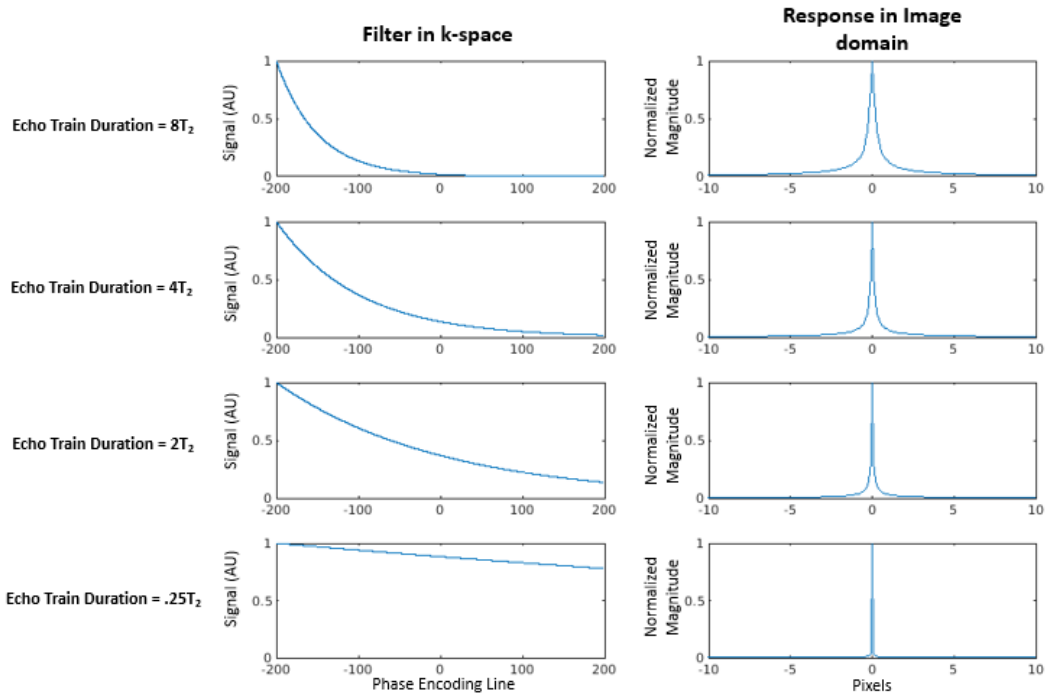

Figure 5-9: Figure showing simulated blur in the image domain due to T_2 decay over the phase encoding direction. Echo train duration refers to the echo train length multiplied by the echo spacing. As the amount of T_2 decay decreases (going down), the point spread function narrows and image sharpness is improved.

In comparison to Cartesian TSE, T_2-decay induced signal modulation in spiral TSE results in low signal intensity contributions from interleaves collected at later echo times, reducing signal throughout k-space. A spiral undersampling analogy can be used to explain this phenomenon, where low signal interleaves are analogous to uncollected lines and produce aliasing-like artifacts. With correction from the modified double encoding strategy, these T_2-decay artifacts are noticeably reduced but not fully eliminated, leading to ringing-like artifacts that reduce contrast and increasing artifact power. However, unlike Cartesian TSE,

T_2-decay effects do not cause significant blurring. This is a potential trade-off between the two sampling trajectories that should be considered for prostate biopsy, in particularly for small lesions where improved image sharpness can increase targeting accuracy.

T_2-decay effects in Cartesian and spiral TSE both result in image changes that can also impact image contrast. At short acquisition times of 4s and 8s, blurring and ringing artifacts in Cartesian TSE resulted in an increase in lesion brightness at low T_2 values in both the TZ and PZ phantoms (Figure 5-4) that led to a measurable reduction in image contrast relative to the gold standard (Figure 5-6). Similarly, T_2-decay induced spiral artifacts in spiral TSE within the lesions resulted in a measured reduction in lesion contrast.

Pelvic imaging has several sources of off-resonance and chemical shift which can cause artifacts that degrade image quality. Compared to Cartesian TSE, off-resonance effects present a major challenge for spiral imaging, as the longer readout leads to an increase in phase accumulation compared to Cartesian acquisitions. Off-resonance and chemical shift effects in Cartesian TSE manifest as pixelwise shifts in the frequency encoding direction, leading to characteristic bright and dark bands due to signal overlap between shifted off-resonant tissue and unshifted tissue with sufficiently large chemical shifts, and partial volume effects with small off-resonance values leading to mild loss of edge sharpness. In spiral TSE, off-resonance artifacts appear as radially symmetric chemical shift artifacts (Figure 5-5). Off-resonance effects can also cause streaks and signal dropout in non-Cartesian imaging due to partial phase cancellations during

gridding. With the modified double encoding strategy presented in this work, and a short spiral readout of 3.23ms, small off-resonant shifts up to 155Hz are reduced and instead cause mild blurring. In the PZ + off-resonance phantom, the blurring caused by this effect had a smaller impact on measured average image sharpness than the chemical shift artifacts that occurred with Cartesian TSE. However, at higher off-resonance values, spiral TSE exhibits considerable ringing and blurring artifacts as observed in the PZ + Fat/Gas phantom. While these artifacts would normally occur outside the prostate region, additional B_0 correction could potentially improve overall image quality.

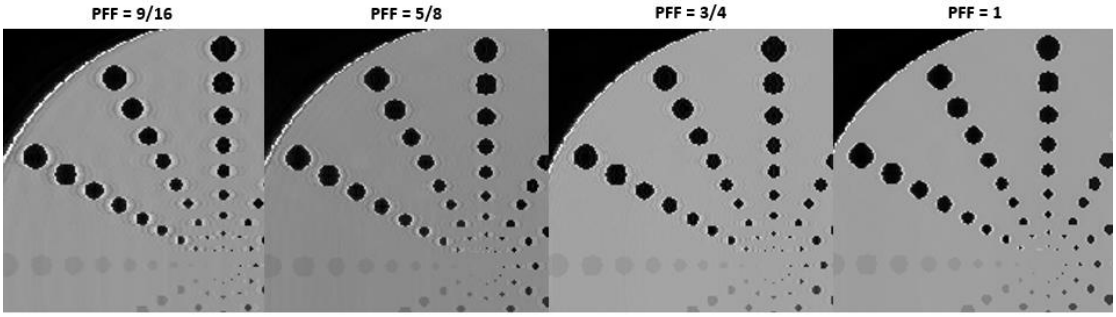

Figure 5-10: PZ phantom simulated using a Cartesian TSE sequence with ETL = 24, ESP = 5, and R = 3 with varying partial Fourier factor. Partial Fourier factor of 1 is fully sampled. As the partial Fourier factor decreases, the individual lesions appear blurrier and additional ringing artifacts appear.

Based on the results of this work, it may be possible to reduce the time needed to collect T_2-weighted images for in-bore MR-guided prostate biopsy from 96s to 24s without a significant reduction in image quality by using a higher acceleration factor and echo train length with a Cartesian sampling trajectory. While spiral TSE does not perform as well as Cartesian TSE, other corrections such as off-resonance corrections or a KWIC filter may reduce artifact power and make spiral TSE an appealing choice for acceleration. The simulated data also indicates that the single-shot sequences examined as part of this work, HASTE

and uncorrected spiral TSE, considerably degrade image quality. HASTE sequences have poor image sharpness as measured in Figure 5-7 and appear visually blurry in both the transition and peripheral zone, as seen in Figure 5-4. Partial Fourier acquisition decreases blur but leads to additional artifacts, even after applying the POCS reconstruction, that lead to an overall decrease in image quality based on the image quality metrics presented in this work (Figure 5-10). However, for large lesions where blur and lesion visibility are less of a concern, HASTE may be suitable for image guidance. When targeting smaller lesions, Cartesian TSE with longer acquisition time should be used to resolve smaller targets with minimal blur (Figure 5-7). Single-shot spiral TSE without corrections has significant image artifacts that not only obscure small lesions (Figure 5-4) but lead to streaks over the whole field-of-view (Figure 5-5) in the presence of off-resonance. Thus, spiral TSE requires corrections to mitigate these artifacts and prevent degradation of image quality. With corrections applied with the modified double encoding strategy, single-shot spiral TSE has an acquisition time of 8s. In comparison with Cartesian TSE collected in the same acquisition time, single-shot spiral TSE with corrections has higher image sharpness and contrast but comes with nearly twice as much artifact power. While spiral TSE does perform worse overall compared to Cartesian TSE, improved image sharpness and contrast provided by spiral TSE may be useful for targeting small, intermediate grade lesions.

Reducing the acquisition time of T_2-weighted imaging could greatly improve imaging efficiency during in-bore MR-guided prostate biopsy procedures. Faster

imaging can impact clinical workflow for prostate biopsy by reducing visual feedback latency and enabling use of procedure robotics. Most importantly, with faster imaging and thus faster MR-guided biopsy procedures, the MR scanner can be made available for a larger volume of patients, increasing accessibility to the highest sensitivity and specificity biopsy technique for prostate cancer[142].

This work has several limitations. Due to highly variable pelvic anatomy and presentation of prostate lesions on imaging, a single anatomically correct phantom model may be representative of only a narrow slice of the potential patient population, and as a result, more generalized uniformly shaped phantoms were designed to be agnostic to individual variation. However, the combination of image quality metrics from these digital phantoms to obtain an overall score is subjective and dependent on the needs of application that is to be optimized. Other clinical applications may value specific image quality characteristics such as contrast, and certain designed digital phantoms may more closely replicate the use case of the technology being optimized. Thus, different weighting factors could be applied to calculating the mean imaging metrics or even to determine the contributions of individual digital phantoms for a given use-case.

In addition, the reconstruction of accelerated datasets (R=2 and R=3) was assumed to be ideal and was not explicitly modeled. In reality, accelerated images would suffer from a loss in SNR, along with other reconstruction-induced artifacts. Noise was also not modeled in simulation, and the performance of different sequences at different noise levels was not considered. While the digital phantoms used in this study were designed to be proxies for in vivo prostate

biopsy, no anatomically correct model was designed. Furthermore, in vivo data were not collected to confirm the sequence assessments in this work.

One aspect of TSE not addressed in this study is the impact of refocusing flip angle. By modeling all refocusing pulses as ideal 180-degree flip angles, the effects of stimulated echoes, which add additional T_1 contrast, are mitigated. However, low flip angle and variable flip angle schemes can reduce the total signal variation due to T_2-decay over the echo train, reducing blur at the cost of altering contrast. In Cartesian TSE in particular, variable flip angle schemes like smooth transitions between pseudo steady states (TRAPS)[143] could be used to reduce blurring by flattening the T_2-decay-induced apodization filter over k-space. Other variable flip angle schemes[143,144] can be designed to reach a steady state, which could eliminate T_2 decay from both Cartesian TSE and spiral TSE. Alternatively, reduction of the read-out time could be achieved by using different trajectory designs such as a variable density spiral[33] or WHIRL[34] which may prove to be more suited for prostate applications due to the prevalence of off-resonance sources.

5.5: Conclusion

In this work, a simulation study was performed over a range of sequence parameters for accelerated T_2-weighted imaging, specifically for use in in-bore MR-guided prostate biopsy. Based on the results of this simulation, the acquisition time of the 96s Cartesian TSE sequence currently used for guidance imaging could be reduced to 24s without degradation in image quality; a reduction of the acquisition time further to 16s may be possible with a minor

reduction in image quality. While spiral TSE was demonstrated to have higher image sharpness and contrast characteristics compared to Cartesian TSE, these acquisitions lead to additional artifacts that reduced their performance in the simulated prostate biopsy setting.

Chapter 6 Conclusions and Future Directions

6.1: Summary

In this thesis, several approaches to optimize MR imaging for clinical applications by identifying a clinical aspect of imaging that needed improvement and optimizing towards that goal.

First in chapter 3, fast cardiac CINE imaging using through-time radial GRAPPA was optimized using coil compression and weight sharing to reduce both acquisition and reconstruction time by leveraging a data compression to minimize required ACS data and local k-space geometry to share GRAPPA weights. Optimized parameters for coil compression and weight sharing applied to reconstructions enables 66ms/frame temporal resolution and 2.34mm x 2.34mm spatial resolution while reducing calibration acquisition time from 34s to 6.7s, weight calculation time from 200s to 3s, and weight application time 18s to 5s. These optimizations applied to through-time radial GRAPPA enables fast free-breathing ungated cardiac cine in a clinically feasible timeframe without compromising image quality.

In chapter 4, cardiac MRF dictionary simulation was optimized and implemented online via the Gadgetron framework. In phantom experiments, there are no significant differences in T1 or T2 measurements between the Gadgetron-based and offline MATLAB reconstructions. In vivo Tissue property maps showed no statistically significant difference between the two reconstructions in the myocardium or blood. The Gadgetron implementation reduced the total reconstruction time by 64% from 62.5s to 22.5s, and has the additional benefit of

providing the tissue property maps directly at the scanner. The Gadgetron implementation of cMRF yields accurate quantitative myocardial T1 and T2 maps while eliminating data transfer overhead by processing raw data and outputting maps directly to clinical MR systems, which improves clinical workflow and efficiency.

Finally in Chapter 5, a spiral TSE acquisition with a double encoding strategy to mitigate T_2-decay and off-resonance effects was proposed as a fast-imaging candidate for MR-guided in-gantry prostate biopsy. The proposed spiral TSE acquisition was compared to currently used Cartesian TSE on an image quality per unit acquisition time basis via simulations. Spiral TSE was shown to have better blur performance from T_2-decay effects compared to Cartesian TSE but had poor image quality in the presence of strong off-resonance sources like fat or gas. Off-resonance artifact mitigation from the proposed double encoding strategy did reduce both T_2-decay based swirl artifacts and off-resonance blurring but can be improved by additional B_0 correction in the future. Further optimizations of both Cartesian and spiral TSE may be possible using compressed sensing or machine learning reconstructions.

6.2: Future Directions

Exploration of other Non-Cartesian Trajectories for TSE

One pitfall of the spiral TSE approach is the sensitivity to off-resonance effects that results from long readout times. While long readout times can be reduced by increasing the number of spiral interleaves, this approach minimizes the acquisition time benefits from reducing the number of phase encoding steps.

Other sampling approaches that can reduce readout time may have fewer imaging artifacts while retaining fast acquisition time. At one extreme, radial TSE uses many projections with minimized readout duration comparable to Cartesian TSE. In addition, radial GRAPPA is more robust to higher acceleration factors which may mitigate the increased number of phase encoding steps required for projection imaging. However, the radial trajectory repeatedly samples the center of k-space leading to contrast mixing and artifacts associated with T_2-decay. Usage of a k-space weighted image convolution filter (KWIC) to eliminate contrast mixing from echoes collected away from the intended effective T_E can potentially mitigate this effect but comes at the cost of scan efficiency, as collected data must be thrown out. An intermediary trajectory between spiral and radial sampling is the WHIRL trajectory[34] which increases the acquisition speed and improves the off-resonance properties of a spiral, but improvements are likely to be modest at best. At the other extreme, a single interleaf spiral sampling scheme can be performed by segmenting the spiral into a series of equal duration spiral segments and acquiring data at each echo with a different segment[145]. This approach has the advantage of solving the contrast mixing problem at the center of k-space for non-Cartesian TSE, as the center of k-space is sampled only with the central segment of the segmented spiral interleaf. However, this approach lacks compatibility with non-Cartesian GRAPPA as any under sampling would be non-uniform. In addition, phase errors due to off-resonance can introduce additional artifacts. Parallel imaging with compressed sensing may be one way to enable further acceleration.

Low field sequence optimization for prostate intervention

Another approach to minimize off-resonance artifacts is to optimize spiral TSE for low field systems. Off resonance frequencies are directly proportional to B_0 field strength, and low-field systems can minimize the maximum off-resonance in a sequence which can minimize blur and chemical shift artifacts due to fat and gas. Not only would one of the major disadvantages of spiral imaging, namely it's sensitivity to off-resonance effects, be minimized at lower field, but longer spiral readouts reducing the number of interleaves and further accelerating acquisition. However, low field imaging also provides less SNR, which is particularly problematic in prostate MRI which is often performed at 3T to maximize signal and enable the use of external pelvic coils rather than an endo-rectal coil. With sufficient acquisition speed, SNR could potentially be recovered by acquiring additional averages.

Variable flip angle sequences

Variable flip angle sequences and smooth transitions between pseudo steady states (TRAPS) are both TSE flip angle trains that could provide better contrast and fewer artifacts in both Cartesian and non-Cartesian TSE sequences. Variable flip angle trains can be designed to read a pseudo steady state signal resulting in each echo having equal signal and not only allows spiral imaging without requiring a double encoding strategy to correct for swirl artifacts produced by T_2-decay induced signal modulation but also enables longer echo train lengths without loss of signal. However, these sequences significantly alter the effective T_E of TSE sequences, and further investigation is necessary to

determine if the contrast provided by variable flip angle TSE is sufficient to visualize prostatic lesions. TRAPS is another variable flip angle sequence that produces a temporary pseudo-steady state during which data could be acquired. In theory, TRAPS allows for even greater signal than pseudo-steady state variable flip angle schemes, and already has shown success in Cartesian imaging.

Bibliography

1. Elster AD. An index system for comparative parameter weighting in MR imaging. *J Comput Assist Tomogr*. 1988;12(1):130-134. doi:10.1097/00004728-198801000-00025

2. Saloner D. The AAPM/RSNA physics tutorial for residents. An introduction to MR angiography. *Radiographics*. 1995;15(2):453-465. doi:10.1148/radiographics.15.2.7761648

3. Taylor DG, Bushell MC. The spatial mapping of translational diffusion coefficients by the NMR imaging technique. *Phys Med Biol*. 1985;30(4):345-349. doi:10.1088/0031-9155/30/4/009

4. Merboldt KD, Hanicke W, Frahm J. Self-diffusion NMR imaging using stimulated echoes. *Journal of Magnetic Resonance (1969)*. 1985;64(3):479-486. doi:10.1016/0022-2364(85)90111-8

5. Guivel-Scharen V, Sinnwell T, Wolff SD, Balaban RS. Detection of proton chemical exchange between metabolites and water in biological tissues. *J Magn Reson*. 1998;133(1):36-45. doi:10.1006/jmre.1998.1440

6. Thulborn KR, Waterton JC, Matthews PM, Radda GK. Oxygenation dependence of the transverse relaxation time of water protons in whole blood at high field. *Biochimica et Biophysica Acta (BBA) - General Subjects*. 1982;714(2):265-270. doi:10.1016/0304-4165(82)90333-6

7. Uludağ K, Müller-Bierl B, Uğurbil K. An integrative model for neuronal activity-induced signal changes for gradient and spin echo functional imaging. *NeuroImage*. 2009;48(1):150-165. doi:10.1016/j.neuroimage.2009.05.051

8. Reeder SB, Sirlin C. Quantification of Liver Fat with Magnetic Resonance Imaging. *Magn Reson Imaging Clin N Am*. 2010;18(3):337-357. doi:10.1016/j.mric.2010.08.013

9. Burakiewicz J, Sinclair CDJ, Fischer D, Walter GA, Kan HE, Hollingsworth KG. Quantifying fat replacement of muscle by quantitative MRI in muscular dystrophy. *J Neurol*. 2017;264(10):2053-2067. doi:10.1007/s00415-017-8547-3

10. Narayanan S, Nayak K, Lee S, Sethy A, Byrd D. An approach to real-time magnetic resonance imaging for speech production. *J Acoust Soc Am*. 2004;115(4):1771-1776. doi:10.1121/1.1652588

11. Lee DC, Markl M, Dall'Armellina E, et al. The growth and evolution of cardiovascular magnetic resonance: a 20-year history of the Society for Cardiovascular Magnetic Resonance (SCMR) annual scientific sessions. *Journal of Cardiovascular Magnetic Resonance*. 2018;20(1):8. doi:10.1186/s12968-018-0429-z

12. Ehman RL, Felmlee JP. Adaptive technique for high-definition MR imaging of moving structures. *Radiology*. 1989;173(1):255-263. doi:10.1148/radiology.173.1.2781017

13. Ehman RL, McNamara MT, Pallack M, Hricak H, Higgins CB. Magnetic resonance imaging with respiratory gating: techniques and advantages. *AJR Am J Roentgenol*. 1984;143(6):1175-1182. doi:10.2214/ajr.143.6.1175

14. Lanzer P, Barta C, Botvinick EH, Wiesendanger HU, Modin G, Higgins CB. ECG-synchronized cardiac MR imaging: method and evaluation. *Radiology*. 1985;155(3):681-686. doi:10.1148/radiology.155.3.4001369

15. Deshmane A, Gulani V, Griswold MA, Seiberlich N. Parallel MR imaging. *J Magn Reson Imaging*. 2012;36(1):55-72. doi:10.1002/jmri.23639

16. Blaimer M, Breuer F, Mueller M, Heidemann RM, Griswold MA, Jakob PM. SMASH, SENSE, PILS, GRAPPA: how to choose the optimal method. *Top Magn Reson Imaging*. 2004;15(4):223-236. doi:10.1097/01.rmr.0000136558.09801.dd

17. Glover GH. Simple analytic spiral K-space algorithm. *Magnetic Resonance in Medicine*. 1999;42(2):412-415. doi:10.1002/(SICI)1522-2594(199908)42:2<412::AID-MRM25>3.0.CO;2-U

18. Bergin CJ, Pauly JM, Macovski A. Lung parenchyma: projection reconstruction MR imaging. *Radiology*. 1991;179(3):777-781. doi:10.1148/radiology.179.3.2027991

19. Ma D, Gulani V, Seiberlich N, et al. Magnetic resonance fingerprinting. *Nature*. 2013;495(7440):187-192. doi:10.1038/nature11971

20. Phys. Rev. 70, 460 (1946) - Nuclear Induction. Accessed September 26, 2022. https://journals.aps.org/pr/abstract/10.1103/PhysRev.70.460

21. Williamson MP. Drawing Single NMR Spins and Understanding Relaxation. *Natural Product Communications*. 2019;14(5):1934578X19849790. doi:10.1177/1934578X19849790

22. Is quantum mechanics necessary for understanding magnetic resonance? - Hanson - 2008 - Concepts in Magnetic Resonance Part A - Wiley Online Library. Accessed December 30, 2022. https://onlinelibrary.wiley.com/doi/10.1002/cmr.a.20123

23. Hahn EL. Nuclear Induction Due to Free Larmor Precession. *Phys Rev*. 1950;77(2):297-298. doi:10.1103/PhysRev.77.297.2

24. Hahn EL. Spin Echoes. *Phys Rev*. 1950;80(4):580-594. doi:10.1103/PhysRev.80.580

25. Markl M, Leupold J. Gradient echo imaging. *Journal of Magnetic Resonance Imaging*. 2012;35(6):1274-1289. doi:10.1002/jmri.23638

26. Mansfield P, Maudsley AA. Planar spin imaging by NMR. *Journal of Magnetic Resonance (1969)*. 1977;27(1):101-119. doi:10.1016/0022-2364(77)90197-4

27. Hinshaw WS. Image formation by nuclear magnetic resonance: The sensitive-point method. *Journal of Applied Physics*. 1976;47(8):3709-3721. doi:10.1063/1.323136

28. Glover GH, Pauly JM. Projection Reconstruction Techniques for Reduction of Motion Effects in MRI. *Magnetic Resonance in Medicine*. 1992;28(2):275-289. doi:10.1002/mrm.1910280209

29. Russek SE, Boss M, Jackson EF, et al. Characterization of NIST/ISMRM MRI System Phantom. In: *Proceedings of the International Society of Magnetic Resonance in Medicine*. ; 2012:2456.

30. Thompson RB, McVeigh ER. Flow-gated phase-contrast MRI using radial acquisitions. *Magn Reson Med*. 2004;52(3):598-604. doi:10.1002/mrm.20187

31. Coristine AJ, Chaptinel J, Ginami G, et al. Improved respiratory self-navigation for 3D radial acquisitions through the use of a “pencil-beam” 2D-T2-Prep in free-breathing, whole-heart coronary MRA. *Magn Reson Med*. 2018;79(3):1293-1303. doi:10.1002/mrm.26764

32. Aandal G, Nadig V, Yeh V, et al. Evaluation of left ventricular ejection fraction using through-time radial GRAPPA. *Journal of Cardiovascular Magnetic Resonance*. 2014;16(1):79. doi:10.1186/s12968-014-0079-8

33. Chang C, Glover GH. Variable Density Spiral-In/Out fMRI. *Magn Reson Med*. 2011;65(5):1287-1296. doi:10.1002/mrm.22722

34. Pipe JG. An optimized center-out k-space trajectory for multishot MRI: comparison with spiral and projection reconstruction. *Magn Reson Med*. 1999;42(4):714-720. doi:10.1002/(sici)1522-2594(199910)42:4<714::aid-mrm13>3.0.co;2-g

35. Liao JR, Pauly JM, Brosnan TJ, Pelc NJ. Reduction of motion artifacts in cine MRI using variable-density spiral trajectories. *Magnetic Resonance in Medicine*. 1997;37(4):569-575. doi:10.1002/mrm.1910370416

36. Lee Y, Wilm BJ, Brunner DO, et al. On the signal-to-noise ratio benefit of spiral acquisition in diffusion MRI. *Magnetic Resonance in Medicine*. 2021;85(4):1924-1937. doi:10.1002/mrm.28554

37. Glover GH, Lai S. Self-navigated spiral fMRI: Interleaved versus single-shot. *Magnetic Resonance in Medicine*. 1998;39(3):361-368. doi:10.1002/mrm.1910390305

38. Fessler JA. On NUFFT-based gridding for non-Cartesian MRI. *Journal of Magnetic Resonance*. 2007;188(2):191-195. doi:10.1016/j.jmr.2007.06.012

39. Oppenheim A, Johnson D, Steiglitz K. Computation of spectra with unequal resolution using the fast Fourier transform. *Proceedings of the IEEE*. 1971;59(2):299-301. doi:10.1109/PROC.1971.8146

40. Beylkin G. On the Fast Fourier Transform of Functions with Singularities. *Applied and Computational Harmonic Analysis*. 1995;2(4):363-381. doi:10.1006/acha.1995.1026

41. Hamilton J, Franson D, Seiberlich N. Recent advances in parallel imaging for MRI. *Prog Nucl Magn Reson Spectrosc*. 2017;101:71-95. doi:10.1016/j.pnmrs.2017.04.002

42. Glockner JF, Hu HH, Stanley DW, Angelos L, King K. Parallel MR imaging: a user's guide. *Radiographics*. 2005;25(5):1279-1297. doi:10.1148/rg.255045202

43. Pruessmann KP, Weiger M, Scheidegger MB, Boesiger P. SENSE: sensitivity encoding for fast MRI. *Magn Reson Med*. 1999;42(5):952-962.

44. Pruessmann KP, Weiger M, Börnert P, Boesiger P. Advances in sensitivity encoding with arbitrary k-space trajectories. *Magn Reson Med*. 2001;46(4):638-651. doi:10.1002/mrm.1241

45. Griswold MA, Jakob PM, Heidemann RM, et al. Generalized autocalibrating partially parallel acquisitions (GRAPPA). *Magn Reson Med*. 2002;47(6):1202-1210. doi:10.1002/mrm.10171

46. Sodickson DK, Manning WJ. Simultaneous acquisition of spatial harmonics (SMASH): fast imaging with radiofrequency coil arrays. *Magn Reson Med*. 1997;38(4):591-603. doi:10.1002/mrm.1910380414

47. Jakob PM, Griswold MA, Edelman RR, Sodickson DK. AUTO-SMASH: a self-calibrating technique for SMASH imaging. SiMultaneous Acquisition of Spatial Harmonics. *MAGMA*. 1998;7(1):42-54. doi:10.1007/BF02592256

48. Heidemann RM, Griswold MA, Haase A, Jakob PM. VD-AUTO-SMASH imaging. *Magnetic Resonance in Medicine*. 2001;45(6):1066-1074. doi:10.1002/mrm.1141

49. Wright KL, Hamilton JI, Griswold MA, Gulani V, Seiberlich N. Non-Cartesian Parallel Imaging Reconstruction. *J Magn Reson Imaging*. 2014;40(5):1022-1040. doi:10.1002/jmri.24521

50. Pfeiffer MP, Biederman RWW. Cardiac MRI: A General Overview with Emphasis on Current Use and Indications. *Medical Clinics*. 2015;99(4):849-861. doi:10.1016/j.mcna.2015.02.011

51. Schwab F, Schwarz F, Dietrich O, et al. Free Breathing Real-Time Cardiac Cine Imaging With Improved Spatial Resolution at 3 T. *Investigative Radiology*. 2013;48(3):158-166. doi:10.1097/RLI.0b013e31827f1b68

52. Ma Y, Hou Y, Ma Q, Wang X, Sui S, Wang B. Compressed SENSE single-breath-hold and free-breathing cine imaging for accelerated clinical evaluation of the left ventricle. *Clin Radiol*. 2019;74(4):325.e9-325.e17. doi:10.1016/j.crad.2018.12.012

53. Sudarski S, Henzler T, Haubenreisser H, et al. Free-breathing Sparse Sampling Cine MR Imaging with Iterative Reconstruction for the Assessment of Left Ventricular Function and Mass at 3.0 T. *Radiology*. 2017;282(1):74-83. doi:10.1148/radiol.2016151002

54. Wang Y, Ying L. Compressed sensing dynamic cardiac cine MRI using learned spatiotemporal dictionary. *IEEE Trans Biomed Eng*. 2014;61(4):1109-1120. doi:10.1109/TBME.2013.2294939

55. Usman M, Ruijsink B, Nazir MS, Cruz G, Prieto C. Free breathing whole-heart 3D CINE MRI with self-gated Cartesian trajectory. *Magnetic Resonance Imaging*. 2017;38:129-137. doi:10.1016/j.mri.2016.12.021

56. Ahmed AH, Zhou R, Yang Y, Nagpal P, Salerno M, Jacob M. Free-breathing and ungated cardiac cine using navigator-less spiral SToRM. *IEEE Trans Med Imaging*. 2020;39(12):3933-3943. doi:10.1109/TMI.2020.3008329

57. Franson D, Dupuis A, Gulani V, Griswold M, Seiberlich N. A System for Real-Time, Online Mixed-Reality Visualization of Cardiac Magnetic Resonance Images. *Journal of Imaging*. 2021;7(12):274. doi:10.3390/jimaging7120274

58. Saybasili H, Herzka DA, Seiberlich N, Griswold MA. Real-time imaging with radial GRAPPA: Implementation on a heterogeneous architecture for low-latency reconstructions. *Magnetic Resonance Imaging*. 2014;32(6):747-758. doi:10.1016/j.mri.2014.02.022

59. Seiberlich N, Wright KL, Ehses P, Griswold M. Through-time 3D radial GRAPPA for whole heart cardiac imaging. *J Cardiovasc Magn Reson*. 2012;14(Suppl 1):P279. doi:10.1186/1532-429X-14-S1-P279

60. Griswold M, Blaimer M, Heidemann R, et al. Rapid evaluation of cardiac function using undersampled radial trueFISP with GRAPPA. *undefined*. Published online 2004. Accessed August 8, 2021. https://www.semanticscholar.org/paper/Rapid-evaluation-of-cardiac-function-using-radial-Griswold-Blaimer/10e33c25619422fd309797e52f03b125296f3535

61. Seiberlich N, Ehses P, Duerk J, Gilkeson R, Griswold M. Improved radial GRAPPA calibration for real-time free-breathing cardiac imaging. *Magnetic Resonance in Medicine*. 2011;65(2):492-505. doi:10.1002/mrm.22618

62. Hamilton JI, Zuchold C, Seiberlich N. Reducing scan time for calibration of through-time radial GRAPPA using PCA coil compression. *J Cardiovasc Magn Reson*. 2015;17(Suppl 1):Q41. doi:10.1186/1532-429X-17-S1-Q41

63. Zhang T, Pauly JM, Vasanawala SS, Lustig M. Coil Compression for Accelerated Imaging with Cartesian Sampling. *Magn Reson Med*. 2013;69(2):571-582. doi:10.1002/mrm.24267

64. Buehrer M, Pruessmann KP, Boesiger P, Kozerke S. Array compression for MRI with large coil arrays. *Magnetic Resonance in Medicine*. 2007;57(6):1131-1139. doi:10.1002/mrm.21237

65. Chang Y, Wang H. Kernel Principal Component Analysis of Coil Compression in Parallel Imaging. Computational and Mathematical Methods in Medicine. doi:10.1155/2018/4254189

66. Huang F, Vijayakumar S, Akao J. Software Compression for Partially Parallel Imaging with Multi-channels. In: *2005 IEEE Engineering in Medicine and Biology 27th Annual Conference*. ; 2005:1348-1351. doi:10.1109/IEMBS.2005.1616677

67. Fessler J. Image reconstruction toolbox. Published online 2012. http://www. eecs. umich. edu/fessler/code

68. Walsh DO, Gmitro AF, Marcellin MW. Adaptive reconstruction of phased array MR imagery. *Magnetic Resonance in Medicine*. 2000;43(5):682-690. doi:10.1002/(SICI)1522-2594(200005)43:5<682::AID-MRM10>3.0.CO;2-G

69. Zhang T, Pauly JM, Vasanawala SS, Lustig M. Coil compression for accelerated imaging with Cartesian sampling. *Magnetic Resonance in Medicine*. 2013;69(2):571-582. doi:10.1002/mrm.24267

70. Huang F, Vijayakumar S, Li Y, Hertel S, Duensing GR. A software channel compression technique for faster reconstruction with many channels. *Magnetic Resonance Imaging*. 2008;26(1):133-141. doi:10.1016/j.mri.2007.04.010

71. Zhou Z, Han F, Ghodrati V, et al. Parallel imaging and convolutional neural network combined fast MR image reconstruction: Applications in low-latency accelerated real-time imaging. *Medical Physics*. 2019;46(8):3399-3413. doi:10.1002/mp.13628

72. Sandino CM, Lai P, Vasanawala SS, Cheng JY. Accelerating cardiac cine MRI using a deep learning-based ESPIRiT reconstruction. *Magnetic Resonance in Medicine*. 2021;85(1):152-167. doi:10.1002/mrm.28420

73. Vermersch M, Longère B, Coisne A, et al. Compressed sensing real-time cine imaging for assessment of ventricular function, volumes and mass in clinical practice. *Eur Radiol*. 2020;30(1):609-619. doi:10.1007/s00330-019-06341-2

74. Bustin A, Fuin N, Botnar RM, Prieto C. From Compressed-Sensing to Artificial Intelligence-Based Cardiac MRI Reconstruction. *Frontiers in Cardiovascular Medicine*. 2020;7:17. doi:10.3389/fcvm.2020.00017

75. Hamilton JI, Jiang Y, Chen Y, et al. MR fingerprinting for rapid quantification of myocardial T1, T2, and proton spin density. *Magnetic Resonance in Medicine*. 2017;77(4):1446-1458. doi:10.1002/mrm.26216

76. Hamilton JI, Wright KL, Jiang Y, et al. Pulse Sequence Optimization for Improved MRF Scan Efficiency. :1.

77. Hamilton JI, Griswold MA, Seiberlich N. MR Fingerprinting with chemical exchange (MRF-X) to quantify subvoxel T1 and extracellular volume fraction. *Journal of Cardiovascular Magnetic Resonance*. 2015;17(1):W35. doi:10.1186/1532-429X-17-S1-W35

78. Cohen O, Huang S, McMahon MT, Rosen MS, Farrar CT. Rapid and quantitative chemical exchange saturation transfer (CEST) imaging with magnetic resonance fingerprinting (MRF). *Magnetic Resonance in Medicine*. 2018;80(6):2449-2463. doi:10.1002/mrm.27221

79. Hong T, Han D, Kim MO, Kim DH. RF slice profile effects in magnetic resonance fingerprinting. *Magnetic Resonance Imaging*. 2017;41:73-79. doi:10.1016/j.mri.2017.04.001

80. Hamilton JI, Jiang Y, Ma D, et al. Investigating and reducing the effects of confounding factors for robust T1 and T2 mapping with cardiac MR fingerprinting. *Magnetic Resonance Imaging*. 2018;53:40-51. doi:10.1016/j.mri.2018.06.018

81. Ma D, Coppo S, Chen Y, et al. Slice profile and B1 corrections in 2D magnetic resonance fingerprinting. *Magn Reson Med*. 2017;78(5):1781-1789. doi:10.1002/mrm.26580

82. Jiang Y, Ma D, Keenan KE, Stupic KF, Gulani V, Griswold MA. Repeatability of magnetic resonance fingerprinting T1 and T2 estimates assessed using the ISMRM/NIST MRI system phantom. *Magnetic Resonance in Medicine*. 2017;78(4):1452-1457. doi:10.1002/mrm.26509

83. Buonincontri G, Biagi L, Retico A, et al. Multi-site repeatability and reproducibility of MR fingerprinting of the healthy brain at 1.5 and 3.0 T. *Neuroimage*. 2019;195:362-372. doi:10.1016/j.neuroimage.2019.03.047

84. Körzdörfer G, Kirsch R, Liu K, et al. Reproducibility and Repeatability of MR Fingerprinting Relaxometry in the Human Brain. *Radiology*. 2019;292(2):429-437. doi:10.1148/radiol.2019182360

85. Lo WC, Jiang Y, Bittencourt LK, et al. Multicenter repeatability and reproducibility of MR Fingerprinting. In: *Joint Annual Meeting ISMRM-ESMRMB*. ; 2018.

86. Panda A, Chen Y, Ropella-Panagis K, et al. Repeatability and reproducibility of 3D MR fingerprinting relaxometry measurements in normal breast tissue. *J Magn Reson Imaging*. 2019;50(4):1133-1143. doi:10.1002/jmri.26717

87. Hansen MS, Sørensen TS. Gadgetron: an open source framework for medical image reconstruction. *Magn Reson Med*. 2013;69(6):1768-1776. doi:10.1002/mrm.24389

88. Franson D, Ahad J, Hamilton JI, et al. (ISMRM 2017) Real-time 3D cardiac MRI using through-time radial GRAPPA and GPU-enabled reconstruction pipelines in the Gadgetron framework. In: ; 2017. Accessed February 25, 2018. http://dev.ismrm.org/2017/0448.html

89. Simpson R, Keegan J, Gatehouse P, Hansen M, Firmin D. Spiral tissue phase velocity mapping in a breath-hold with non-cartesian SENSE. *Magnetic Resonance in Medicine*. 2014;72(3):659-668. doi:10.1002/mrm.24971

90. Xue H, Hansen MS, Nielles-Vallespin S, Arai AE, Kellman P. Nonlinear myocardial perfusion imaging with motion corrected reconstruction: validation via quantitative flow mapping. *Journal of Cardiovascular Magnetic Resonance*. 2016;18(1):O8. doi:10.1186/1532-429X-18-S1-O8

91. Xue H, Brown LAE, Nielles-Vallespin S, Plein S, Kellman P. Automatic in-line quantitative myocardial perfusion mapping: Processing algorithm and implementation. *Magnetic Resonance in Medicine*. 2020;83(2):712-730. doi:10.1002/mrm.27954

92. Lo WC, Jiang Y, Franson D, Griswold M, Gulani V, Seiberlich N. MR Fingerprinting using a Gadgetron-based reconstruction. In: *Joint Annual Meeting ISMRM-ESMRMB*. ; 2018.

93. Cheng HLM, Stikov N, Ghugre NR, Wright GA. Practical medical applications of quantitative MR relaxometry. *Journal of Magnetic Resonance Imaging*. 2012;36(4):805-824. doi:10.1002/jmri.23718

94. Friedrich MG, Abdel-Aty H, Taylor A, Schulz-Menger J, Messroghli D, Dietz R. The salvaged area at risk in reperfused acute myocardial infarction as visualized by cardiovascular magnetic resonance. *J Am Coll Cardiol*. 2008;51(16):1581-1587. doi:10.1016/j.jacc.2008.01.019

95. Abdel-Aty H, Cocker M, Meek C, Tyberg JV, Friedrich MG. Edema as a Very Early Marker for Acute Myocardial Ischemia: A Cardiovascular Magnetic Resonance Study. *Journal of the American College of Cardiology*. 2009;53(14):1194-1201. doi:10.1016/j.jacc.2008.10.065

96. Lotan CS, Miller SK, Bouchard A, et al. Detection of intramyocardial hemorrhage using high-field proton (1H) nuclear magnetic resonance imaging. *Cathet Cardiovasc Diagn*. 1990;20(3):205-211.

97. Foltz Warren D., Huang Hong, Fort Stephen, Wright Graham A. Vasodilator Response Assessment in Porcine Myocardium With Magnetic Resonance Relaxometry. *Circulation*. 2002;106(21):2714-2719. doi:10.1161/01.CIR.0000039475.66067.DC

98. Inati SJ, Naegele JD, Zwart NR, et al. ISMRM Raw data format: A proposed standard for MRI raw datasets. *Magnetic Resonance in Medicine*. 2017;77(1):411-421. doi:10.1002/mrm.26089

99. McGivney DF, Pierre E, Ma D, et al. SVD Compression for Magnetic Resonance Fingerprinting in the Time Domain. *IEEE Transactions on Medical Imaging*. 2014;33(12):2311-2322. doi:10.1109/TMI.2014.2337321

100. Inati S, Hansen MS, Kellman P. A Solution to the Phase Problem in Adaptive Coil Combination. In: *Proceedings of the 21st Meeting of the International Society of Magnetic Resonance in Medicine*. ; 2013:2672.

101. Standardized Myocardial Segmentation and Nomenclature for Tomographic Imaging of the Heart. :4.

102. Altman DG, Bland JM. Measurement in Medicine: The Analysis of Method Comparison Studies. *Journal of the Royal Statistical Society: Series D (The Statistician)*. 1983;32(3):307-317. doi:10.2307/2987937

103. Giavarina D. Understanding Bland Altman analysis. *Biochem Med (Zagreb)*. 2015;25(2):141-151. doi:10.11613/BM.2015.015

104. Merkel D. Docker: Lightweight Linux Containers for Consistent Development and Deployment. *Linux J*. 2014;2014(239). Accessed April 25, 2019. http://dl.acm.org/citation.cfm?id=2600239.2600241

105. Li Z, Wang D, Robison RK, et al. Sliding-slab three-dimensional TSE imaging with a spiral-In/Out readout. *Magn Reson Med*. 2016;75(2):729-738. doi:10.1002/mrm.25660

106. Li Z, Karis JP, Pipe JG. A 2D spiral turbo-spin-echo technique. *Magn Reson Med*. 2018;80(5):1989-1996. doi:10.1002/mrm.27171

107. Block W, Pauly J, Nishimura D. RARE spiral T2-weighted imaging. *Magn Reson Med*. 1997;37(4):582-590.

108. Aandal G, Nadig V, Yeh V, et al. Evaluation of left ventricular ejection fraction using through-time radial GRAPPA. *Journal of Cardiovascular Magnetic Resonance*. 2014;16(1):79. doi:10.1186/s12968-014-0079-8

109. Kido T, Kido T, Nakamura M, et al. Compressed sensing real-time cine cardiovascular magnetic resonance: accurate assessment of left ventricular function in a single-breath-hold. *Journal of Cardiovascular Magnetic Resonance*. 2016;18(1):50. doi:10.1186/s12968-016-0271-0

110. Park YS, Lee CH, Kim IS, et al. Usefulness of controlled aliasing in parallel imaging results in higher acceleration in gadoxetic acid-enhanced liver magnetic resonance imaging to clarify the hepatic arterial phase. *Invest Radiol*. 2014;49(3):183-188. doi:10.1097/RLI.0000000000000011

111. Mann L, Higgins D, Peters C, et al. Accelerating MR Imaging Liver Steatosis Measurement Using Combined Compressed Sensing and Parallel Imaging: A Quantitative Evaluation. *Radiology*. 2015;278:150320. doi:10.1148/radiol.2015150320

112. Fielden SW, Mugler III JP, Hagspiel KD, Norton PT, Kramer CM, Meyer CH. Noncontrast peripheral MRA with spiral echo train imaging. *Magnetic Resonance in Medicine*. 2015;73(3):1026-1033. doi:10.1002/mrm.25216

113. Li Z, Schär M, Wang D, et al. Arterial spin labeled perfusion imaging using three-dimensional turbo spin echo with a distributed spiral-in/out trajectory. *Magn Reson Med*. 2016;75(1):266-273. doi:10.1002/mrm.25645

114. Munsch F, Taso M, Zhao L, et al. Rotated spiral RARE for high spatial and temporal resolution volumetric arterial spin labeling acquisition. *NeuroImage*. 2020;223:117371. doi:10.1016/j.neuroimage.2020.117371

115. Kasivisvanathan V, Rannikko AS, Borghi M, et al. MRI-Targeted or Standard Biopsy for Prostate-Cancer Diagnosis. *New England Journal of Medicine*. Published online March 18, 2018. doi:10.1056/NEJMoa1801993

116. Cornud F, Bomers J, Futterer JJ, Ghai S, Reijnen JS, Tempany C. MR imaging-guided prostate interventional imaging: Ready for a clinical use? *Diagnostic and Interventional Imaging*. 2018;99(11):743-753. doi:10.1016/j.diii.2018.08.002

117. Walser EM, Sze TF, Ross JR, Karamanian AA, Woodrum DA. MRI-Guided Prostate Interventions. *American Journal of Roentgenology*. 2016;207(4):755-763. doi:10.2214/AJR.16.16663

118. Overduin CG, Heidkamp J, Rothgang E, Barentsz JO, de Lange F, Fütterer JJ. Fast 3-T MR-guided transrectal prostate biopsy using an in-room tablet device for needle guide alignment: a feasibility study. *Eur Radiol*. 2018;28(11):4824-4831. doi:10.1007/s00330-018-5497-9

119. Schimmöller L, Blondin D, Arsov C, et al. MRI-Guided In-Bore Biopsy: Differences Between Prostate Cancer Detection and Localization in Primary and Secondary Biopsy Settings. *American Journal of Roentgenology*. 2016;206(1):92-99. doi:10.2214/AJR.15.14579

120. Kwan RK, Evans AC, Pike GB. MRI simulation-based evaluation of image-processing and classification methods. *IEEE Trans Med Imaging*. 1999;18(11):1085-1097. doi:10.1109/42.816072

121. Petersson JS, Christoffersson JO, Golman K. MRI simulation using the k-space formalism. *Magnetic Resonance Imaging*. 1993;11(4):557-568. doi:10.1016/0730-725X(93)90475-S

122. Jaynes ET. Matrix Treatment of Nuclear Induction. *Phys Rev*. 1955;98(4):1099-1105. doi:10.1103/PhysRev.98.1099

123. Hargreaves BA. Rapid gradient-echo imaging. *J Magn Reson Imaging*. 2012;36(6):1300-1313. doi:10.1002/jmri.23742

124. Panda A, Obmann VC, Lo WC, et al. MR Fingerprinting and ADC Mapping for Characterization of Lesions in the Transition Zone of the Prostate Gland. *Radiology*. 2019;292(3):685-694. doi:10.1148/radiol.2019181705

125. Panda A, O'Connor G, Lo WC, et al. Targeted Biopsy Validation of Peripheral Zone Prostate Cancer Characterization with MR Fingerprinting and Diffusion Mapping. *Invest Radiol*. 2019;54(8):485-493. doi:10.1097/RLI.0000000000000569

126. Kakkar LS, Usman M, Arridge S, Kirkham A, Atkinson D. Characterization of B0-field fluctuations in prostate MRI. *Phys Med Biol*. 2020;65(21):21NT01. doi:10.1088/1361-6560/abbc7f

127. Wu LM, Yao QY, Zhu J, et al. T2* mapping combined with conventional T2-weighted image for prostate cancer detection at 3.0T MRI: a multi-observer study. *Acta Radiol*. 2017;58(1):114-120. doi:10.1177/0284185116633916

128. Wu LM, Chen XX, Xuan HQ, et al. Feasibility and Preliminary Experience of Quantitative T2* Mapping at 3.0 T for Detection and Assessment of Aggressiveness of Prostate Cancer. *Academic Radiology*. 2014;21(8):1020-1026. doi:10.1016/j.acra.2014.04.007

129. Wu LM, Zhao ZZ, Chen XX, et al. Comparison of T2* mapping with diffusion-weighted imaging in the characterization of low-grade vs intermediate-grade and high-grade prostate cancer. *Br J Radiol*. 89(1063):20151076. doi:10.1259/bjr.20151076

130. Lo WC, Panda A, Jiang Y, Ahad J, Gulani V, Seiberlich N. MR fingerprinting of the prostate. *Magn Reson Mater Phy*. 2022;35(4):557-571. doi:10.1007/s10334-022-01012-8

131. Panda A, Chen Y, Ropella-Panagis K, et al. Repeatability and reproducibility of 3D MR fingerprinting relaxometry measurements in normal breast tissue. *J Magn Reson Imaging*. 2019;50(4):1133-1143. doi:10.1002/jmri.26717

132. Hepp T, Kalmbach L, Kolb M, et al. T2 mapping for the characterization of prostate lesions. *World J Urol*. 2022;40(6):1455-1461. doi:10.1007/s00345-022-03991-8

133. Hoang Dinh A, Souchon R, Melodelima C, et al. Characterization of prostate cancer using T2 mapping at 3T: A multi-scanner study. *Diagnostic and Interventional Imaging*. 2015;96(4):365-372. doi:10.1016/j.diii.2014.11.016

134. Lee CH. Quantitative T2-mapping using MRI for detection of prostate malignancy: a systematic review of the literature. *Acta Radiol*. 2019;60(9):1181-1189. doi:10.1177/0284185118820058

135. Mai J, Abubrig M, Lehmann T, et al. T2 Mapping in Prostate Cancer. *Invest Radiol*. 2019;54(3):146-152. doi:10.1097/RLI.0000000000000520

136. Fielden SW, Meyer CH. A simple acquisition strategy to avoid off-resonance blurring in spiral imaging with redundant spiral-in/out k-space trajectories. *Magn Reson Med*. 2015;73(2):704-710. doi:10.1002/mrm.25172

137. Haacke EM, Liang ZP, Boada F. Image reconstruction using projection onto convex sets, model constraints, and linear prediction theory for the removal of phase, motion, and Gibbs artifacts in magnetic resonance and ultrasound imaging. *SPIE J*. 1990;29(5):555-566. doi:10.1117/12.55624

138. A 2D spiral turbo-spin-echo technique. - PubMed - NCBI. Published March 18, 2019. Accessed March 18, 2019. https://www.ncbi.nlm.nih.gov/pubmed/29524248

139. Atkinson D, Hill DL, Stoyle PN, Summers PE, Keevil SF. Automatic correction of motion artifacts in magnetic resonance images using an entropy focus criterion. *IEEE Trans Med Imaging*. 1997;16(6):903-910. doi:10.1109/42.650886

140. Philips B, Uden M, Rietsch S, Orzada S, Scheenen T. A multi-transmit external body array combined with a 1 H and 31 P endorectal coil to enable a multi-parametric and multi-metabolic MRI examination of the prostate at 7T. *Medical Physics*. 2019;46. doi:10.1002/mp.13696

141. Masoom SN, Sundaram KM, Ghanouni P, et al. Real-Time MRI-Guided Prostate Interventions. *Cancers (Basel)*. 2022;14(8):1860. doi:10.3390/cancers14081860

142. Das CJ, Razik A, Sharma S, Verma S. Prostate biopsy: when and how to perform. *Clinical Radiology*. 2019;74(11):853-864. doi:10.1016/j.crad.2019.03.016

143. Hennig J, Weigel M, Scheffler K. Multiecho sequences with variable refocusing flip angles: Optimization of signal behavior using smooth transitions between pseudo steady states (TRAPS). *Magnetic Resonance in Medicine*. 2003;49(3):527-535. doi:10.1002/mrm.10391

144. Busse RF, Hariharan H, Vu A, Brittain JH. Fast spin echo sequences with very long echo trains: Design of variable refocusing flip angle schedules and generation of clinical T2 contrast. *Magnetic Resonance in Medicine*. 2006;55(5):1030-1037. doi:10.1002/mrm.20863

145. Single shot spiral TSE with annulated segmentation - Hennig - 2022 - Magnetic Resonance in Medicine - Wiley Online Library. Accessed December 29, 2022. https://onlinelibrary.wiley.com/doi/full/10.1002/mrm.29224